Nonlinear Structural Analysis

Contents

Nonlinear Structural Analysis

Basics

Area of Application

The analysis option *Nonlinear analysis* enables the determination of the internal forces and deformations of beam and shell structures made of reinforced concrete and steel as well as stress states of solid elements considering geometric and physical nonlinearities. A distinction can be made between calculations with material characteristics for the ultimate limit state or the serviceability limit state. Due to the considerable numerical complexity, it only makes sense to use this program module for special problems.

Specifically, the following nonlinear effects can be taken into consideration:

- Equilibrium of the deformed system according to the second- or third order theory, if this has been activated for the corresponding load case.
- Beams and area elements made of reinforced concrete according to DIN 1045, DIN 1045-1, OENORM B4700, SIA 262 and EN 1992-1-1.
- Beams and area elements made of steel with bilinear stress-strain curve under consideration of the Huber-von Mises yield criterion and complete interaction with all internal forces.
- Beams and area elements with bilinear stress-strain curve respectively yield criterion according to Raghava or Rankine and individually definable compressive and tensile strength.
- Solids with isotropic damage according to De Vree or Mazars as well as yield criteria according to Huber-Mises, Raghava, Rankine, Mohr-Coulomb, Drucker-Prager or Lubliner with linear hardening.
- Solids with combined plasticity and damage.
- Compression-flexible beams.
- Beam and area element bedding with bilinear bedding curve perpendicular to and alongside the beam.
- Solid elements with bilinear bedding curve in the element coordinate system.
- Pressed steel layers in bond with concrete in beams can be considered with a bilinear stress-strain curve.
- Tendon groups in bond with concrete can be taken into account with a bilinear stress-strain curve.
- Prestressing without bond (only load) can also be simulated.
- Beams and area elements made of steel and reinforced concrete in case of fire according to EN 1992-1-2 and EN 1993-1-2 or beams made of timber in case of fire according to EN 1995-1-2
  (see chapter '*Structural analysis for fire scenarios*').

Analysis Method

The analysis model used is based on the finite element method. To carry out a nonlinear system analysis, the standard beam elements are replaced internally with shear-flexible nonlinear beams with an increased displacement function. For the treatment of area and volume structures nonlinear layer elements and solid elements are used. In contrast to the linear calculation and in order to account for the nonlinear or even discontinuous properties of the structure, a finer subdivision is generally necessary. The program assumes that the actions defined in the load cases are weighted with the appropriate partial safety factors.

Requirements

- The beams are assumed to be straight.
- The area elements are flat.
- Area and beam sections are constant for each element.
- The dimensions of the section are small compared with the other system dimensions.
- Shear deformations of beams are accounted for with a shear distortion that is constant across the section, meaning the section remains plane after the deformation but is no longer perpendicular to the beam axis.
- The mathematical curvature is linearized (second-order theory).
- The load is slowly increased to its final value and does not undergo any deviation in direction as a result of the system deformation.

Equilibrium iteration

To solve the nonlinear system of equations, both the incremental Newton-Raphson method and the arc length method can be used. In both methods, the tangential stiffness matrix is computed in each iteration depending on the current internal force and deformation state. Alternatively, a constant stiffness matrix (*linear stiffness method*) can be used. Here, the stiffness matrix is computed only once at the beginning of the numerical simulation and in the following assumed to be constant.

The following calculation methods are available:

- *Newton method*:
  The iteration is load-controlled until the residual (length of the error vector) falls below a required error limit. If the limit is not reached within the maximum allowable iteration steps per load level, the iteration is aborted and the load factor (≤ 1.0) is determined by interval nesting.

- *Newton time steps method (NTS)*:
  The solution method corresponds to the Newton method, except that for each time step the load present at that time may be different according to the defined load-time function. Based on the solution of the last time step, a solution for the next time step is determined. If it is not possible to fall below the error limit within the maximum iteration steps per load level, the solution for an intermediate point in time is determined by interval nesting.

- *Arc length method (ARC)*:
  In this method, in each iteration cycle, starting from the last converged state, the solution of an extended nonlinear system of equations along a circular arc with a given radius (arc length) is sought. As a result of the additional constraint that has to be considered (equation of a generalized sphere), there is another unknown besides the deformation vector - the load factor. Due to the combined load-displacement-controlled method, the behavior of structures in the supercritical range (including *snap through* and *snap back*) can be analyzed. If, within the maximum allowable iteration steps per arc length, the error is larger than the given tolerance, a solution for a smaller arc length is determined. The end of the calculation is controlled either by the number of increments (arc lengths, iteration cycles), the 1st bifurcation point, or a load factor to be reached. It is possible to increase the load within a load case only for selected loads. For this purpose, an arbitrary load-time history must be assigned to these loads. All other loads are constant. The shape of the load-time function is irrelevant.

The following figures illustrate the different iteration progressions using the example of a beam with one degree of freedom.
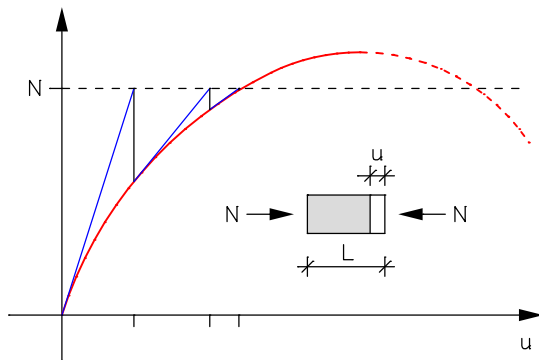
Newton method with tangential stiffness
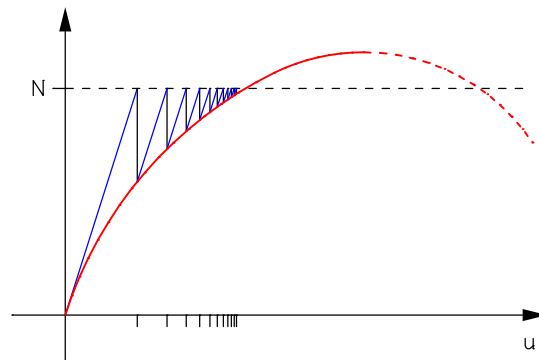
Newton method with constant stiffness
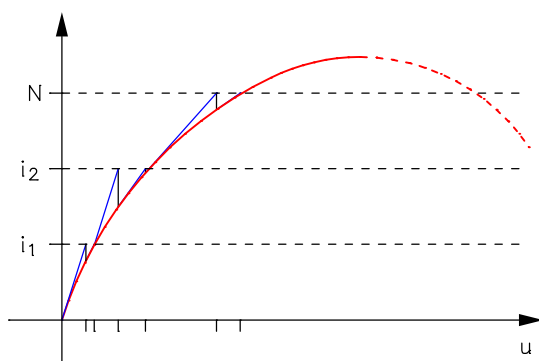
Newton method with time steps and tangential stiffness
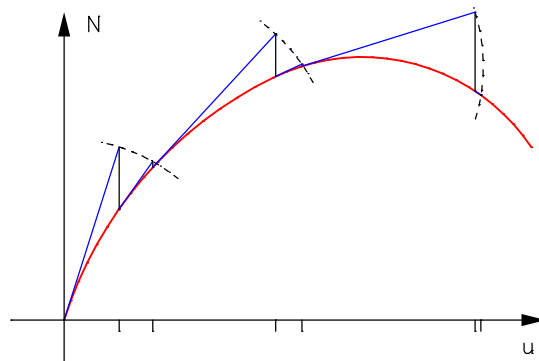
Arc length method with tangential stiffness

When performing a check on the entire system according to OENORM B4700 (Section 3.4.3.3), you need to keep in mind that the decisive action combination may only amount to 80% of the reachable system limit load. To account for this, you can, for example, introduce an additional load factor of 1.25.

For reinforced concrete components the existing reinforcement forms the basis of the calculation. If desired, an automatic reinforcement increase can be carried out for the load bearing capacity check to achieve the required load level.

Finite Beam Elements

A shear-flexible beam element with 4 nodes is used. Both inner nodes are hidden to the user. Each node has the degrees of freedom u_x, u_y, u_z, φ_x, φ_y and φ_z.
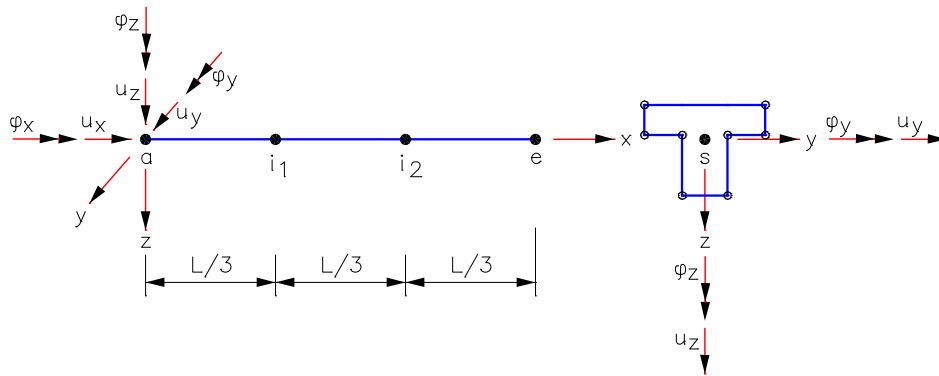
Beam element with node degrees of freedom

Because independent deformation functions are used for the displacement and rotation of shear-flexible elements, all deformations of the given beam element are approximated by third-order polynomials.

This allows an equivalent representation of the strains and curvatures, which is especially advantageous for determining the physical nonlinearities. All internal forces are described by second-order polynomials (quadratic parabolas).

In connection to shell elements equivalent shear fixed beam elements are used to provide compatibility.

For linear calculation and constant element load in the longitudinal or lateral direction the results are precise. Other loads, such as point loads in the element or trapezoidal loads in the element, can only be approximated. The quality of the results depends on the chosen structure discretization.

Kinematics

$$u_x(x, y, z) = u_x(x) - y \cdot \varphi_z(x) + z \cdot \varphi_y(x)$$

$$u_y(x, y, z) = u_y(x) - z \cdot \varphi_x(x)$$

$$u_z(x, y, z) = u_z(x) - y \cdot \varphi_x(x)$$

Distortion-displacement relationships

$$\varepsilon_x = \frac{\partial u_x}{\partial x} + \frac{1}{2}\left[\left(\frac{\partial u_y}{\partial x}\right)^2 + \left(\frac{\partial u_z}{\partial x}\right)^2\right]$$

$$\gamma_{xy} = \frac{\partial u_x}{\partial y} + \frac{\partial u_y}{\partial x}$$

$$\gamma_{xz} = \frac{\partial u_z}{\partial x} + \frac{\partial u_x}{\partial z}$$

$$\vartheta' = \frac{\partial \varphi_x}{\partial x}$$

$$\varepsilon_y = \varepsilon_z = \gamma_{yz} = 0$$

Virtual internal work

$$\Psi(a) = \int_V \delta\varepsilon \cdot \sigma \, dV + \int_V \delta\gamma \cdot \tau \, dV + \int_L \delta\vartheta' \cdot M_x \, dx$$

       Normal force   *Shear*   *Torsion*
       Bending

a Nodal degrees of freedom

Tangential stiffness matrix

$$\frac{d\Psi}{da} = K_{\mathrm{T}} = \int_V \left(dB^{\mathrm{T}} \cdot \sigma + B^{\mathrm{T}} \cdot \frac{d\sigma}{d\varepsilon} \right) dV + K_{\mathrm{shear}} + K_{\mathrm{torsion}}$$

$$= K_0 + K_{\mathrm{G}} + K_{\mathrm{L}} + K_{\mathrm{shear}} + K_{\mathrm{torsion}}$$

with $d\varepsilon = B \cdot da$ and $B = B_0 + B_{\mathrm{L}}$

If necessary, terms from the bedding of the elements can be added.

Section Analysis

In general, a nonlinear analysis can only be performed for polygon sections, database sections and steel sections. For all other section types and for the material types *Beton* and *Timber* an elastic material behavior is assumed. In order to determine the nonlinear stiffnesses and internal forces, you need to perform a numeric integration of the stresses and their derivatives across the section area. The procedure differs depending on the material.

Reinforced Concrete Beams

Based on the stress-strain curves shown further below, the resulting internal forces N_x, M_y and M_z at the section can be determined for a known strain state by integrating the normal stresses. For determining the strain and stress states at the section the following assumptions are made:

- The sections remain flat at every point in time during the deformation, even when the section is cracked as a result of exceeding the concrete tensile strength.
- The concrete and reinforcement are perfectly bonded.
- The tensile strength of the concrete is usually ignored, but it can be taken into account if desired.
- The tensile section of the stress-strain curves can be described using one of the two following curves:
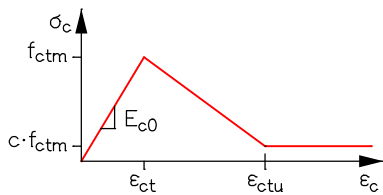
With softening   *Bilinear*
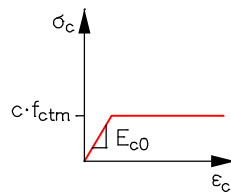
ε_{ct} Strain when reaching the concrete tensile strength

ε_{ctu} Strain after exceeding the specific fracture energy G_f

$$G_f = G_{f0} \cdot \left(\frac{f_{cm}}{f_{cmo}} \right)^{0.7} \qquad G_{fo} \approx 3.0 \cdot 10^{-5} \, \frac{\mathrm{MNm}}{\mathrm{m}^2} \qquad f_{cmo} = 10 \, \frac{\mathrm{MN}}{\mathrm{m}^2}$$

f_{cm} Average concrete compressive strength

- The tension stiffening effect of the concrete is accounted for by the residual tensile stress $\sigma = c \cdot f_{ctm}$ or $c \cdot \beta_{bz}$. The constant c can be set by the user (default: 0.1).
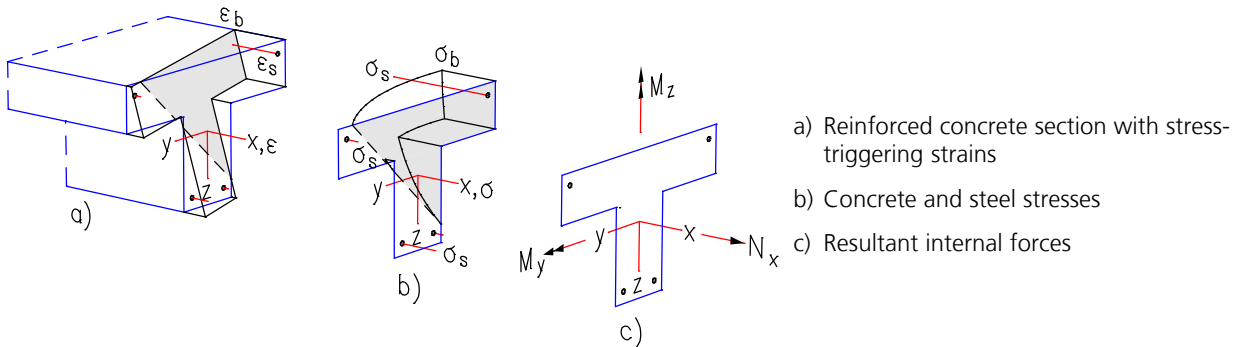
a) Reinforced concrete section with stress-triggering strains

b) Concrete and steel stresses

c) Resultant internal forces

Depending on the chosen material type, the following stress-strain curves are applied. The tensile section of the concrete is only activated as an option.

         © InfoGraph GmbH, February 2024

Stress-Strain-Curves for the Ultimate Limit State Check

The following material partial safety factors are implemented. For Concretes according to EN 1992-1-1 or OENORM B 4700 the user-defined material safety factors for the permanent and temporary design situation or fundamental combination are used.

The stress-strain curves of prestressing steel have a rising branch with E_p and a horizontal upper branch at f_{pd}. Depending on the concrete, the following strengths are assumed for f_{pd}.

- Concrete *DIN 1045:1988* : $f_{pd} = \beta_s$

- Concrete *DIN EN 1992-1-1, DIN 1045-1* : $f_{pd} = 1{,}1 \cdot f_{p0,1k}/\gamma_R$ mit $\gamma_R = 1.3$

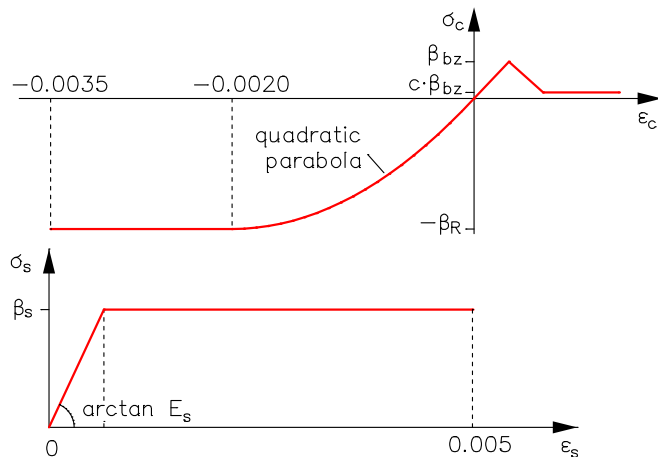- Concrete *EN 1992-1-1, ÖNORM B 4700, SIA 262* : $f_{pd} = f_{p0,1k}/\gamma_s$ mit $\gamma_s = 1.15$

Concrete acc. to DIN 1045:1988, Figure 11
β_R acc. to Table 12
$\sigma_c = -\beta_R \cdot (\varepsilon_b - 1/4 \cdot \varepsilon_b{}^2)$ for $0 \geq \varepsilon_b \geq -2$ ‰

Reinforcing steel acc. to DIN 1045:1988, Figure 12
$E_s = 210000$ MN/m² acc. to Figure 12
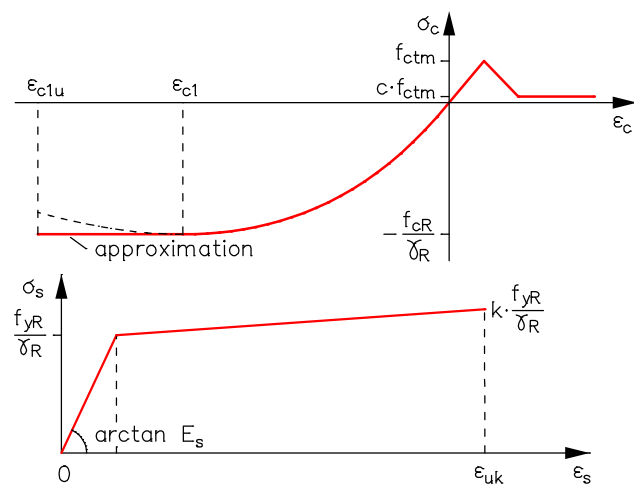
Stress-strain curves according to DIN 1045

Concrete acc. to DIN 1045-1, 9.1.5
σ_c acc. to Equation (62) or Figure 22 for $0 \geq \varepsilon_c \geq \varepsilon_{c1}$
with f_{cR}/γ_R instead of f_c ; $\gamma_R = 1.3$
E_{c0m} or E_{lc0m} instead of E_{c0}
f_{cR} acc. to Eq. (23) or Eq. (24)

Normal concrete: $\alpha = 0.85$

Lightweight concrete: f_{lck} instead of f_{ck} and $\alpha = 0.75$

Reinforcing steel acc. to DIN 1045-1, 9.2.3 Figure 26
$f_{yR} = 1{,}1 \cdot f_{yk}$; $\gamma_R = 1.3$ acc. to 8.5.1 (4)
$k = 1.05$; $\varepsilon_{uk} = 2.5\%$ acc. to Table 11, Column 1 or 2
$E_s = 200000$ MN/m² acc. to 9.2.4 (4)
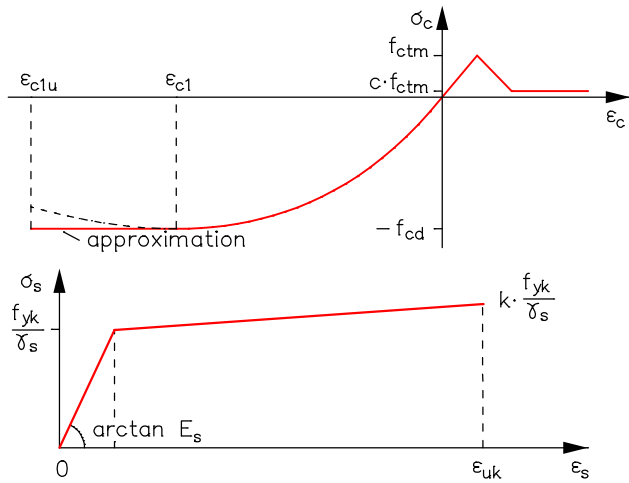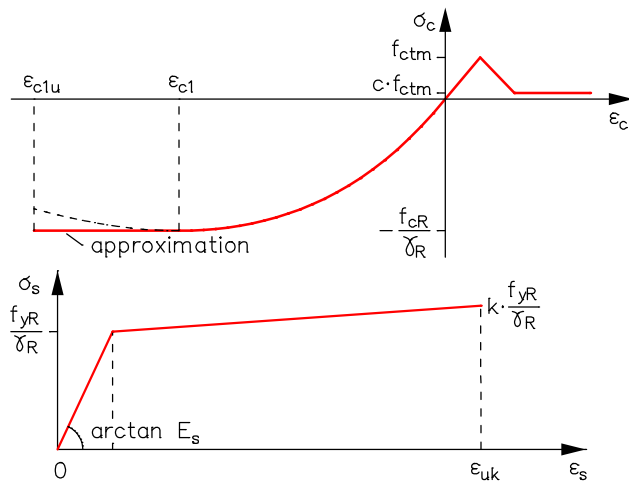
Stress-strain curves according to DIN 1045-1

Concrete acc. to EN 1992-1-1, 3.1.5

σ_c acc. to Equation (3.14) for $0 \geq \varepsilon_c \geq \varepsilon_{c1}$ or ε_{lc1}

with f_{cd} or f_{lcd} instead of f_{cm} and acc. Eq. (5.20)

$E_{cd} = E_{cm}/\gamma_c$ instead of E_{cm}

with $\gamma_{cE} = 1.2$ and E_{cm} as specified

Normal concrete: $\quad f_{cd} = \alpha_{cc} \cdot f_{ck}/\gamma_c$ (Eq. 3.15) with $\alpha_{cc} = 1.0$

Lightweight concrete: $\quad f_{lcd} = \alpha_{lcc} \cdot f_{lck}/\gamma_c$ (Eq. 11.3.15)

with $\alpha_{lcc} = 0.85$

γ_c as specified (Table 2.1N, Row 1, $\gamma_c = 1.5$)

Reinforcing steel acc. to EN 1992-1-1, 3.2.7 Figure 3.8

$k = 1.05$; $\varepsilon_{uk} = 2.5\%$ acc. to Table C.1, Column A

$E_s = 200000$ MN/m² acc. to 3.2.7 (4)
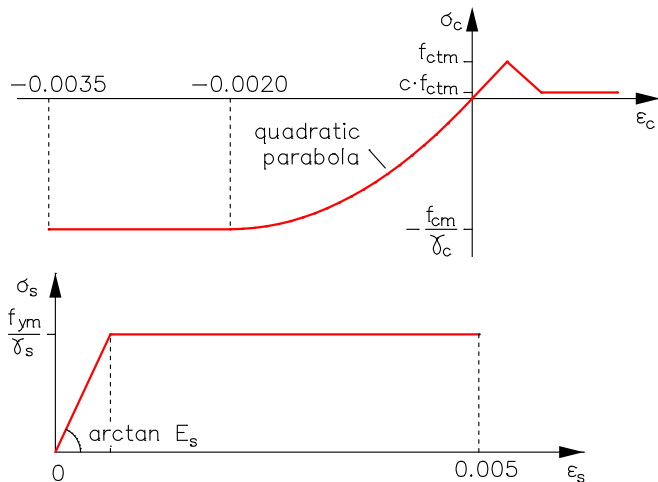
$\gamma_s = 1.15$ acc. to Table 2.1N, Row 1

Stress-strain curves according to EN 1992-1-1

Concrete acc. to DIN EN 1992-1-1, 3.1.5

σ_c acc. to Equation (3.14) for $0 \geq \varepsilon_c \geq \varepsilon_{c1}$ or ε_{lc1}

with f_{cR}/γ_R instead of f_{cm} and E_{cm}/γ_R instead of E_{cm}

with $\gamma_R = 1.3$ and E_{cm} as specified

f_{cR} acc. to Eq. (NA.5.12.7)

Normal concrete: $\quad f_{cR} = 0.85 \cdot \alpha_{cc} \cdot f_{ck}$ with $\alpha_{cc} = 0.85$

Lightweight concrete: $\quad f_{cR} = 0.85 \cdot \alpha_{lcc} \cdot f_{lck}$ with $\alpha_{lcc} = 0.75$

Reinforcing steel acc. to DIN EN 1992-1-1, 3.2.7 Figure 3.8

$f_{yR} = 1.1 \cdot f_{yk}$ acc. to Eq. (NA.5.12.2); $\gamma_R = 1.3$

$k = 1.05$; $\varepsilon_{uk} = 2.5\%$ acc. to Eq. (NA.5.12.4)

$E_s = 200000$ MN/m² acc. to 3.2.7 (4)

Stress-strain curves according to DIN EN 1992-1-1

Concrete acc. to OENORM B 4700, 3.4.1.1 Figure 7

with $f_{cm} = f_{ck} + 7.5$ (N/mm²) acc. to Equation (10c) and

$f_{ck} = 0.75 \cdot f_{cwk}$ acc. to 3.4.1.1 (2)

γ_c as specified (Table 1, Row 1, $\gamma_c = 1.5$)

Reinforcing steel acc. to OENORM B 4700, 3.4.1.2 Figure 9

with $f_{ym} = f_{yk} + 10$ (N/mm²) acc. to Equation (10d)

$E_s = 200000$ MN/m² acc. to Figure 9

$\gamma_s = 1.15$ acc. to Table 1, Row 1
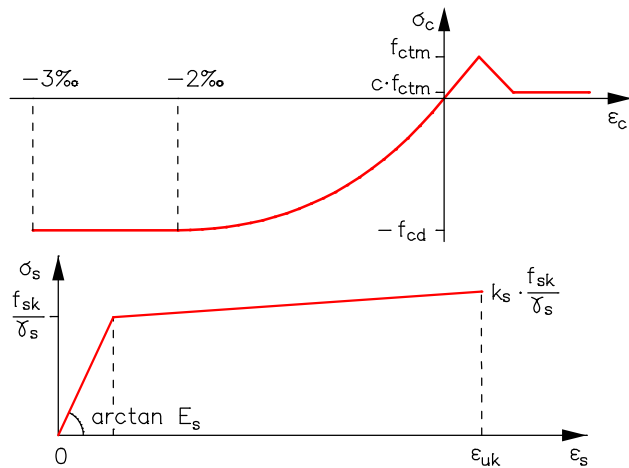
Stress-strain curves according to OENORM B 4700

Concrete acc. to SIA 262, 4.2.1.6 and Figure 12
σ_c acc. to Equation (28) for $0 \geq \varepsilon_c \geq$ -2 ‰ with
f_{cd} acc. to Eq. (2) and Eq. (26); $\gamma_c = 1.5$ acc. to 2.3.2.6
$E_{cd} = E_{cm} / \gamma_{cE}$ acc. to Eq. (33)
E_{cm} acc. to Eq. (10) and Eq. (11)
$\gamma_{cE} = 1.2$ acc. to 4.2.1.17

Reinforcing steel acc. to SIA 262, 4.2.2.2, Figure 16
with $f_{sd} = f_{sk}/\gamma_s$ acc. to Eq. (4); $\gamma_s = 1.15$ acc. to 2.3.2.6
$k_s = 1.05$ and $\varepsilon_{uk} = 2$ % acc. to Table 9, Column A
$E_s = 205000$ MN/m² acc. to Figure 16

Stress-strain curves according to SIA 262

Stress-Strain-Curves for the Serviceability Check

The serviceability check is based on the average strengths of the materials. The partial safety factors are assumed to be 1.0. The stress-strain curves of prestressing steel have a rising branch with E_p and a horizontal upper branch at $f_{p0,1k}$ or β_s.

Concrete with linear stiffness in the compression zone without failure limit

Reinforcing steel acc. to DIN 1045:1988, Figure 12
$E_s = 210000$ MN/m² acc. to 6.2.1
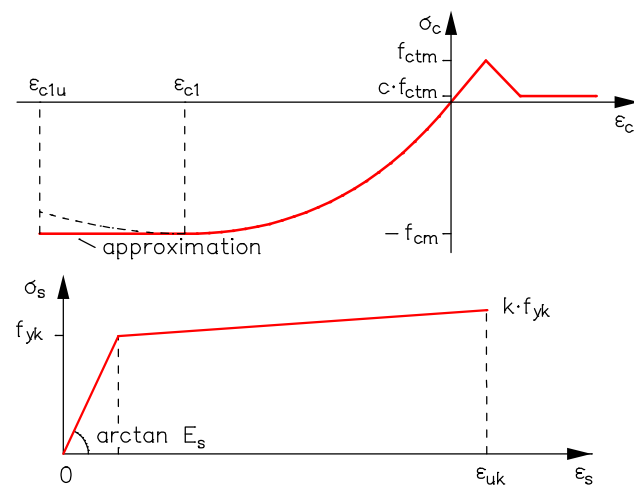
Stress-strain curves according to DIN 1045

Concrete acc. to DIN 1045-1, 9.1.5
σ_c acc. to Equation (62) or Figure 22 for $0 \geq \varepsilon_c \geq \varepsilon_{c1}$
with $f_{cm} = f_{ck} + 8$ (N/mm²) or $f_{lcm} = f_{lck} + 8$ (N/mm²)
instead of f_c and E_{c0m} or E_{lc0m} instead of E_{c0}

Reinforcing steel acc. to DIN 1045-1, 9.2.3 Figure 26
$k = 1.05$; $\varepsilon_{uk} = 2.5$% acc. to Table 11, Column 1 or 2
$E_s = 200.000$ MN/m² acc. to 9.2.4 (4)

Stress-strain curves according to DIN 1045-1

Concrete acc. to EN 1992-1-1, 3.1.5
σ_c acc. to Equation (3.14) for $0 \geq \varepsilon_c \geq \varepsilon_{c1}$ or ε_{lc1}
with $f_{cm} = f_{ck} + 8$ (N/mm²) acc. to Table 3.1
or f_{lcm} acc. to Table 11.3.1
and E_{cm} or E_{lcm} as specified

Reinforcing steel acc. to EN 1992-1-1, 3.2.7 Figure 3.8
$k = 1.05$; $\varepsilon_{uk} = 2.5\%$ acc. to Table C.1, Column A
$E_s = 200000$ MN/m² acc. to 3.2.7 (4)
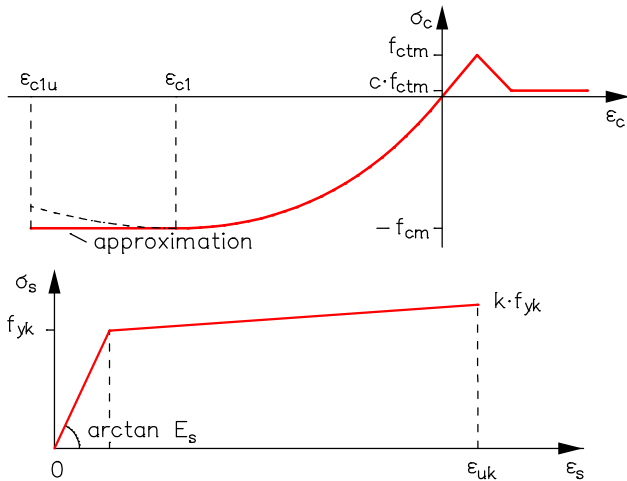
Stress-strain curves according to EN 1992-1-1

Concrete acc. to DIN EN 1992-1-1, 3.1.5
σ_c acc. to Equation (3.14) for $0 \geq \varepsilon_c \geq \varepsilon_{c1}$ or ε_{lc1}
with $f_{cm} = f_{ck} + 8$ (N/mm²) acc. to Table 3.1
or f_{lcm} acc. to Table 11.3.1
and E_{cm} or E_{lcm} as specified

Reinforcing steel acc. to DIN EN 1992-1-1, 3.2.7 Figure 3.8
$k = 1.05$; $\varepsilon_{uk} = 2.5\%$
$E_s = 200000$ MN/m²
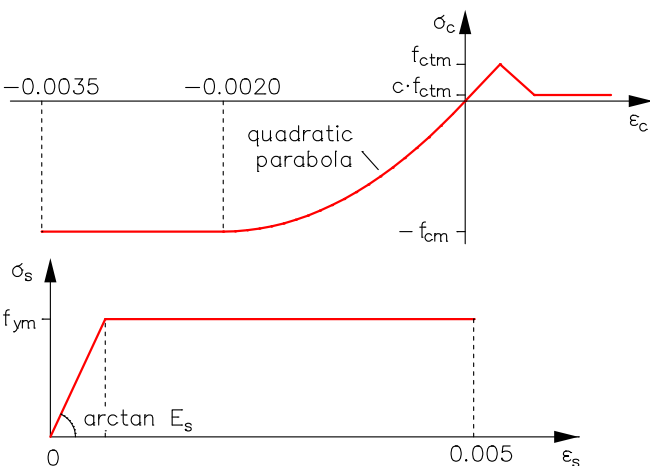
Stress-strain curves according to DIN EN 1992-1-1

Concrete acc. to OENORM B 4700, 3.4.1.1 Figure 7
with $f_{cm} = f_{ck} + 7.5$ (N/mm²) acc. to Equation (10c) and
$f_{ck} = 0.75 \cdot f_{cwk}$ acc. to 3.4.1.1 (2)

Reinforcing steel acc. to OENORM B 4700, 3.4.1.2 Figure 9
with $f_{ym} = f_{yk} + 10$ (N/mm²) acc. to Equation (10d)
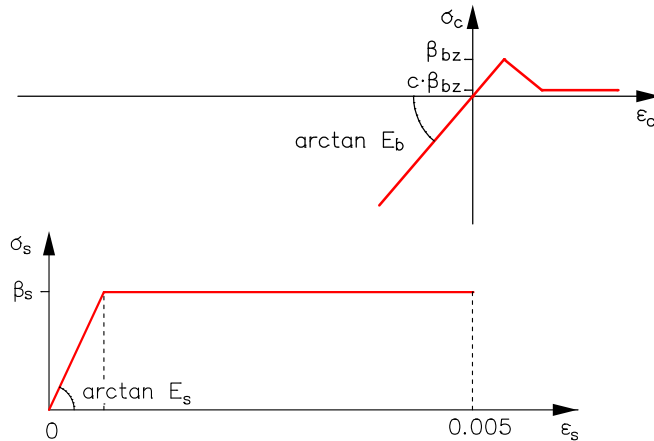$E_s = 200000$ MN/m² acc. to Figure 9
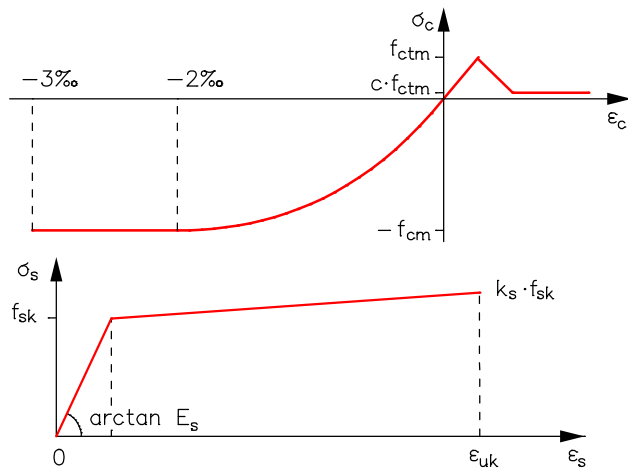
Stress-strain curves according to OENORM B 4700

Concrete acc. to SIA 262, 4.2.1.6 and Figure 12
σ_c acc. to Equation (28) for $0 \geq \varepsilon_c \geq -2$ ‰ with
$f_{cm} = f_{ck} + 8$ (N/mm²) acc. to Eq. (6) instead of f_{cd}
E_{cm} acc. to Eq. (10) and Eq. (11) instead of E_{cd}

Reinforcing steel acc. to SIA 262, 4.2.2.2, Figure 16
with f_{sk} instead of f_{sd}
$k_s = 1.05$ and $\varepsilon_{uk} = 2$ % acc. to Table 9, Column A
$E_s = 205000$ MN/m² acc. to Figure 16

Stress-strain curves according to SIA 262

Torsional Stiffness

When calculating the torsional stiffness of the section, it is assumed that it decreases at the same rate as the bending stiffness.

$$GI_{x,II} = \frac{1}{2} \cdot GI_{x,I} \cdot \left(\frac{EI_{y,II}}{EI_{y,I}} + \frac{EI_{z,II}}{EI_{z,I}} \right)$$

The opposite case, meaning a reduction of the stiffnesses as a result of torsional load, cannot be analyzed. The physical nonlinear analysis of a purely torsional load is also not possible for reinforced concrete.

Check of the Limit Strains (Ultimat Limit State Check)

After completion of the equilibrium iteration the permissible limit strains for concrete and reinforcing steel are checked in the case of structures consisting only of beam elements, if the *Newton* analysis method is used. If the permissible values are exceeded the reinforcement will be increased or the load-bearing capacity will be reduced.

Automatic Reinforcement Increase (Ultimate Limit State Check)

If requested an automatic increase of reinforcement can be made for structures consisting only of beam elements with the *Newton* analysis method to reach the full load-bearing capacity. Initially based on the desired start reinforcement the reachable load level is determined. If the reached load-bearing capacity considering the limit strains is lower then 100%, the reinforcement will be increased and the iteration starts again. If no load-bearing capacity exists because of insufficient start reinforcement a base reinforcement can be specified within the reinforcing steel definition and the design can be performed again.

Concrete Creep

The consideration of concrete creep in nonlinear analysis is realized by modifying the underlying stress-strain curves. These are scaled in strain-direction with the factor $(1+\varphi)$. Also the corresponding limit strains are multiplied by $(1+\varphi)$. The following figure shows the qualitative approach.
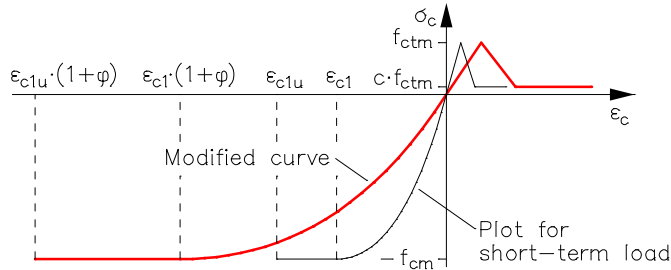
The described procedure postulates that the creep-generating stresses remain constant during the entire creep-period. Due to stress redistributions, for example to the reinforcement, this can not be guaranteed. Therefore an insignificant overestimation of the creep-deformations can occur.

Stress relaxation during a constant strain state can also be modelled by the described procedure. It leads, however, to an overestimation of the remaining stresses due to the non-linear stress-strain curves.

The nonlinear concrete creep can be activated in the '*Load group*' dialog.

This analysis approach applies analogous for area elements.

The plausibility of the achievable calculation results as well as the mode of action of different approaches for the concrete tensile strength and the *tension stiffening* are demonstrated by some examples in the '*Examples*' section.

Steel Beams

The section geometry is determined by the polygon boundary. In order to perform the section analysis, the program internally generates a mesh. The implemented algorithm delivers all section properties, stresses and internal forces on the basis of the quasi-harmonic differential equation and others.

The shear load is described by the following boundary value problem:

$$\frac{\partial^2 \varphi}{\partial y^2} + \frac{\partial^2 \varphi}{\partial z^2} = 0 \qquad \text{(Differential equation)}$$

$$\tau_{xn} = 0 \qquad \text{(Boundary condition)}$$

$$\sqrt{\sigma_x{}^2 + 3\tau_{xy}{}^2 + 3\tau_{xz}{}^2} - \sigma_{R,d} = 0 \qquad \text{(Yield criterion)}$$
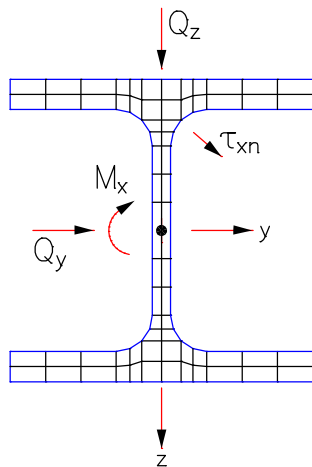
Steel cross-section with internal mesh

The differential equation holds equally for Q_y, Q_z and M_x. Depending on the load, the boundary condition delivers different boundary values of the solution function φ. The solution is arrived at by integral representation of the boundary value problem and discretization through finite differential equation elements. The internal forces are determined by numerical integration of the stresses across the section under consideration of the Huber-von Mises yield criterion. The interaction of all internal forces can be considered.

At the ultimate limit state, the material safety factor γ_M is taken into account as follows:

- Construction steel according to DIN 18800 and the general material type *Stahl*:
  The factor γ_M of the fundamental combination according to DIN 18800 is decisive.

- Construction steel according to EN 10025-2:
  In accordance with EN 1993-1-1, Chapter 6.1 (1), γ_M is assumed to be $\gamma_{M0} = 1.0$.

The serviceability check is generally calculated with a material safety factor of $\gamma_M = 1.0$.

On the basis of DIN 18800, the interaction between normal and shear stresses is considered only when one of the following three conditions is met:

$$Q_y \geq 0.25 \cdot Q_{pl,y,d}$$

$$Q_z \geq 0.33 \cdot Q_{pl,z,d}$$

$$M_x \geq 0.20 \cdot M_{pl,x,d}$$

Limiting the bending moments $M_{pl,y,d}$ and $M_{pl,z,d}$ according to DIN 18800 to 1.25 times the corresponding elastic limit moment does not occur.

Stability failure due to cross-section buckling or lateral torsional buckling is not taken into account.

Beams of Free Material

For polygon sections of the general material type *Frei*, the following bilinear stress-strain curve with user-defined tensile strength ($f_{y,tension}$) and compressive strength ($f_{y,compression}$) is used.
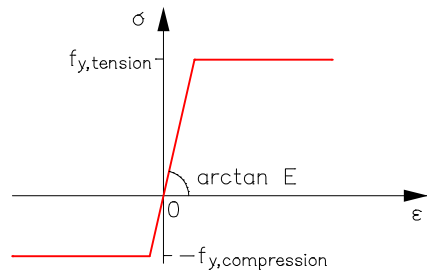
Stress-strain curve for the material type Frei

Due to the differing strengths in the compressive and tensile section, the Huber-von Mises yield criterion is not used here. The interaction of normal and shear stresses is also not accounted for.

Area Elements

So-called layer elements are used to enable the integration of nonlinear stresses across the area section. This is done by determining the stresses in each layer according to the plain stress theory, two-dimensional stress state, under consideration of the physical nonlinearities. The integration of the stresses to internal forces is carried out with the help of the trapezoidal rule.

$$n_x = t \cdot \left(\sigma_{xo} + \sigma_{xn} + 2 \cdot \sum_{i=1}^{n-1} \sigma_{xi} \right) \qquad m_x = t \cdot \left(\sigma_{xo} \cdot z_o + \sigma_{xn} \cdot z_n + 2 \cdot \sum_{i=1}^{n-1} \sigma_{xi} \cdot z_i \right)$$

$$n_y = t \cdot \left(\sigma_{yo} + \sigma_{yn} + 2 \cdot \sum_{i=1}^{n-1} \sigma_{yi} \right) \qquad m_y = t \cdot \left(\sigma_{yo} \cdot z_o + \sigma_{yn} \cdot z_n + 2 \cdot \sum_{i=1}^{n-1} \sigma_{yi} \cdot z_i \right)$$

$$n_{xy} = t \cdot \left(\tau_{xyo} + \tau_{xyn} + 2 \cdot \sum_{i=1}^{n-1} \tau_{xyi} \right) \qquad m_{xy} = t \cdot \left(\tau_{xyo} \cdot z_o + \tau_{xyn} \cdot z_n + 2 \cdot \sum_{i=1}^{n-1} \tau_{xyi} \cdot z_i \right)$$
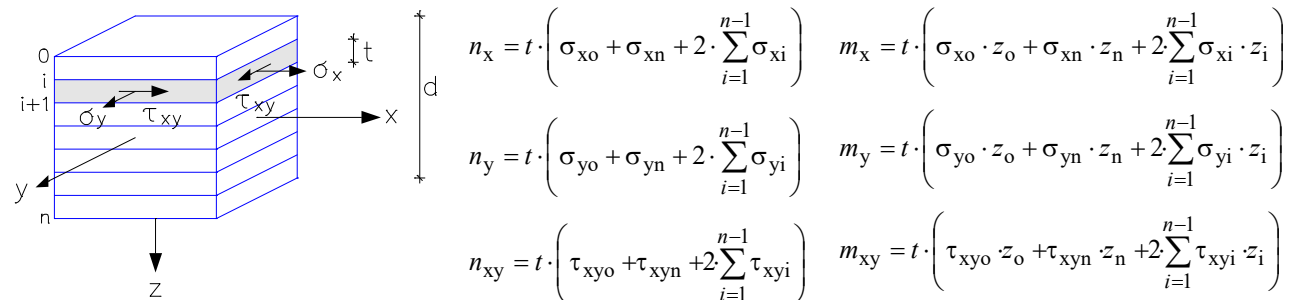
Reinforced Concrete Area Elements

The biaxial concrete behavior is realized with the help of the concept of equivalent one-axial strains (Finite Elemente im Stahlbetonbau (Finite Elements in Reinforced Concrete Construction), Stempniewski and Eibl, Betonkalender 1993). The existing strain state is first transformed into the principal direction in each corresponding layer and then reformed to the equivalent relationship of the form

$$
\begin{Bmatrix} \sigma_{11} \\ \sigma_{22} \\ \sigma_{12} = 0 \end{Bmatrix} = \frac{1}{1-\nu^2} \begin{Bmatrix} E_1 & \nu\cdot\sqrt{E_1\cdot E_2} & 0 \\ \nu\cdot\sqrt{E_1\cdot E_2} & E_2 & 0 \\ 0 & 0 & (1-\nu^2)\cdot G \end{Bmatrix} \begin{Bmatrix} \varepsilon_{11} \\ \varepsilon_{22} \\ \varepsilon_{12} = 0 \end{Bmatrix}
$$

with

$$\varepsilon_{c,1} = \varepsilon_{11} + \nu\cdot\sqrt{\frac{E_2}{E_1}}\cdot\varepsilon_{22}$$

$$
= \frac{1}{1-\nu^2} \begin{Bmatrix} E_1 & 0 & 0 \\ 0 & E_2 & 0 \\ 0 & 0 & (1-\nu^2)\cdot G \end{Bmatrix} \begin{Bmatrix} \varepsilon_{c,1} \\ \varepsilon_{c,2} \\ \varepsilon_{12} = 0 \end{Bmatrix}
$$

$$\varepsilon_{c,2} = \nu\cdot\sqrt{\frac{E_1}{E_2}}\cdot\varepsilon_{11} + \varepsilon_{22}$$

$$G = \frac{1}{4\cdot(1-\nu^2)}\left[E_1 + E_2 - 2\cdot\nu\sqrt{|E_1\cdot E_2|} \right]$$

The shear modulus G is considered to be direction independent in this approach. The poisson's ratio ν is assumed to be constant.

The required tangential stiffnesses E_1 and E_2 and equivalent biaxial concrete compressive stresses $\sigma_{c,i}$ are iterated using the Saenz curve

$$\sigma_{c,i} = \frac{E_{c0}\cdot\varepsilon_{c,i}}{1 + \left(\dfrac{E_{c0}}{E_{cS,i}} - 2\right)\dfrac{\varepsilon_{c,i}}{\varepsilon_{cB,i}} + \left(\dfrac{\varepsilon_{c,i}}{\varepsilon_{cB,i}}\right)^2}$$

with $i = 1, 2$ (principal directions)

under consideration of the biaxial stiffnesses according to Kupfer/Hilsdorf/Rüsch.

Only when checking the serviceability according to DIN 1045 it is assumed that the compressive area exhibits a linear elastic material behavior.

Parameters for the stress-strain relationship used are:

- Initial stiffness E_{c0} of the one-axial stress-strain curve of the selected concrete.

- Equivalent biaxial concrete strains $\varepsilon_{c,i}$

- Factor of the biaxial failure curve k_i according to Kupfer/Hilsdorf/Rüsch depending on $\sigma_{c,1} / \sigma_{c,2}$.

- Secant stiffness $E_{cS,i} = f_{cB,i} / \varepsilon_{cB,i}$ when the biaxial concrete compressive strength $f_{cB,i}$ is reached.

- Biaxial concrete compressive strength $f_{cB,i} = k_i \cdot f_c$

- Concrete compressive strength f_c of the one-axial stress-strain curve of the selected concrete. The values described in the section *Reinforced concrete beams* are used.

- Compression $\varepsilon_{cB,i}$ when $f_{cB,i}$ is reached. The value $\varepsilon_{cB,i}$ is derived from the function parameters k_i and ε_{c1} according to Darwin and Pecknold.

- Compression ε_{c1} when the strength f_c of the one-axial stress-strain curve of the selected concrete is reached.
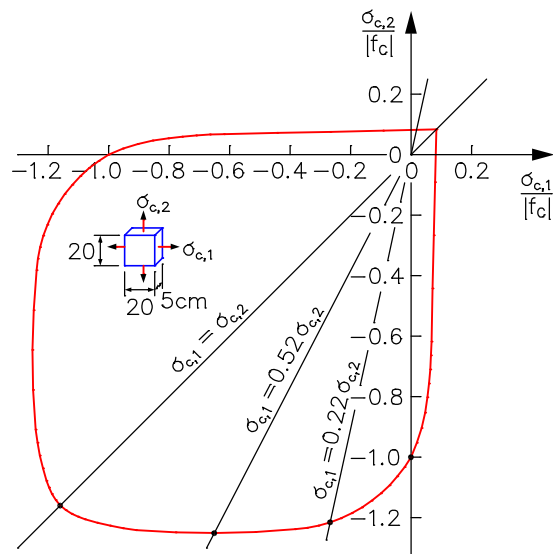
Biaxial failure curve according to Kupfer/Hilsdorf/Rüsch
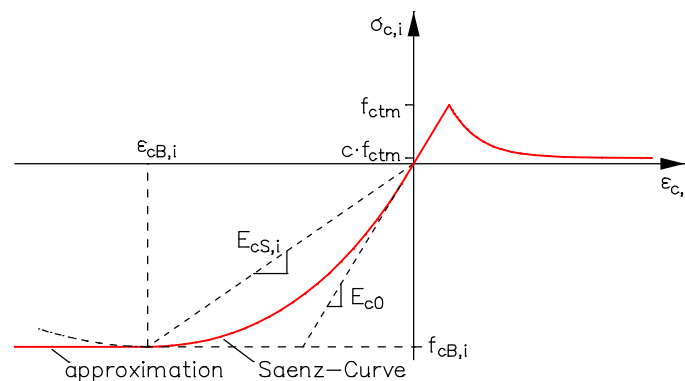
Standardized equivalent one-axial stress-strain curve for concrete
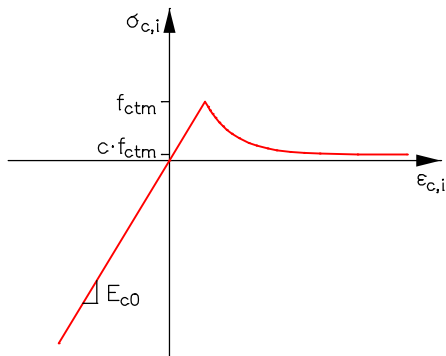
Stress-strain curve for the serviceability check according to DIN 1045

The consideration of the concrete creep occurs analog to the procedure for beams through modification of the underlying stress-strain curves and can be activated in the '*Load group*' dialog.

Interaction with the shear stresses from the lateral forces is not considered here. During the specification of the crack direction the so-called 'rotating crack model' is assumed, meaning that the crack direction can change during the nonlinear iteration as a function of the strain state. Conversely, a fixed crack direction after the initial crack formation can lead to an overestimation of the load-bearing capacity.

The Finite Element module currently does not check the limit strain nor does it automatically increase reinforcement to improve the load-bearing capacity due to the significant numerical complexity.

For clarification of the implemented stress-strain relationships for concrete, the curves measured in the biaxial test according to Kupfer/Hilsdorf/Rüsch are compared with those calculated using the approach described above.
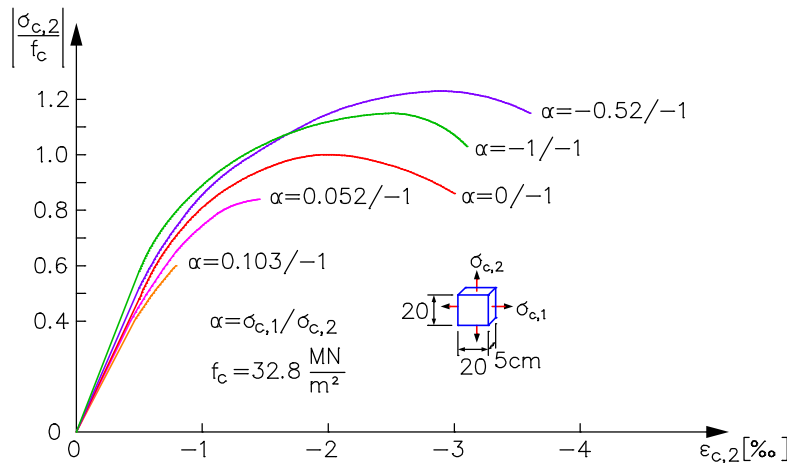
Biaxial test according to Kupfer/Hilsdorf/Rüsch
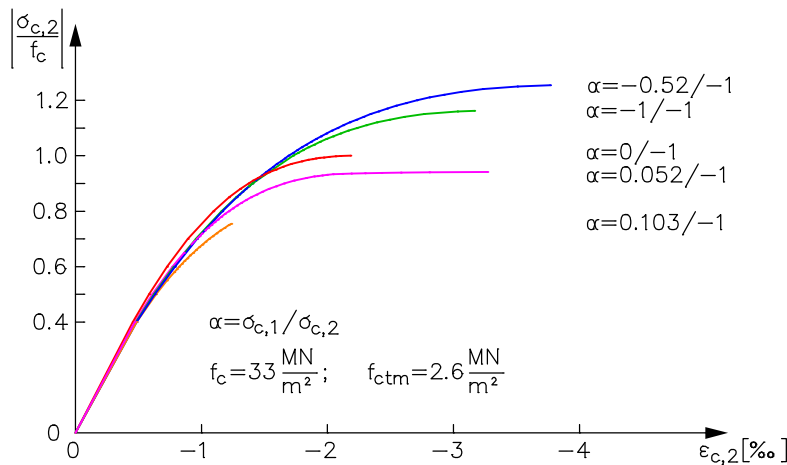
Calculation results for C25/30; f_{cm} = 25 + 8 = 33 MN/m²

The existing **reinforcing steel** is modeled as a 'blurred' orthogonal reinforcement mesh. The corresponding strain state is transformed into the reinforcement directions (p, q) of the respective reinforcing steel layer. The stress-strain curve of the selected reinforced concrete standard is used to determine the stress.
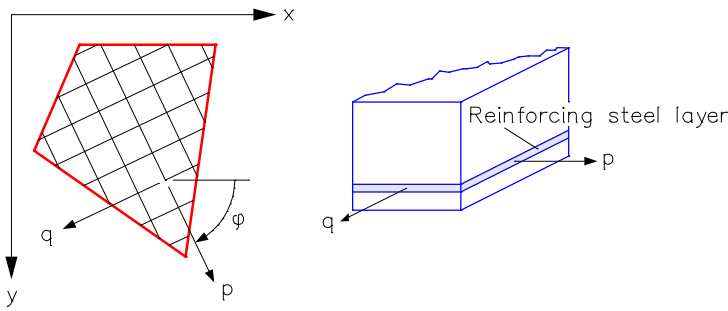
Area Elements of Steel and Free Material

For area elements made of steel the Huber v.Mises yield criterion is used. The material safety factor specified in the section *Steel beams* apply accordingly. For area elements of the material type *Frei*, the *Raghava* yield criterion, as described below, or the *Rankine* yield criterion can be chosen.

$$F = J_2 - 1/3 \cdot f_c \cdot f_t + (f_c - f_t) \cdot \sigma_m = 0$$

with

$$\sigma_m = 1/3 \, (\sigma_x + \sigma_y + \sigma_z)$$

$$J_2 = 1/2 \, ({\sigma'}_x^2 + {\sigma'}_y^2 + {\sigma'}_z^2) + \tau_{xy}^2 + \tau_{yz}^2 + \tau_{zx}^2$$

$$\sigma'_x = \sigma_x - \sigma_m$$

$$\sigma'_y = \sigma_y - \sigma_m$$

$$\sigma'_z = \sigma_z - \sigma_m$$

Starting from the strain state, a layer is iterated on the yield surface with the help of a 'backward Euler return' that, in conjunction with the Newton-Raphson method, ensures quadratic convergence. (Non-linear Finite Element Analysis of Solids and Structures, M.A. Crisfield, Publisher John Wiley & Sons).

The yield surface mentioned above is illustrated below for the 2D stress state, as used for layer elements, for the principal stresses σ_1 and σ_2 as well as for the components σ_x, σ_y and τ_{xy}.

In this example $f_c = 20$ MN/m² and $f_t = 2$ MN/m².
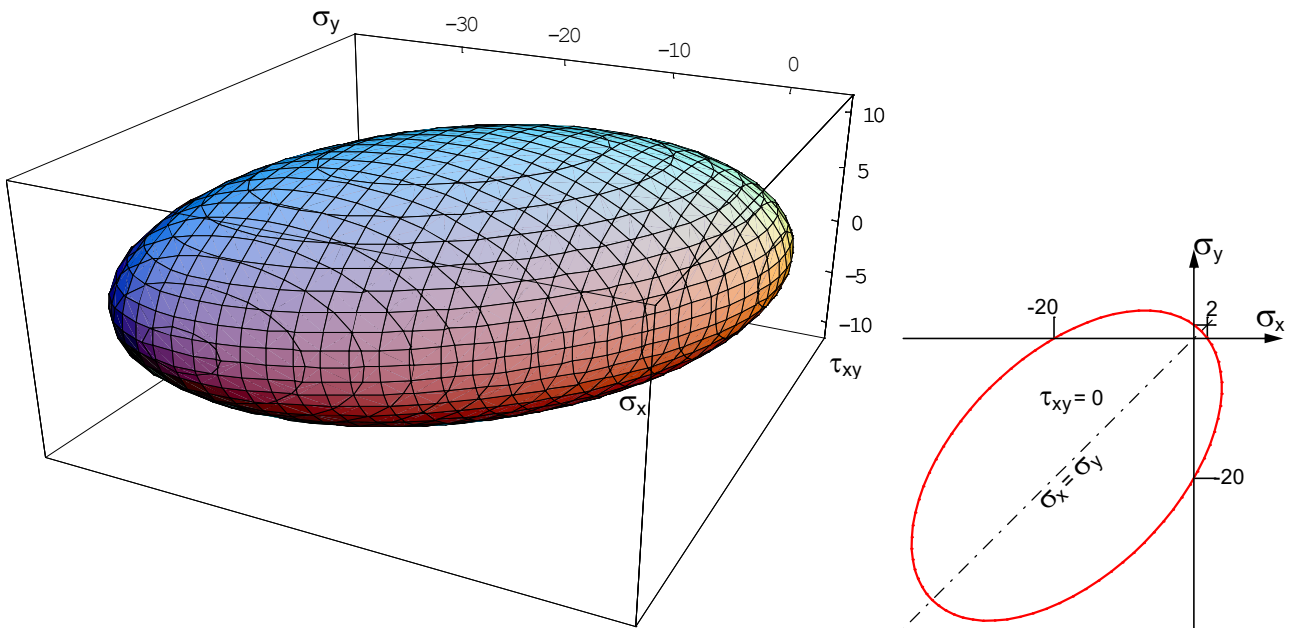
Yield surface for the 2D stress state according to Raghava

Solid Elements

A distinction is made between solid elements made of steel, a standardized concrete type and solid elements with the material type *Frei*.

For solid elements made of the first two material types, the yield criterion according to *Raghava* (ideal plastic) is used. For the standardized concrete types, the compressive strength f_c is set to f_{ck} in the serviceability and to f_{cd} in the ultimate limit state. Softening of the material in tension is not currently supported for these material types.

If, on the other hand, a structure is discretized with solid elements of the material type *Frei*, three different model approaches are available to represent the nonlinear material behavior (i.a. with hardening and softening in tension and compression). Depending on the problem to be analyzed, the numerical calculation can be carried out either by using pure damage and plasticity models or a combination of plasticity and damage. Damage surfaces, yield criteria and all parameters associated with the respective model are to be selected or adapted in the dialog for the material properties. An isotropic material behavior is assumed for all models.

In the following, the model approaches (damage, plasticity and combined model) are briefly described. Detailed derivations etc. can be found in a large number of publications

[e.g. *Kachanov* (1958, 1986), *Chaboche* (1981), *Lemaitre & Chaboche* (1990), *Chen & Han* (1988)].

Damage

The constitutive relations of a isotropic damage model are as follows:

$$\sigma = (1-D) \cdot C : \varepsilon = (1-D) \cdot \overline{\sigma}, \quad (C: \text{elasticity tensor}, \varepsilon: \text{strain tensor}) \tag{V1}$$

where $\overline{\sigma}$ are denoted as effective and σ as nominal stresses. The degradation of the material is determined using the scalar damage parameter $D(\eta)$, which is calculated here as a function of the equivalent strain η. In *InfoCAD* only exponential functions are used to represent the loss of stiffness. All functions have in common that the damage parameter takes the value zero ($D = 0 \rightarrow \sigma = C : \varepsilon$) for undamaged material and the value one ($D = 1 \rightarrow \sigma = 0$) for completely damaged material.

InfoCAD provides two damage models, the *De Vree et al.* (1995) model and the *Mazars et al.* (2015) model. The models differ both in the shape of the damage surface and in the equation used to calculate the damage parameter. As a result, materials with both identical (*De Vree*) and different (*Mazars*) tension-compression behavior can be modeled. A method for minimizing mesh dependency is not currently considered in either model.

De Vree

In the *De Vree* model, elastic material behavior is assumed until the maximum tensile (f_t) and compressive (f_c) stresses are reached. The stress-strain curve after reaching the respective yield stress (softening) is also qualitatively identical. In InfoCAD, a combination of equivalent strain according to *De Vree et al.* (1995)

$$\eta = K_1 \cdot I_1 + \sqrt{(K_1 \cdot I_1)^2 + K_2 \cdot J_2}, \quad \text{with:} \quad \begin{matrix} K = \dfrac{f_c}{f_t}, \quad K_1 = \dfrac{K-1}{2K \cdot (1-2\nu)}, \quad K_2 = \dfrac{3}{K \cdot (1+\nu)^2} \\ I_1 = \varepsilon_1 + \varepsilon_2 + \varepsilon_3 \quad \text{(1. invariant of the strain tensor)} \\ J_2 = [(\varepsilon_1 - \varepsilon_2)^2 + (\varepsilon_2 - \varepsilon_3)^2 + (\varepsilon_3 - \varepsilon_1)^2]/6 \quad \text{(2. deviatoric invariant)} \end{matrix} \tag{V2}$$

and exponential damage function according to *Peerlings* (1999)

$$D(\eta) = 1 - (1-A) \cdot \frac{\eta_0}{\eta} - A \cdot \frac{\eta_0}{\eta} \cdot \exp(B \cdot (\eta_0 - \eta)), \quad \text{with:} \quad \eta_0 = \frac{f_t}{E} \tag{V3}$$

is used, where $D(\eta) = 0$ if $\eta \leq \eta_0$. In the latter formulation, the residual tensile or compressive strength is controlled by parameter A ($\sigma^{res} = (1 - A) \cdot \sigma_{c,t}$) and the damage evolution (slow or fast increase of damage) by parameter B, see Figure 1.

$E = 30000$ MPa
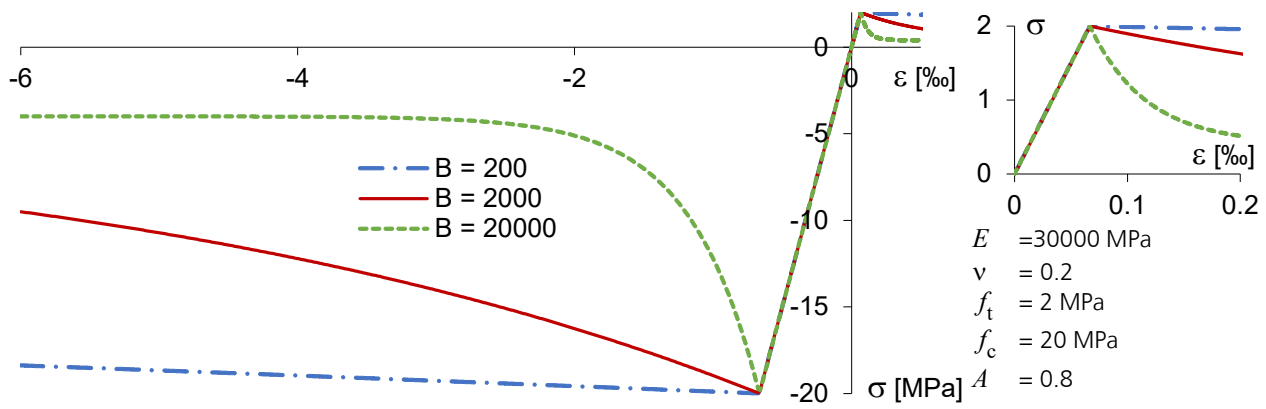$\nu = 0.2$
$f_t = 2$ MPa
$f_c = 20$ MPa
$A = 0.8$

Figure 1:   Uniaxial stress-strain diagram (de Vree / Peerlings)

With increasing stiffness degradation, the damage asymptotically approaches the value 1. In addition to the three-dimensional view, Figure 2 also shows the damage surface for the plane stress state (σ_3=0). Based on this (cf. with *Kupfer et al.* (1969)) and the uniaxial stress-strain relationship, it becomes clear that the compressive behavior of concrete cannot be adequately represented with this damage model.

3D view   *Stress state with constant σ_3*

× Kupfer et al. (1969)
$\sigma_3 = 2$
$\sigma_3 = 0$
$\sigma_3 = -2$
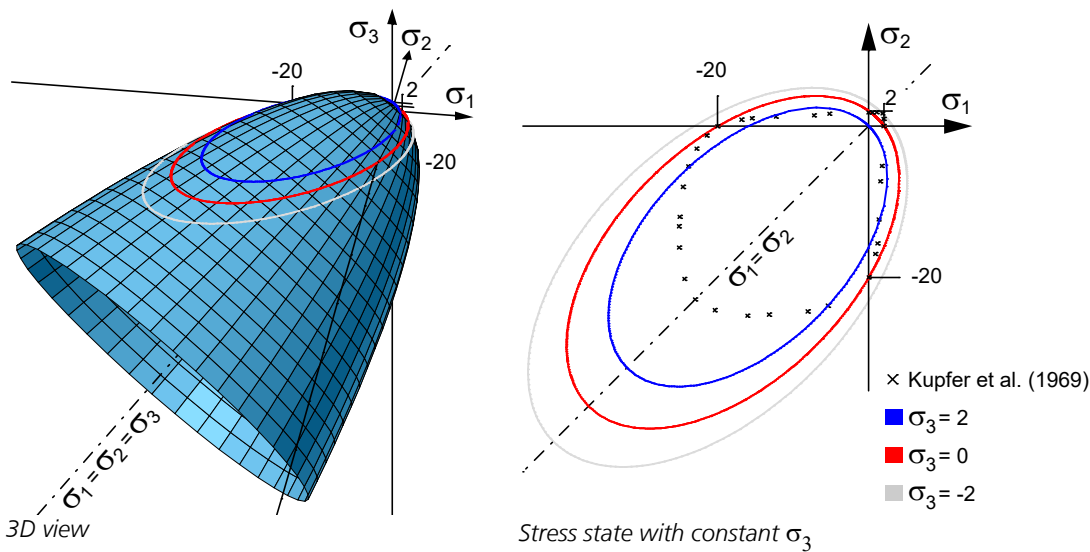
Figure 2:   Damage (de Vree) in the principal stress space, f_c = 20 MPa, f_t = 2 MPa

On the one hand, the nonlinear relationship between stresses and strains is not reproduced realistically, this applies both before and after reaching the compressive strength f_c, and on the other hand, the compressive-compressive failure is significantly overestimated. However, problems with dominant tensile failure can be predicted with sufficient accuracy using this model. The counterpart to *De Vree's* damage surface is the yield surface according to *Raghava* (1973) (or *Mises-Schleicher* (1926)) in the case of plastic material behavior, see Figure 9. In analogy to the yield surface (*Raghava → Mises*), in the plane stress state (σ_3=0) the damage surface degenerates to an ellipse symmetrical to the stress origin for identical values of tensile and compressive strength ($f_t = f_c \rightarrow K = 1$, see Eq. V2).

Mazars' μ-Model

The second isotropic damage model implemented in InfoCAD is based on the publications of *Mazars et al.* (2015, 2017). The equivalent strains are determined separately for tension (η_t) and compression (η_c):

$$\eta_t = \frac{I_1}{2 \cdot (1-2\nu)} + \frac{\sqrt{J_e}}{2 \cdot (1+\nu)} \quad \text{and} \quad \eta_c = \frac{I_1}{5 \cdot (1-2\nu)} + \frac{6 \cdot \sqrt{J_e}}{5 \cdot (1+\nu)}, \text{ with } J_e = \left[(\varepsilon_1 - \varepsilon_2)^2 + (\varepsilon_2 - \varepsilon_3)^2 + (\varepsilon_3 - \varepsilon_1)^2 \right] / 2 \quad \text{(V4)}$$

The triaxial factor r (*Lubliner et al.* 1989) is subsequently used to calculate the equivalent total strain corresponding to the respective stress state:

$$\eta = r \cdot \eta_t + (1-r) \cdot \eta_c, \qquad \text{with: } r = \sum_{i=1}^{3} \langle \sigma_i \rangle / \sum_{i=1}^{3} |\sigma_i|. \quad \text{(V5)}$$

Depending on the triaxial factor r and the respective parameters for generating the damage function in tension (A_t, B_t) and compression (A_c, B_c), a damage related to the three-dimensional stress state is formulated. With the two parameters A and B

$$A = (2 \cdot r^2 (1 - 2 \cdot k) - r \cdot (1 - 4 \cdot k)) \cdot A_t + (2 \cdot r^2 - 3 \cdot r + 1) \cdot A_c \tag{V6}$$

$$B = r^{r^2 - 2 \cdot r + 2} \cdot B_t + (1 - r^{r^2 - 2 \cdot r + 2}) \cdot B_c \tag{V7}$$

the damage parameter finally yields to:

$$D(\eta) = 1 - (1 - A) \cdot \frac{\eta_0}{\eta} - A \cdot \exp(B \cdot (\eta_0 - \eta)), \qquad \text{with: } \eta_0 = r \cdot \eta_{T0} + (1 - r) \cdot \eta_{C0} \tag{V8}$$

Also here applies: $D(\eta) = 0$ if $\eta \le \eta_0$. The shear parameter k is set to 0.7 according to the recommendation in *Mazars et al.* (2017). For the two limiting cases $r = 1$ (pure tension) and $r = 0$ (pure compression), the result is: $A = A_t$ and $B = B_t$ or $A = A_c$ and $B = B_c$, see Eqs. V6 and V7. In contrast to the tensile range, where damage to the material only starts when the maximum tensile stress f_t is reached, in the compressive range a loss of stiffness already occurs before the compressive strength f_c is reached.
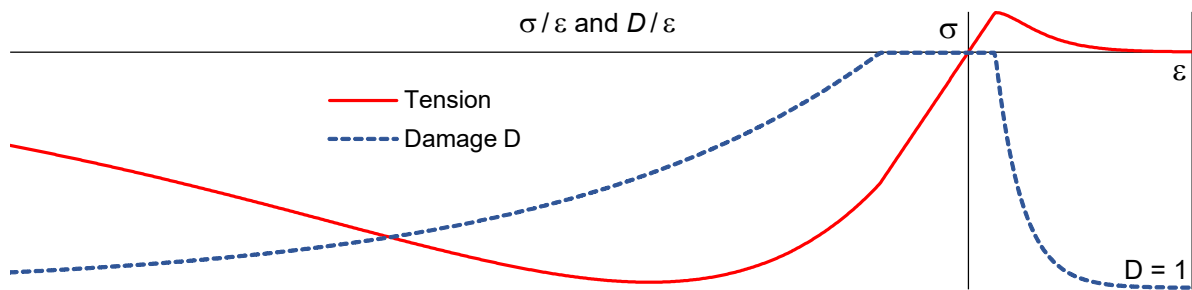
Figure 3:   Uniaxial stress-strain and damage-strain diagram (Mazars' µ-Model)

This is evident from both the damage surfaces (Figure 4) and the nonlinear stress-strain relationships even before the maximum value is reached (see Figure 3). Thus, in contrast to the *De Vree* model, the compressive behavior of concrete can also be represented satisfactorily. The factor η_0 / η, which was not considered by *Mazars et al.* (2015) in the third term of the damage function, is decisive for this, see Eqs. V3 and Gl. V8.

3D View   Plane stress state $\sigma_3 = 0$ sections parallel to the deviatoric plane
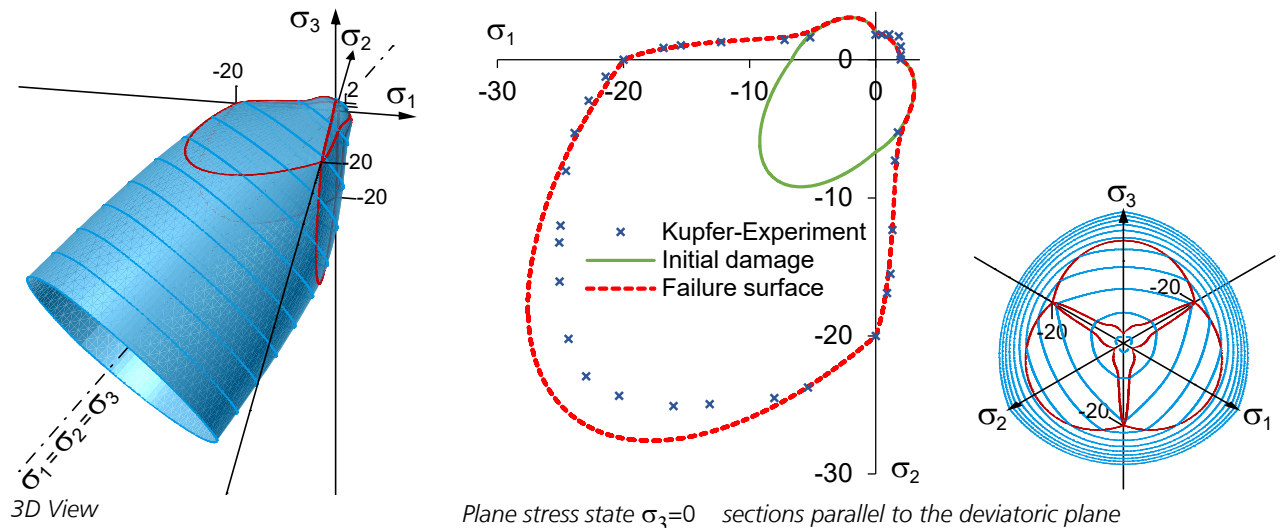
Figure 4:   Damage surface (Mazars' µ-Model) in the principal stress space, f_c = 20 MPa, f_t = 2 MPa

The respective threshold values η_{T0} (uniaxial tension) and η_{C0} (uniaxial compression) are defined as follows:

$$\eta_{T0} = \frac{f_t}{E} \qquad \text{and} \quad \eta_{C0} = \frac{10}{3} \cdot \eta_{T0} \tag{V9}$$

The compressive threshold value is 10/3 times the tensile threshold value (*Gafoor & Dinkler* 2020). Analogous to the exponential damage function according to *Peerlings* (Gl. V3), the residual strength is controlled with the parameters A_t (tension) and A_c (compression) and the stiffness degradation with the parameters B_t (tension) and B_c (compression). However, due to the changed function compared to *Peerlings* as well as the definition of the compression threshold η_{C0},

there are some dependencies that have to be considered when using the μ-model. First, since the compression range of the stress-strain relation is determined by the tensile strength f_t, the residual tensile strength is also defined by it:

$$\sigma_t{}^{res} = (1 - A_t) \cdot f_t \qquad \text{or} \qquad \sigma_c{}^{res} = (1 - A_c) \cdot \frac{10}{3} \cdot f_t \qquad\qquad \text{(V10)}$$

Secondly, the parameters A (A_t, A_c) and B (B_t, B_c) not only influence the residual load-carrying capacity and induce a fast or slow increase of the damage (see Figure 1), but also (with the exception of A_t) directly influence the maximum value of the compressive or tensile stress (f_c or f_t). This can be seen from the uniaxial relationships shown in Figure 5 (A_t and A_c constant) and Figure 6 (B_t and B_c constant).
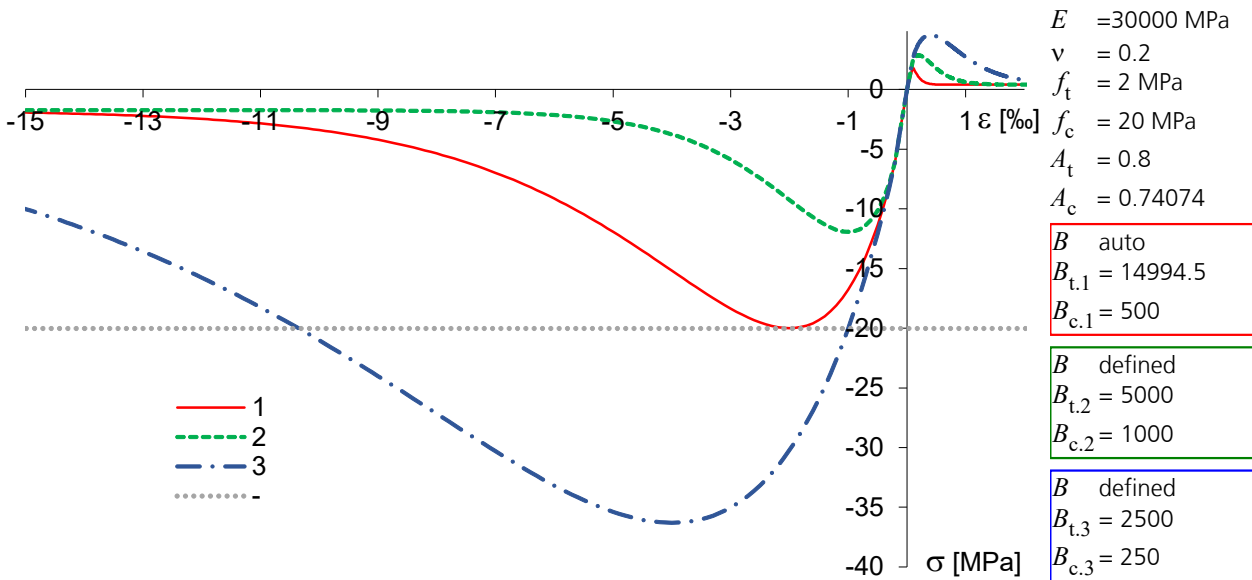
Figure 5: Uniaxial stress-strain diagram (Mazars' μ-Model). Influence of the parameter B.

In order to make both the input of the stress-strain relationship as flexible as possible and to guarantee compliance with the tensile and compressive strength selected in the dialog (without parameter study), two alternatives are available in InfoCAD. One with and one without entering the parameters B_t and B_c. With the input of both parameters, the selected tensile and compressive strength does not correspond to the maximum values of the stress-strain relationship (see 2 and 3 in Figures 5 and 6). Without input, on the other hand, i.e. if the check mark is removed from 'Enter B', the strengths previously defined in the dialog are automatically obtained (see 1 in Figures 5 and 6).
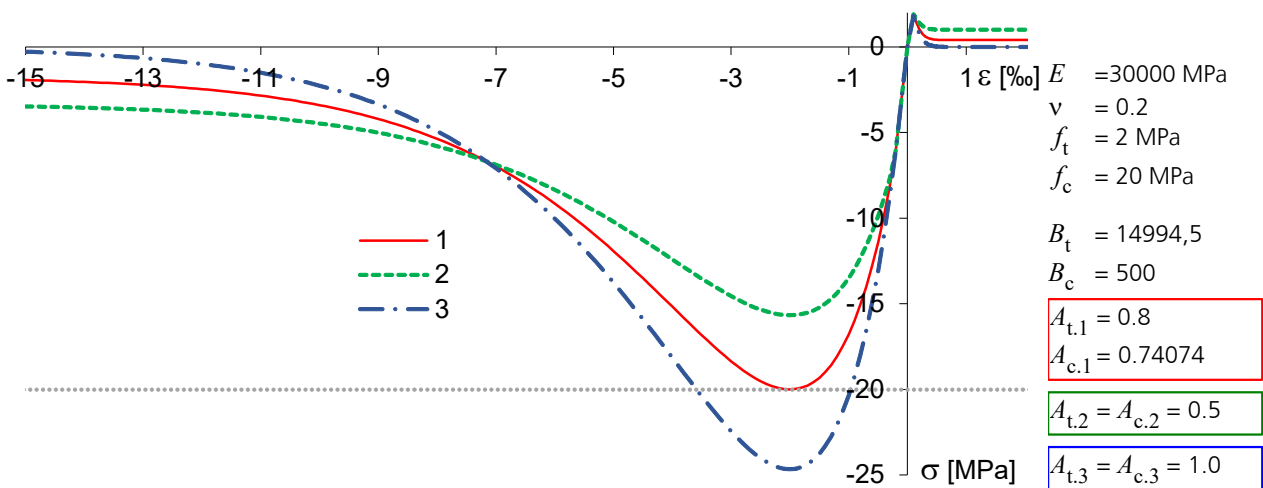
Figure 6: Uniaxial stress-strain diagram (Mazars' μ-Model). Influence of the parameter A.

In the standard case, the limit strain ε_1 results from the parameters selected in the dialog for the material properties. However, if the compressive strength f_c is to correspond to a certain limiting strain ε_1, it is necessary to adjust the compressive parameters A_c and B_c. For this purpose, B_c ($B_c = 1 / \varepsilon_1$) can first be determined and then the parameter A_c according to Equation V11:

$$A_c = (\eta_{C0} - f_c / E)/(\eta_{C0} - \exp(B_c \cdot \eta_{C0} - 1)/B_c) \qquad\qquad \text{(V11)}$$

Examples

To validate the μ-model implemented in InfoCAD and verify the numerically predicted stiffness degradation due to uniaxial and biaxial loading, a comparison is made with the results of *Mazars et al.* (2015) as well as a comparison with experimental results (*Kupfer et al.* 1969). Figure 8 shows the stress-strain relationship resulting from uniaxial load. *InfoCAD* gives the same results as published by *Mazars et al*. For completeness, it is noted that the damage thresholds are determined internally here (Eq. V9) and are not explicitly given as model parameters (η_{T0} and η_{C0}).
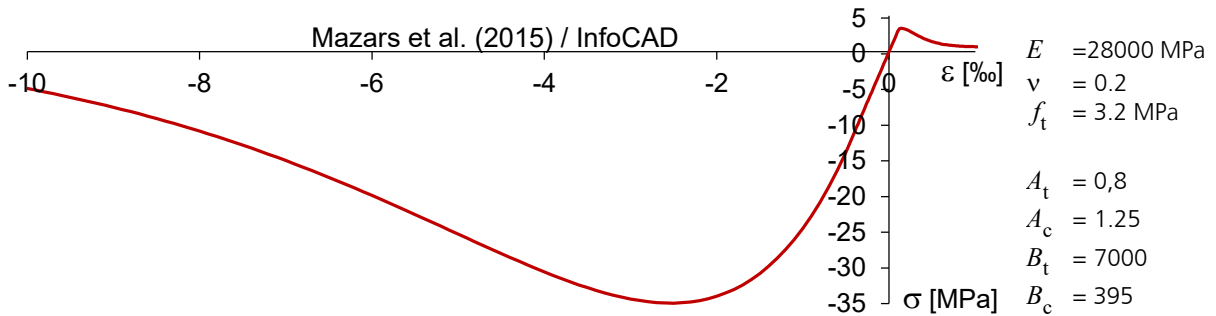
Figure 7: Uniaxial stress-strain relation (numerical)

The damage surface visualized in Figure 4 already shows that the biaxial failure curve of concrete (*Kupfer et al.*) can also be reproduced well with the μ-model. In order to additionally evaluate the quality of the numerically predicted stiffness degradation for a biaxial loading (plane stress state $\sigma_3=0$), corresponding finite element analyses were carried out and their results plotted together with the experimental results of *Kupfer et al.* in Figure 8. While all compressive components of the principal strains agree sufficiently accurately with the measured values, the tensile components in the region of the maximum values deviate from the recorded values. This is due to the fact that with an isotropic damage formulation, the poisson's ratio ν remains constant (*Mazars et al.*). In addition, this model slightly overestimates the biaxial compressive strength. Regarding the partial discrepancy between numerical and experimental results, it should be mentioned here again that the stress-strain relationship, as described in the previous sections, can be adapted to the existing material behavior at any time by changing the four damage parameters (A_t, B_t, A_c and B_c) as well as the tensile strength.

Tension-compression test   *Compression-compression test*

Figure 8: Two-axial stress-strain relationships. Comparison of numerical (— InfoCAD: Mazars' μ-model) and experimental (■ Kupfer et al.) results.
Parameters: f_t = 3.2 MPa, E = 30 GPa, ν = 0.2, A_t = 1, A_c = 1.25, B_t = 10000, B_c = 459

Plasticity

The yield criteria available in InfoCAD are explained below:

- *Raghava*
- *Huber-v.Mises*
- *Rankine*
- *Mohr-Coulomb*
- *Drucker-Prager*
- *Lubliner*

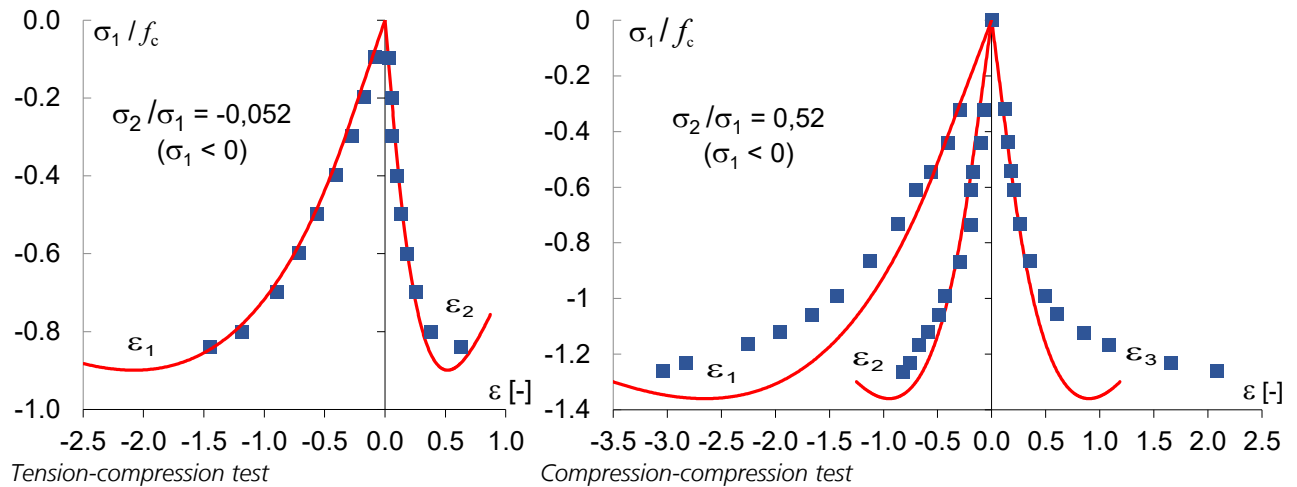The *Rankine*, *Mohr-Coulomb*, *Drucker-Prager* and *Lubliner* yield criteria are only available for solid elements with the material type *Frei*. The desired plasticity model can be selected in the material properties dialog.

It should be noted that the following equations do not take into account isotropic hardening. Initially, an ideal plastic material behavior is assumed. Explanations of the linear hardening considered in the FE program are given at the end of this section.

Due to the split of the strain tensor (ε) into an elastic (ε^{el}) and a plastic (ε^{pl}) part, the constitutive relations are defined as follows:

$$\sigma = C : \varepsilon^{el} = C : (\varepsilon - \varepsilon^{pl}), \ (C: \text{elasticity tensor}) \tag{V12}$$

Where the stresses here are also named effective stresses.

Raghava

For solid elements made of steel and standardized concrete, only the yield criterion according to *Raghava et al.* (1973), *Schleicher* (1926) is used:

$$F(\sigma) = J_2 + \alpha \cdot I_1 - \beta = 0, \qquad \begin{array}{l} \text{with } \alpha = (f_c - f_t)/3 \ , \ \beta = (f_c \cdot f_t)/3, \\ I_1 = \sigma_1 + \sigma_2 + \sigma_3 \text{ and } J_2 = [(\sigma_1 - \sigma_2)^2 + (\sigma_2 - \sigma_3)^2 + (\sigma_3 - \sigma_1)^2]/6 \end{array} \tag{V13}$$

Figure 9 shows the yield surface in the principal stress space. To illustrate the difference to the biaxial failure curve according to *Kupfer et al.* (1969), the yield surface in the plane stress state (σ_3=0) is shown in addition to the three-dimensional surface.

3D view   *Stress state with constant σ_3*

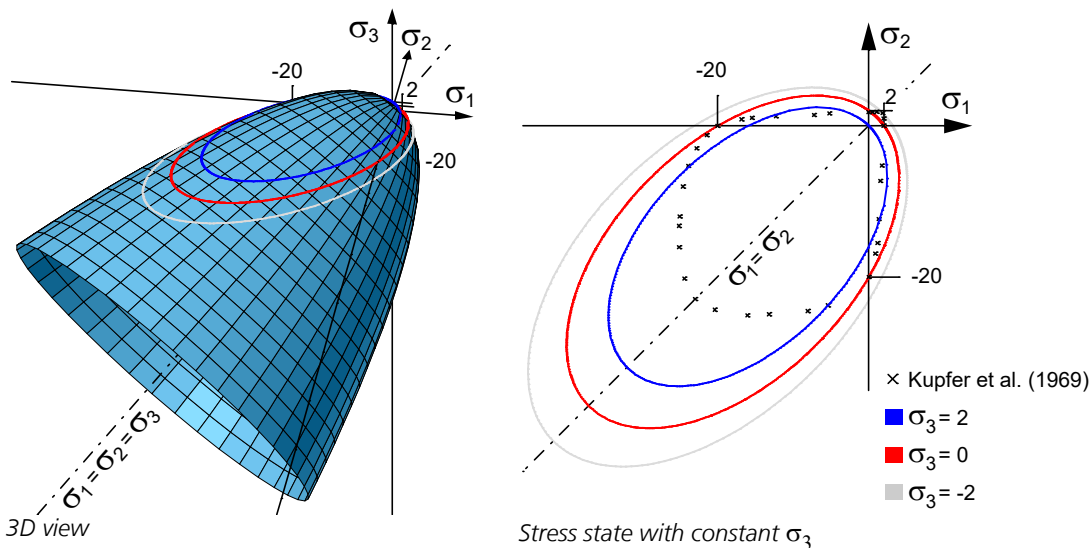*Figure 9: Yield surface according to Raghava in the principal stress space, f_{ck} = 20 MPa, f_{ctm} = 2 MPa*

Analogous to the *De Vree* damage model (Figure 2), the compression-compression zone for concrete is significantly overestimated.

Huber-v.Mises

If tensile and compressive strength are identical ($f_c = f_t = \sigma_y$), the yield criterion of *Raghava et al.* (1973) is equivalent to the *Huber-v. Mises* yield criterion:

$$F(\sigma) = J_2 - \sigma_y^2 / 3 = 0 \tag{V14}$$

The representation of the yield surface in the principal stress space results in the typical *Huber-v.Mises* cylinder, whose center line coincides with the hydrostatic axis, see Figure 10. Due to the fact that here hydrostatic stresses (in contrast to the modified approach of *Raghava*, Eq. V13) have no influence on the yield behavior, this plasticity model is only suitable for a few materials, such as steel. This is also evident from the symmetrical yield surface in the plane stress state ($\sigma_3=0$).

3D view *Stress state with constant σ_3*
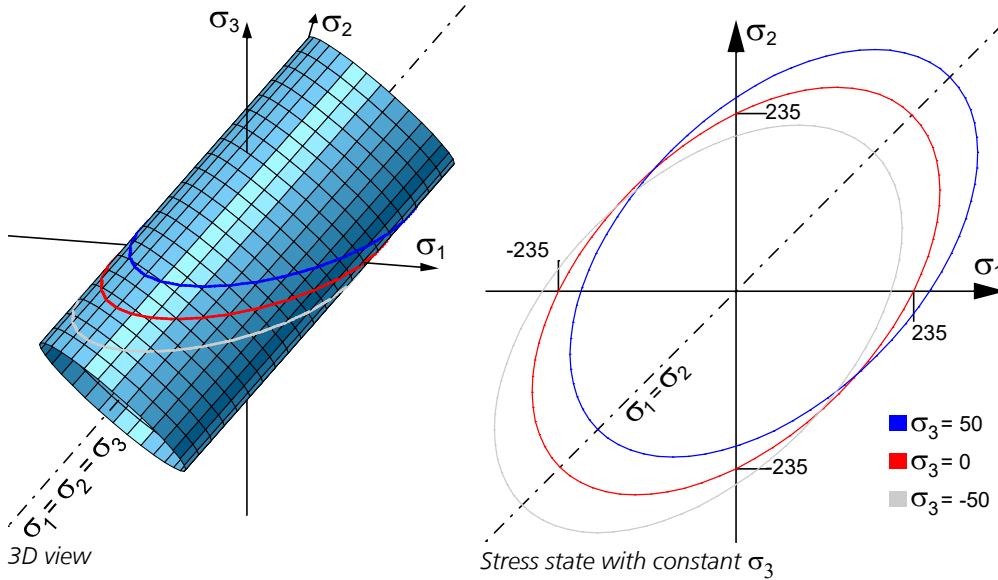
Figure 10:   Yield surface according to Huber-v.Mises in the principal stress space, f_c = 235 MPa, f_t = 235 MPa

Rankine

A plasticity criterion that can be used in addition to the two previously mentioned for solid elements of the material type *Frei* is based on the work of *Rankine* (1858). It is mainly suitable for brittle materials, since only one of the three principal stresses must exceed the elastic limit ($\sigma_{1,2,3} > f_{c,t}$) for plastic yield to occur. The remaining two principal stresses have no effect on material failure. The yield surface composed of two parts is shown in Figure 11.

3D view *Plane stress state*
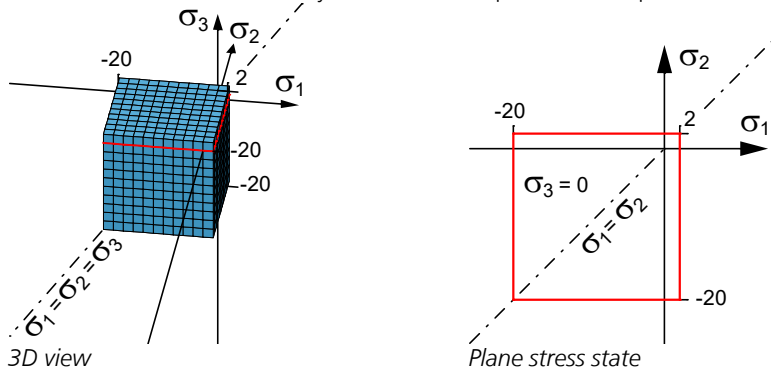
Figure 11:   Yield surface according to Rankine in the principal stress space, f_c = 20 MPa, f_t = 2 MPa

With the first invariant of the stress tensor I_1, the second deviatoric invariant J_2, the *Lode* angle Θ and the respective strengths (t: tension, c: compression), the following form of the yield criterion is obtained:

$$F_{t,c}(\sigma) = 2 \cdot \sqrt{3 \cdot J_2} \cdot \cos\Theta + I_1 - 3 \cdot f_{t,c} = 0 \tag{V15}$$

Mohr-Coulomb

A frequently used plasticity model for estimating the load-bearing behavior of soils (i.a. bearing capacity failure of foundation and embankment failure) was developed by *Coulomb* in the 18th century and generalized by *Mohr* towards the end of the 19th century: the *Mohr-Coulomb* model. Here, a linear relationship is assumed between the shear strength of a material and the normal stresses occurring in the shear joint, with the resistance that occurs during sliding within the shear joint being defined by the angle of friction

φ. With additional consideration of the cohesion *c*, i.e. the adhesive strength of individual soil particles, the following form of the yield condition is obtained:

$$F(\sigma) = \tau + \sigma \cdot \tan(\varphi) - c = 0,$$

With the use of *Mohr's* stress circle, the above equation can also be formulated as a function of the maximum and minimum principal stress:

$$F(\sigma) = (\sigma_{max} - \sigma_{min}) + (\sigma_{max} + \sigma_{min}) \cdot \sin(\varphi) - 2 \cdot c \cdot \cos(\varphi) = 0 \qquad \text{(V16)}$$

The *Mohr-Coulomb* yield surface is described by a total of six planar surfaces, which form an irregular six-sided pyramid in the three-dimensional stress space, see Figure 12. Its shape can also be clearly understood by the showb sections perpendicular to the hydrostatic axis (deviator plane). In addition, the influence of material parameters such as friction angle φ and cohesion *c* becomes obvious when comparing yield surfaces generated with both concrete (Figure 12, left) and soil (right) parameters.

3D view, sections parallel to deviatoric plane   3D view, sections parallel to deviatoric plane
$\varphi = 54.9°, c = 3.16$ MPa corresponds to $f_c = 20$ MPa, $f_t = 2$ MPa $\varphi = 30°, c = 1$ kPa

Figure 12: Yield surface according to Mohr-Coulomb in the principal stress space

In order to prevent an overestimation of the volume increase during plastic yielding (dilatancy), the general case of the non-associative yielding rule has been implemented in *InfoCAD*. Accordingly, in addition to the two previously known input values (φ and *c*), a further parameter must be specified in the dialog for the material properties, namely the dilatancy angle ($\psi \leq \varphi$). For the special case of an associated yield rule, the friction angle and dilatancy angle are identical ($\varphi = \psi$). Currently, a maximum friction angle of 60° can be entered in *InfoCAD*. A friction angle of zero results in the yield function according to *Tresca*.

Drucker-Prager

In contrast to *Rankine* and *Mohr-Coulomb*, the yield surface of the *Drucker-Prager* plasticity model (here: with adjustment to uniaxial strengths) has no edges. The smooth surface of the Drucker-Prager cone (see Figure 13) is an approximation of the Mohr-Coulomb criterion and is determined in the same way as for *Raghava* by the two invariants and the respective strengths for tension and compression:

$$F(\sigma) = \sqrt{J_2} + \alpha \cdot I_1 - \beta \cdot c = 0 \text{ , with: } \alpha = \frac{1}{\sqrt{3}} \cdot \frac{f_c - f_t}{f_c + f_t} \text{ , } \beta = \frac{2}{\sqrt{3}} \text{ and } c = \frac{f_c \cdot f_t}{f_c + f_t} \qquad \text{(V17)}$$

If the tensile and compressive strength are identical, the hydrostatic dependency is omitted here as well and this results to the *Huber-v.Mises* yield criterion again.

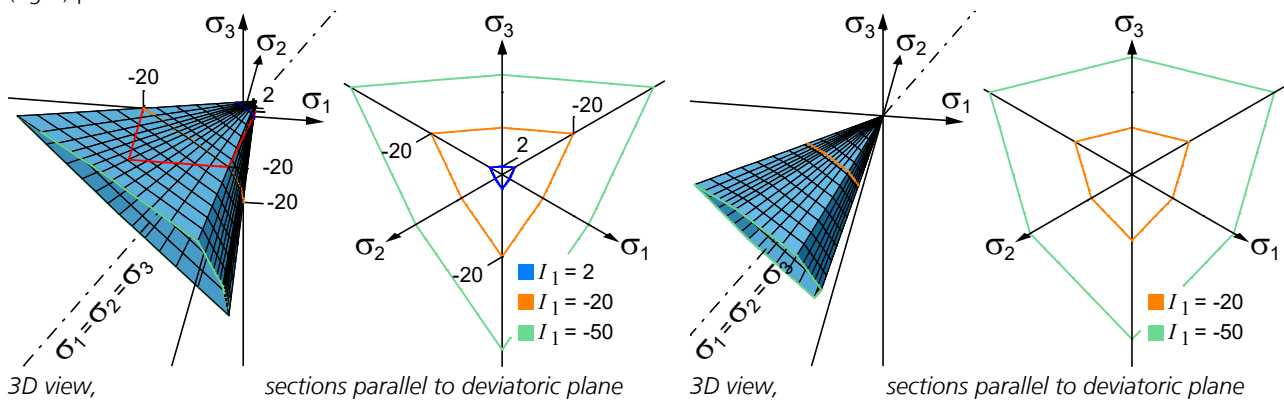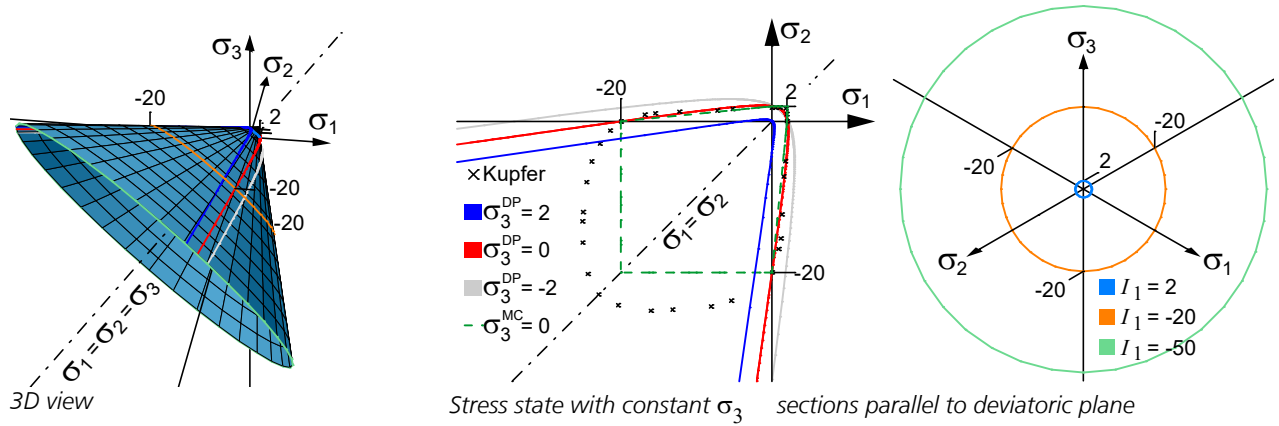*3D view*   *Stress state with constant* σ_3 *sections parallel to deviatoric plane*

Figure 13: Yield surface according to Drucker-Prager in the principal stress space, f_c = 20 MPa, f_t = 2 MPa

In addition, it is clear from Figure 13 that for the strengths used here, contrary to Mohr-Coulomb, no failure occurs in the compression-compression zone (plane stress state σ_3=0). For other values, however, this is quite possible. The following relationship must be considered: the smaller the difference between compressive and tensile strength, the smaller the angle between the yield surface and the hydrostatic axis.

Lubliner

While all previously described plasticity models can only inadequately represent the fracture criteria of concrete or its biaxial material behavior, the yield surface according to *Lubliner et al.* (1989) in the plane stress state (σ_3=0) agrees almost exactly with the failure surface experimentally determined by *Kupfer et al.* (1969), see Figure 14 (center).
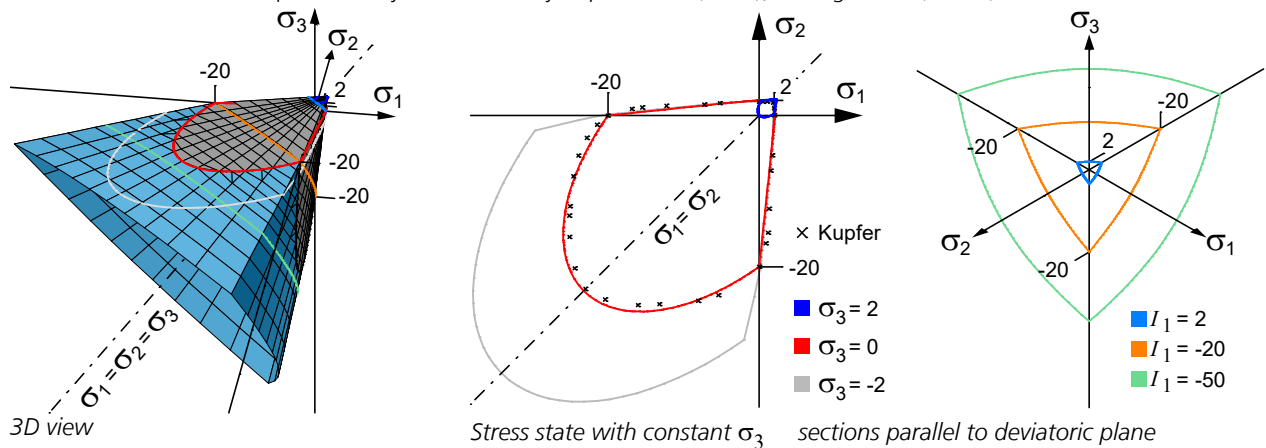

3D view   *Stress state with constant* σ_3 *sections parallel to deviatoric plane*

Figure 14: Yield surface according to Lubliner in the principal stress space, f_c = 20 MPa, f_t = 2 MPa, f_{cb} = 1,16·f_c

The *Lubliner* surface is composed of three components. This is clearly shown by the yield criterion, which contains maximum values of the positive <σ_{max}> and negative <-σ_{max}> stresses put in *Macaulay* brackets

$$F = \underbrace{\sqrt{3 \cdot J_2}}_{1} \underbrace{+ \alpha \cdot I_1}_{2} \underbrace{+ \beta \cdot \langle \sigma_{max} \rangle}_{3} \underbrace{- \gamma \cdot \langle -\sigma_{max} \rangle}_{4} \underbrace{- (1-\alpha) \cdot f_c}_{5} = 0 , \tag{V18}$$

where

$$\alpha = \frac{(f_{cb}/f_c) - 1}{2 \cdot (f_{cb}/f_c) - 1} , \quad \beta = (1-\alpha) \cdot \frac{f_c}{f_t} - (1+\alpha) , \quad \gamma = \frac{3 \cdot (1 - \varphi_c)}{2 \cdot \varphi_c - 1} \quad \text{and} \quad \varphi_c = \frac{2}{3} . \tag{V19}$$

Depending on the stress state, a reduced form of equation V18 results. As already mentioned, three cases are possible:
1) Tensile stresses present -> fourth term of the right-hand side is omitted.
2) Biaxial compression -> third and fourth term omitted.
3) Triaxial compression -> third term omitted.
Due to the congruent areas at biaxial and triaxial compression, the governing yield surface can finally be described by two terms. In Figure 14 (left), these are shown in color for differentiation: gray area -> tensile stresses present, blue area -> triaxial compression. In addition to the tensile and compressive strength, the equibiaxial compressive strength factor (factor = f_{cb}/f_c) can also be adjusted in the material properties dialog for the Lubliner model. The default value (for concrete) is

suggested to be 1.16 times the uniaxial compressive strength (f_c):

$$f_{cb} = 1.16 \cdot f_c .$$ (V20)

The shape of the yield surface is also influenced by the ratio of tensile and compressive meridians at triaxial compression, which is described by the parameter φ_c (see Eq. V19). Values between 0.5 and 1 are theoretically possible ($0.5 < \varphi_c \leq 1$). Displayed in deviator plane, these two limits result in a triangle ($\varphi_c = 0.5$ *Rankine*) or a circle ($\varphi_c = 1$ *Drucker-Prager*). Here the value was set to $\varphi_c = 2/3$ according to the recommendation in *Lubliner et al.* (1989) and *Richart et al.* (1928).

In the same way as with *Mohr-Coulomb*, a non-associative yield rule rather than an associative yield rule is used to ensure sufficient dilatancy, i.e. volume increase during plastic yielding. Plastic potential and yield condition are now no longer identical. The plastic strain increments are determined by deriving a potential function

$$\Delta \varepsilon^{pl} = \Delta \lambda \frac{\partial G(\sigma)}{\partial \sigma}$$ (V21)

and, as a result, are no longer perpendicular to the yield surface. Following the *Lubliner* yield condition (V18), which is composed of different *Drucker-Prager* surfaces, a *Drucker-Prager* type function is also used as the plastic potential. The potential function is as follows:

$$G(\sigma) = \sqrt{2 \cdot J_2 + \left(\tan(\psi) \cdot f_t \cdot \xi\right)^2} + \frac{\tan(\psi)}{3} \cdot I_1$$ (V22)

In addition to the two stress invariants I_1 and J_2, the input variables are the uniaxial tensile strength f_t, the dimensionless parameter ξ, and the dilatancy angle ψ. Both the parameter ξ and the dilatancy angle ψ significantly determine the shape of the potential function, see Fig.15 ($\xi = 0$: linear, $\xi > 0$: hyperbolic).
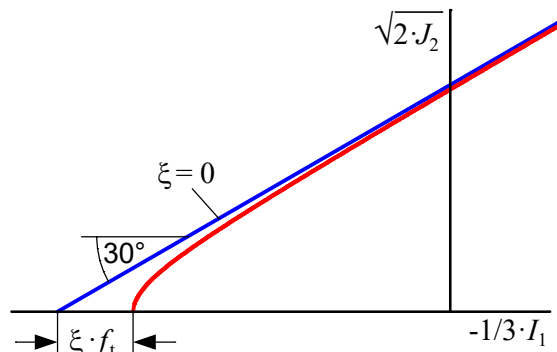
Figure 15: Linear and hyperbolic potential function

While in almost all scientific publications (thus also in *InfoCAD*) the parameter ξ is consistently set to 0.1, very different values for ψ are proposed for describing the dilatancy behavior of concrete. Good results have been obtained with dilatancy angles from $\psi = 11.3°$ to $\psi = 56°$, see *Poliotti & Bairan* (2019).
Considering this range of values, a dilatancy angle of $\psi = 30°$ is chosen in *InfoCAD*.

Note: From a non-associative yield rule follows an asymmetric elasto-plastic tangent and thus an asymmetric stiffness matrix. For an efficient solution of the equation system, the elasto-plastic tangent is symmetrized in *InfoCAD*, see *Pande et al.* (1990). However, to ensure numerical stability, it is recommended to perform the calculation with a constant stiffness.

Linear Hardening

In contrast to the material type *Stahl* or a standardized concrete type, the material type *Frei* offers the possibility to consider a linear hardening. Its degree is defined by the hardening modulus H, which is to be specified in the dialog for the material properties. When entering the modulus, the plastic material behavior is also directly defined. While a linear hardening can be realized by a positive hardening modulus, the modulus is set to zero for modeling an ideal plastic behavior.
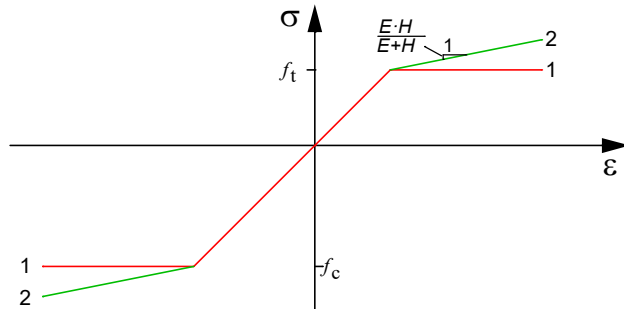

Figure 16:   *Uniaxial stress-strain diagram. Material behavior:*
1) ideally plastic, 2) with linear hardening for Rankine

Using the *Rankine* yield condition as an example, it is shown below how the hardening is to be included in the respective equations. An isotropic hardening is characterized by an expanding yield surface in the stress space; in contrast to kinematic hardening, the orientation does not change. To realize this expansion, a term $q(\kappa)$ dependent on the internal (hardening) variable κ is added to the initial yield stress $f_{t,c}$ (cf. Eq. V15):

$$F_{t,c}(\sigma, \kappa) = 2 \cdot \sqrt{3 \cdot J_2} \cdot \cos\Theta + I_1 - 3 \cdot \left(f_{t,c} + q(\kappa) \right) = 0 \tag{V23}$$

In *InfoCAD*, this term is described by the following linear function: $q(\kappa) = H \cdot \kappa$. A detailed derivation and explanation of the numerical implementation is omitted here. Instead, we refer to the publications by *Chen & Han* (1988) and *Simo & Hughes* (1998).

Combined Model (Plasticity-Damage)

The constitutive relations of the elasto-plastic damage model are obtained by combining Eq. V1 and Eq. V12 as follows:

$$\sigma = (1 - D)\, C : (\varepsilon - \varepsilon^{pl}) \tag{V24}$$

A coupling of stresses σ and effective stresses $\overline{\sigma}$ is carried out here by means of the scalar damage variable D, which reduces the stiffness isotropically in analogy to the procedure for the pure damage models:

$$\sigma = (1 - D) \cdot \overline{\sigma} \tag{V25}$$

To determine the plastic strains ε^{pl}, the yield condition according to *Lubliner et al.* (V18) is first evaluated taking into account the effective stresses:

$$F(\overline{\sigma}, \widetilde{\varepsilon}^{pl}) = \sqrt{3 \cdot J_2} + \alpha \cdot I_1 + \beta(\widetilde{\varepsilon}^{pl}) \cdot \langle \overline{\sigma}_{max} \rangle - \gamma \cdot \langle -\overline{\sigma}_{max} \rangle - (1 - \alpha) \cdot \overline{\sigma}_c(\varepsilon_c^{pl}) \leq 0 \tag{V26}$$

Input variables are, in addition to the effective stresses, two internal variables (*Lee & Fenves,* 1998), the tensile (ε_t^{pl}) and compression (ε_c^{pl}) plastic strains:

$$\widetilde{\varepsilon}^{pl} = [\varepsilon_t^{pl} \quad \varepsilon_c^{pl}]^T \tag{V27}$$

Their evolutions, which describe the hardening and softening of the material, can be calculated as a function of the eigenvalues of the plastic strain tensor and the triaxial factor $r(\overline{\sigma})$ (V5) as follows:

$$\dot{\varepsilon}^{pl} = \begin{bmatrix} \dot{\varepsilon}_t^{pl} \\ \dot{\varepsilon}_c^{pl} \end{bmatrix} = \begin{bmatrix} r(\overline{\sigma}) & 0 & 0 \\ 0 & 0 & 1 - r(\overline{\sigma}) \end{bmatrix} \begin{bmatrix} \dot{\varepsilon}_1^{pl} \\ \dot{\varepsilon}_2^{pl} \\ \dot{\varepsilon}_3^{pl} \end{bmatrix} , \text{ mit: } \dot{\varepsilon}_1^{pl} \geq \dot{\varepsilon}_2^{pl} \geq \dot{\varepsilon}_3^{pl} \tag{V28}$$

The factor $\beta(\widetilde{\varepsilon}^{pl})$ in Eq. V26 is here, in the case of the combined model (plasticity and damage), not constant (cf. Eq. V19), but dependent on the two internal variables:

$$\beta(\widetilde{\epsilon}^{\,pl}) = (1-\alpha) \cdot \frac{\sigma_c(\epsilon_c^{\,pl})}{\sigma_t(\epsilon_t^{\,pl})} - (1+\alpha) \tag{V29}$$

After iterative calculation of the plastic multiplier $\Delta\lambda$ with the return mapping method, the scalar damage parameter D is determined as a function of the internal variable $\widetilde{\epsilon}^{\,pl}$. Due to the separation of tensile and compressive plastic strains, the same procedure is used for the damage parameter. With the parameter for tension

$$d_t = 1 - \frac{\sigma_t \cdot E_0^{\,-1}}{\epsilon_t^{\,pl} \cdot (1/b_t - 1) + \sigma_t \cdot E_0^{\,-1}} \tag{V30}$$

and compression

$$d_c = 1 - \frac{\sigma_c \cdot E_0^{\,-1}}{\epsilon_c^{\,pl} \cdot (1/b_c - 1) + \sigma_c \cdot E_0^{\,-1}} \tag{V31}$$

the isotropic damage for the three-dimensional stress state is finally determined (V23):

$$D = 1 - (1 - s_c \cdot d_t) \cdot (1 - s_t \cdot d_c) \tag{V32}$$

Since it is currently not possible to simulate load changes (hysteresis) in *InfoCAD*, opening or closing of cracks is not taken into account when calculating the damage parameter ($s_c = s_t = 1$).
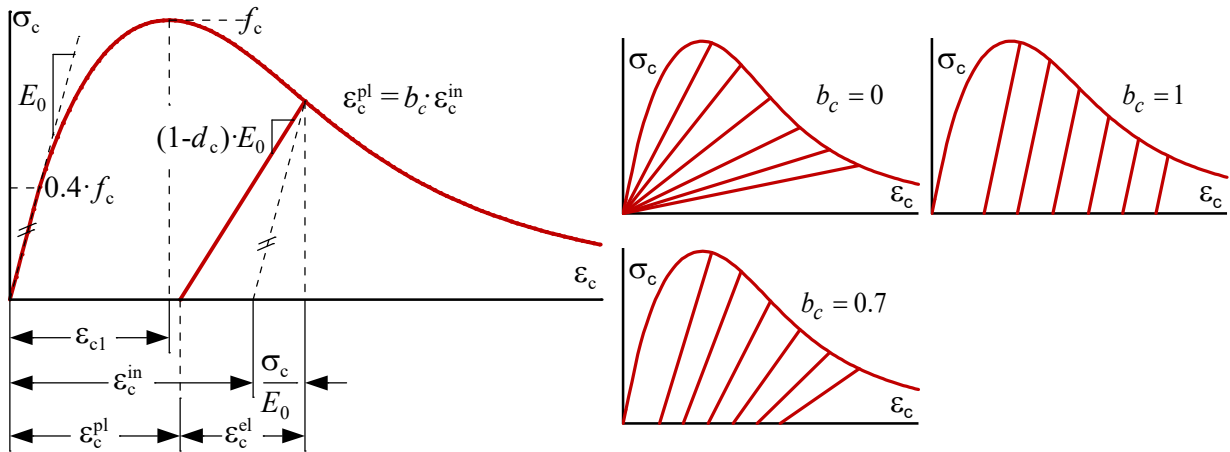

Figure 17:   *Uniaxial compressive stresses*

For a realistic description of the material behavior, uniaxial stress-strain relationships are used, which are based on a decomposition of the strains into elastic, plastic or inelastic components. Separated for compression and tension (elongation), the relationships are as follows (Figs. 17 and 18):

$$\epsilon_c = \epsilon_c^{\,el} + \epsilon_c^{\,pl} = \epsilon_c^{\,in} + \sigma_c / E_0 \text{, with: } \epsilon_c^{\,pl} = b_c \cdot \epsilon_c^{\,in} \tag{V33}$$

$$\epsilon_t = \epsilon_t^{\,el} + \epsilon_t^{\,pl} = \epsilon_t^{\,in} + \sigma_t / E_0 \text{, with: } \epsilon_t^{\,pl} = b_t \cdot \epsilon_t^{\,in} \tag{V34}$$

Here, the factor b_c or b_t determines the ratio of plastic and inelastic strains and thus also the inclination of any unloading paths. While no damage of the material occurs with a factor of $b_{c,t} = 1$ ($D = 0$) and loading and unloading paths have the same inclination, no plastic strains remain after unloading with a factor of $b_{c,t} = 0$. The influence of the parameter can be clearly illustrated by means of both limiting cases (see also Figs. 17 and 18). However, these two cases do not represent a realistic material behavior of concrete during loading and unloading processes. Experimental results often show that the ratio of plastic to inelastic strains takes the value $b_c = 0.7$ (compression) and $b_t = 0.1$ (tension). Consequently, these two values are also used in *InfoCAD*.
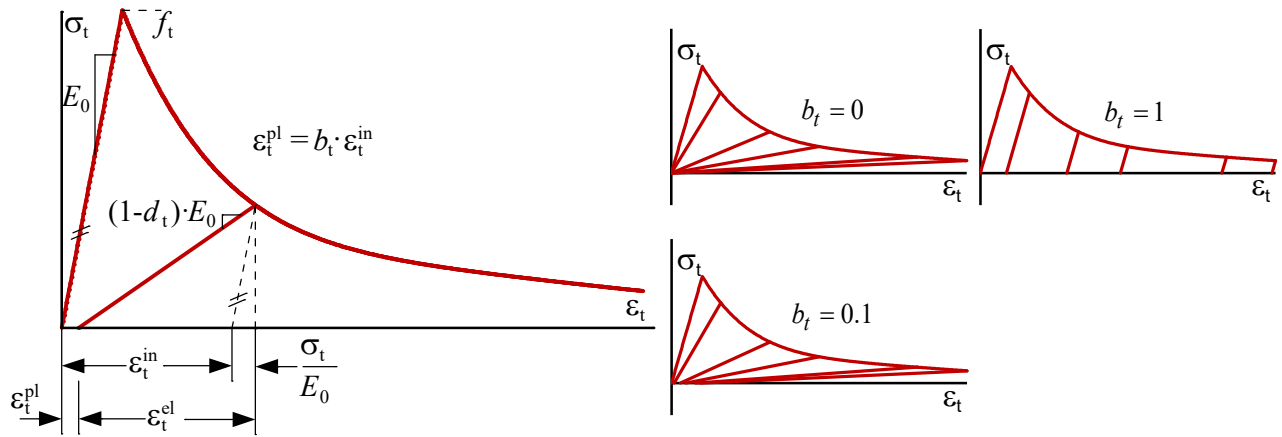
Figure 18:   Uniaxial tensile stresses

The uniaxial stress-strain relations implemented here are defined separately for certain areas. First, the functions for a pure compressive stress state are explained. The first of a total of three sections describes the linear elastic material behavior at the start of loading:

$$\sigma_c(\varepsilon_c) = E_0 \cdot \varepsilon_c \quad \text{for} \quad \sigma_c(\varepsilon_c) \leq 0.4 \cdot f_c \tag{V35}$$

Following the curves according to the standard, 0.4 times the compressive strength is taken as the initial yield stress here. After reaching this limit value, the tangential stiffness (initial: E_0) is successively reduced until a horizontal curve is obtained at $\sigma_c(\varepsilon_c) = f_c$. For this second section, the following analytical function from *CEB-FIP Model Code 1990* is used due to its good agreement with experimental results:

$$\sigma_c(\varepsilon_c) = \frac{E_{ci} \cdot \frac{\varepsilon_c}{f_c} - \left(\frac{\varepsilon_c}{\varepsilon_{c1}}\right)^2}{1 + \left(E_{ci} \cdot \frac{\varepsilon_{c1}}{f_c} - 2\right) \cdot \frac{\varepsilon_c}{\varepsilon_{c1}}} \cdot f_c \quad \text{for } 0.4 \cdot f_c < \sigma_c(\varepsilon_c) \leq f_c \tag{V36}$$

To ensure a continuous transition between the first two sections of the stress-strain relation, the following secant modulus is used to evaluate Eq. V36 instead of the elastic modulus of the undamaged material ($E_{ci} = E_0$):

$$E_{ci} = \frac{2}{3 \cdot E_c} \cdot \left(\frac{f_c}{\varepsilon_{c1}}\right)^2 - \frac{4 \cdot f_c}{3 \cdot \varepsilon_{c1}} + \frac{5}{3} \cdot E_0 \tag{V37}$$

The limit compression ε_{c1} is to be specified a-priori in the same way as the compressive strength in the dialog of the material properties. For a realistic representation of the post-cracking behavior of concrete and minimization of the mesh dependency, the approach of *Krätzig & Pölling* (2004) is used here. This third and final section of the stress-strain relationship under monotonic compressive loading is described by the following function:

$$\sigma_c(\varepsilon_c) = \left(\frac{2 + \gamma_c \cdot f_c \cdot \varepsilon_{c1}}{2 \cdot f_c} - \gamma_c \cdot \varepsilon_c + \frac{\gamma_c \cdot (\varepsilon_c)^2}{2 \cdot \varepsilon_{c1}}\right)^{-1} \quad \text{for } \sigma_c(\varepsilon_c) > f_c \tag{V38}$$

with

$$\gamma_c = \frac{\pi^2 \cdot f_c \cdot \varepsilon_{c1}}{2 \cdot \left(g_c - \frac{f_c}{2} \cdot \left(\varepsilon_{c1} \cdot (1 - b_c) + \frac{b_c \cdot f_c}{E_0}\right)\right)^2} > 0 \tag{V39}$$

and the element and volume based compressive fracture energy: $g_c = G_c / l_c$. In order to nearly eliminate the mesh dependence during softening, the compressive fracture energy G_c is coupled to the element size (volume V_e). Simplified for solid elements, the characteristic length l_c is: $l_c = V_e^{1/3}$ (*Oliver*, 1989). Experimental tests on specimens have also shown that for normal concrete the amount of compressive fracture energy G_c is in the range between 10 and 25 kN/m (*Vonk*, 1992). In *InfoCAD*, however, values between 5 and 500 kN/m are permitted.

The influence of the energy on the free parameter γ_c, which defines the area under the stress-strain curve, is evident from Eq. V39. Due to the condition $\gamma_c > 0$, a negative denominator must also be excluded. Consequently, to avoid a snap-back behavior, the characteristic length should not exceed the following value (*Krätzig & Pölling*, 2004):

$$l_c \leq G_c / (f_c \cdot (\varepsilon_{c1} \cdot (1 - b_c) + b_c \cdot f_c / E_c)) \tag{V40}$$

For a monotonic compressive loading, the stress-strain diagram consisting of three parts is shown in Figure 17 (left) and Figure 19. Figure 19 also clearly shows the good agreement between numerical (*InfoCAD*) and experimental (*Sinha et al.*, 1964) results.

Except for the compressive fracture energy (here: G_c = 26 kN/m), all parameters for the comparative calculation were taken from the publication by *Krätzig & Pölling* (2004).
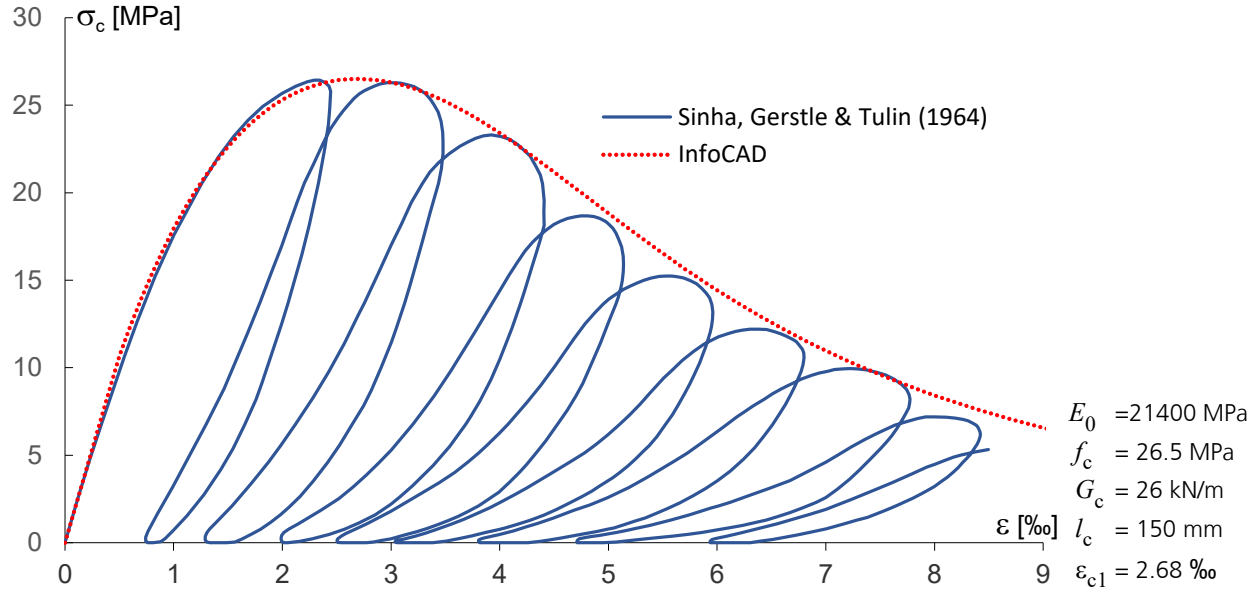

Figure 19: Uniaxial stress-strain diagram (compression): Comparison of experimental (Sinha, Gerstle & Tulin, 1964) and numerical (InfoCAD) results

After describing the stress-strain relationship for compressive loading implemented in *InfoCAD*, the functions for a tensile load are now specified below. Only two sections need to be defined for this purpose. The first section describes the linear elastic material behavior up to the tensile stress f_t

$$\sigma_t(\varepsilon_t) = E_0 \cdot \varepsilon_t \quad \text{for } \sigma_t(\varepsilon_t) \leq f_t \tag{V41}$$

and the second section describes the softening material behavior (decreasing branch). The function, which realistically represents the softening of concrete under monotonic tensile loading, is based on the scientific work of *Cornelissen et al.* (1986) and *Hordjik* (1992). The following stress-crack opening relationship was empirically determined during experiments:

$$\sigma_t(w) = f_t \cdot \left(\left[1 + \left(\frac{c_1 \cdot w}{w_c} \right)^3 \right] \exp\left(-c_2 \frac{w}{w_c} \right) - \frac{w}{w_c} \cdot (1 + c_1)^3 \cdot \exp(-c_2) \right), \quad \text{with: } c_1 = 3 \text{ and } c_2 = 6.93 \tag{V42}$$

Using the inelastic strains ε_t^{in} (V34), the stress-crack opening relation is finally transformed into a stress-strain relation:

$$\sigma_t(\varepsilon_t) = \sigma_t(w = \varepsilon_t^{in} \cdot l_c) \quad \text{for } \sigma_t(\varepsilon_t) > f_t \tag{V43}$$

The volume-specific fracture energy $g_f = G_f / l_c$ and thus the dependency of the decreasing branch on the element size (*Bažant & Oh*, 1983) is already taken into account in Eq. V43:

$$G_f = \int_0^{w_c} \sigma_t(w)\, dw = l_c \cdot \int_0^{w_c / l_c} \sigma_t(\varepsilon_t)\, d\varepsilon_t \tag{V44}$$

After solving the integral over the critical crack width w_c, it follows:

$$G_f = 0.195 \cdot w_c \cdot f_t \tag{V45}$$

In addition to the tensile strength f_t, the fracture energy G_f or the critical crack width w_c must also be specified as a material parameter. In *InfoCAD*, the fracture energy was selected as the input variable (see *Material Properties* dialog). However, the above equation can be used to directly determine the fracture energy if the limit crack width is known.

Figure 20 shows the stress-strain relationship for monotonic tensile loading. Here it becomes clear that, using the function generated by *Cornelissen et al.* (1986) and *Hordjik* (1992), negative stresses are to be expected as soon as the crack width w corresponding to the strain exceeds the critical crack width w_c: $w = \varepsilon_t^{in} \cdot l_c > w_c$ (see V42). Since negative stresses are not permissible, an adjustment must be made for this strain range in the numerical implementation.
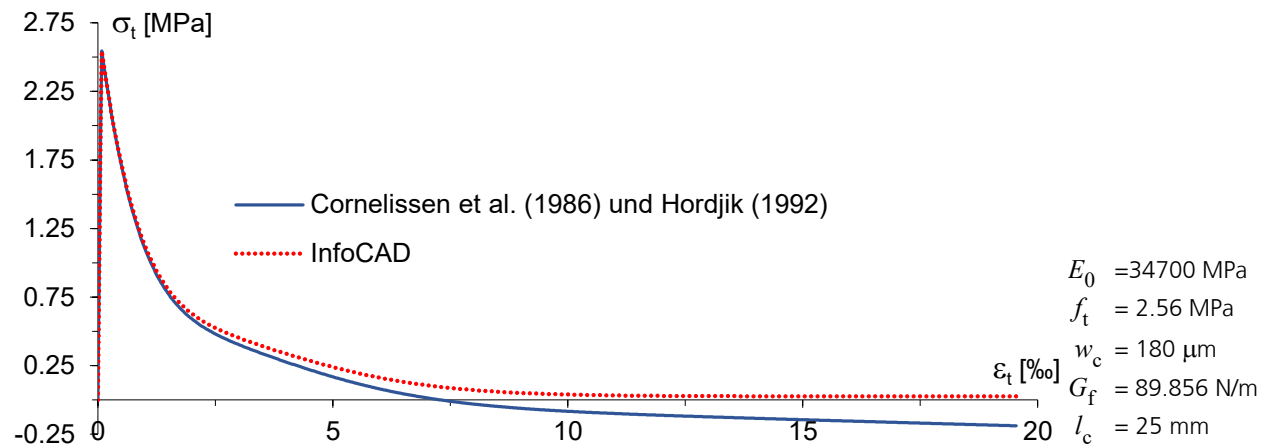
Figure 20:   *Uniaxial stress-strain diagram*

For example, in order to exclude a kink in the stress-strain relationship, which occurs when the critical crack width is exceeded if the stress in this area were set to zero $\langle \sigma_t(\varepsilon_t)\rangle$, the stress-crack opening relationship (V42) is slightly modified for the calculation with *InfoCAD*. On the one hand, the third term is neglected, thus excluding negative stresses, and on the other hand, a factor for the residual tensile strength r is introduced so that stresses never become zero even at infinitely large strains, but asymptotically approach the value $\sigma_t(\varepsilon_t) = r \cdot f_t$ (here $r = 0.02$). The adjusted stress-crack opening relation is then:

$$\sigma_t(w) = f_t \cdot \left(1 - (1-r) + \left[1 + \left(\frac{c_1 \cdot w}{w_c} \right)^3 \right] \cdot (1-r) \cdot \exp\left(-c_2 \frac{w}{w_c} \right) \right) \tag{V46}$$

In addition to the original form, the modified stress-strain relationship for monotonic tensile stresses is also shown in Figure 20. In addition to the different functional curves after reaching the critical crack width, it becomes clear that the deviation of both tensile stresses before reaching the critical crack width is negligible.

In the same way as before for compressive stress, the characteristic length l_c should not exceed a certain value to avoid *snap-back* behavior. The limit is defined as follows [*Irwin* (1958), *Hillerborg et al.* (1976), *Bažant & Oh* (1983)]:

$$l_c < G_f \cdot E_c / f_t^2$$

To demonstrate the capability of the stress-strain relationship implemented in *InfoCAD*, numerical and experimental results are also compared here. Figure 21 shows the good agreement.
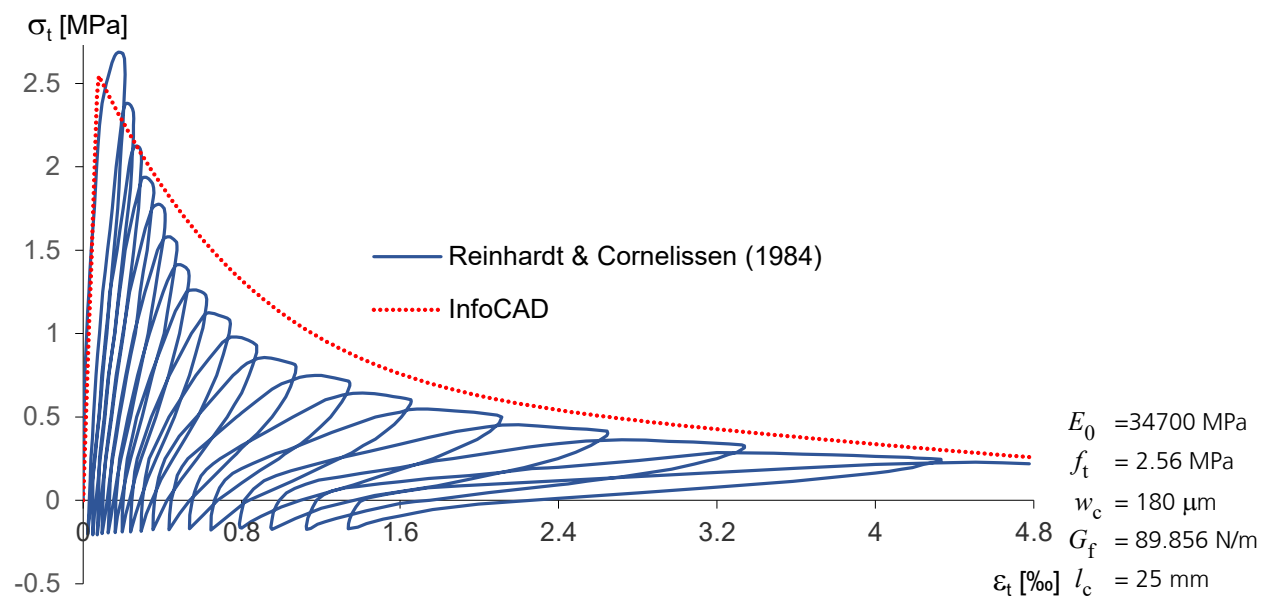

Figure 21:   *Uniaxial stress-strain diagram (tension): Comparison of experimental (Reinhardt & Cornelissen, 1984) and numerical (InfoCAD) results*

Prestressed Structures

Prestressing is often considered only as an external load. Therefore, no stress redistributions between concrete and prestressing steel can be taken into account. But the consideration of this redistributions is also possible. For this purpose, the tendons are included in the element stiffness matrices during the calculation. This method is implemented for all element types. The internal forces (normal forces, bending moments, lateral forces) given by the program always correspond to the concrete section with its reinforcing steel layers. When analyzing composite elements, these alone are not in equilibrium with the external forces since the tendon group forces must be applied while taking into account their spatial orientation. Because the program assumes that a tendon runs straight between the entry and exit points of an element, an adequate FE mesh is especially important for beam elements. Area and solid models, on the other hand, generally exhibit a sufficiently fine discretization.

The stress-strain curves of prestressing steel in the serviceability limit state have a rising branch with E_p and a horizontal upper branch at $f_{p0,1k}$ or β_s. In the ultimate limit state the upper branch is at f_{pd}. Depending on the concrete, the following strengths are assumed for f_{pd}.

- Concrete *DIN 1045:1988* $f_{pd} = \beta_s$

- Concrete *DIN EN 1992-1-1, DIN 1045-1* $f_{pd} = 1{,}1 \cdot f_{p0,1k}/\gamma_R$ mit $\gamma_R = 1.3$

- Concrete *EN 1992-1-1, ÖNORM B 4700, SIA 262* $f_{pd} = f_{p0,1k}/\gamma_s$ mit $\gamma_s = 1.15$

Notes on Convergence Behavior

The implemented analysis methods (Newton method, arc length method) with tangential stiffness matrix result in a stable convergence behavior given a consistent relationship between the stress-strain relation and its derivative. As previously mentioned, this is especially true of bilinear materials. Reinforced concrete, however, typically displays a poor convergence due to its more complex material properties. This is caused by crack formation, not continuously differentiable stress-strain relationships, two-component materials, etc.

Especially for checks of the serviceability and determination of the tensile stiffness with softening, markedly worse convergence can result due to the negative tangential stiffness in the softening area. If this results in a singular global stiffness matrix, it is possible to assume a bilinear function in the tensile section or to perform a calculation without tensile strength.

Material properties

In principle, only area, solid, polygon, database cross-sections and structural steel sections can be subjected to a nonlinear analysis. For all other cross-section types and for the material types *Beton* and *Timber*, linear material behavior is always used as a basis.

In the dialog described below for solid cross-sections with the material type *Frei*, non-linear material properties are specified. The material properties not described here, e.g. modulus of elasticity, are described in the general part of the manual.
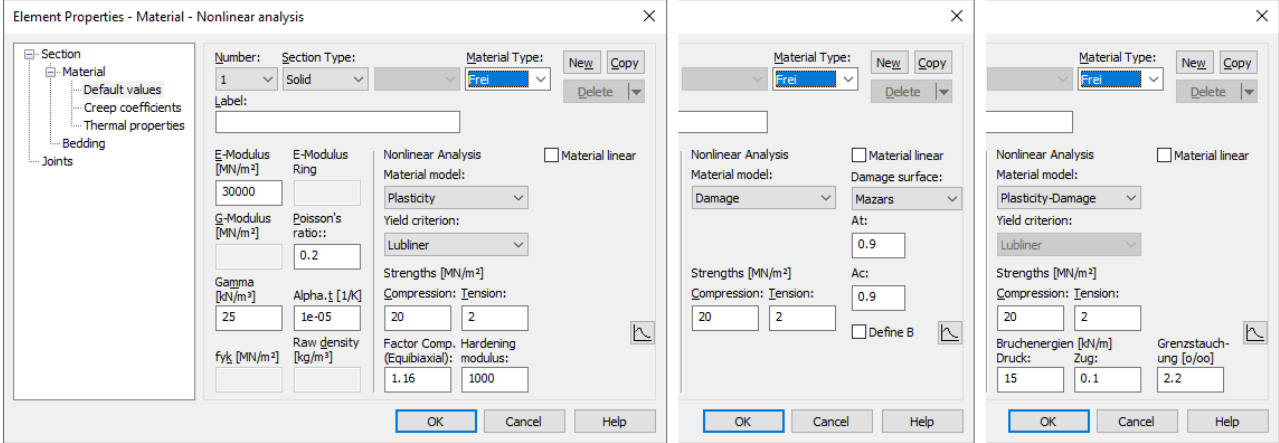
Material model

| Plasticity | Damage | Plasticity-Damage |

Yield criterion

- *Drucker-Prager*
- *Huber- von Mises*
- *Lubliner*
- *Mohr-Coulomb*
- *Raghava*
- *Rankine*

Damage surface

- *De Vree:* Damage model according to *De Vree* with the parameters A and B.
- *Mazars:* Damage model according to *Mazars* with the parameters A_t, B_t, A_c and B_c.

Strengths [MN/m²]

Compression: Yield strength under compressive stresses f_c (positive value)

Tension: Yield strength under tensile stresses f_t (positive value)

Material parameters for Mohr-Coulomb

Friction angle [°]: Resistance that occurs when sliding in a shear joint

Dilatancy angle [°]: Affects the change in volume during plastic deformation

Cohesion [MPa]: Adhesive strength or internal cohesion of individual particles (e.g. in soil or concrete).

More material parameters

Factor comp. (equibiaxial): The standard case for concrete f_{cb} / f_c = **1.16** is suggested, which is used for the yield condition according to *Lubliner*. (positive value).

Hardening modulus: Value describing hardening at strains above tensile and compressive strength.

Fracture energy compression / tension [kN/m]: Specific fracture energies for the material model *plasticity-damage*.

Ultimate compressive strain [‰]: Strain ε_{c1} under the maximum stress f_c for the material model *plasticity-damage*.

The uniaxial stress-strain relation can be visualized via the button ⌐ and adjusted if necessary. For the combined model (plasticity-damage), only the characteristic lengths has to be specified for the visualization. In the calculation, this is determined internally in dependence of the element volume (l_c or g_c in Eq. V38 and g_f in Eq. V42).

Material linear

This switch causes a linear-elastic material behavior for this cross-section in the nonlinear system analysis.

Analysis Settings

The following settings are made on the *Ultimate Limit state* and the *Serviceability* tabs in the *Settings* for the nonlinear analysis of the menu item *Analysis - Settings*.
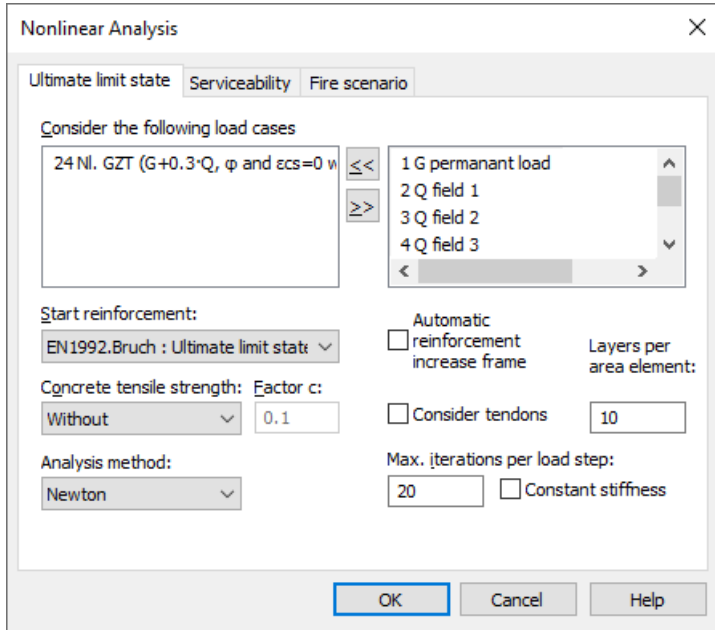
With the nonlinear system analysis, load cases are calculated under consideration of physical and geometrical nonlinearities, whereby the latter only becomes active if the second- or third order theory is activated in the load case. The load bearing capacity and serviceability check as well as the stability check for fire differ according to the load case that is to be checked, the material safety, the different stress-strain-curves and the consideration of the concrete tensile strength.

Consider the following load cases

The load cases from the left list box are calculated.

Start reinforcement

The nonlinear system analysis is carried out on reinforced concrete sections based on the reinforcement selected here. This results from a reinforced concrete design carried out in advance. The starting reinforcement *Null* corresponds to the base reinforcement of the reinforcing steel layers. When performing a check for fire scenarios, special conditions apply as explained in the *Structural Analysis for Fire Scenarios* chapter.

Automatic reinforcement increase frame

For the ultimate limit state check of pure frameworks a reinforcement increase is carried out for reinforced concrete sections to achieve the required load-bearing safety.

Concrete tensile strength; Factor c

This option defines the behavior in the tensile zone for the nonlinear internal forces calculation for all reinforced concrete sections. By default the ultimate limit state check is performed without considering the concrete tensile strength.

With softening (beams)   *With softening (area elements)*   *Bilinear*
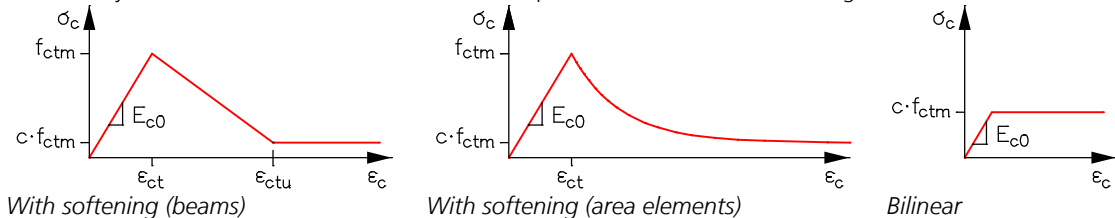
Layers per area element

Number of integration levels of an area element. Members subject to bending should be calculated with 10 layers. Structure mostly subject to normal forces can be adequately analyzed with 2 layers.

Consider tendons

The tendons are considered in the calculation of the element stiffness matrices.

Constant stiffness

The iteration is done with a constant stiffness matrix. If the switch is not set, then a tangential stiffness matrix is used.

Phi-c Reduction

Method for determining the stability of embankments (serviceability tab). Successive reduction of soil parameters (friction angle φ and cohesion c) until the failure condition (embankment failure) occurs. The *Phi-c Reduction* according to *Fellenius* is only activated in conjunction with the *Mohr-Coulomb* plasticity model. If the switch is set but no *Mohr-Coulomb* material is defined, the method is not used.

Analysis method

The following methods are available:

- **Newton, Newton time steps**

Max. iterations per load step:
    Maximum number of iteration steps, in order to reach convergence within one load step. If the error threshold is exceeded, the iteration is interrupted and an expectable reduced load level is determined on the basis of load. If it is not possible to fall below the error limit within the iteration steps per load step, the iteration is aborted and load-controlled the loadable load factor (≤ 1.0) or the load at an intermediate time is determined by interval nesting.

Time increment and Duration:
    The load-time function is defined in the database in the folder *Structure description > Instationary load-time function* and then assigned to loads. The time increment and the time duration must be adapted to the load time function. With regard to the special procedure for activating the *Phi-c Reduction*, please refer to the section ' Bearing capacity failure of foundation and embankment failure'.

- **Arc length**

Initial arc length:
    The initial arc length can either be entered manually (between 0.001 and 100) or calculated automatically depending on the system stiffness and load. While the arc length does not exceed the maximum value of 100 in the numerical calculation, significantly smaller arc lengths than 0.001 can occur. If the arc length is reduced to less than 1e-12 (1e-5 for Solids with Material type *Frei*), the calculation will be aborted. The input value is at the same time the maximum value, if a checkmark is set at "Up limited".

Iterations per arc length:
    Due to the influence of the iteration number on the arc length during the calculation, when the selected value is reached due to insufficient accuracy of the numerical solution, the number is doubled once. If divergent behavior occurs during the subsequent iterations, or if the error tolerance is not reached even after the increase, the arc length is halved.

Control:
    There are three ways to control the arc length method. This can be done via the number of increments to be calculated as well as via the first bifurcation point (inactive at constant stiffness) or, if a certain load level is to be achieved, via the load factor (correct to four decimal places).

Examples

## Flat Ceiling With Cantilever in State II

This example shows a ceiling slab that has already been analyzed in the *EN 1992-1-1 design manual*. For this slab, deformations in state II in the serviceability and the ultimate limit states are to be determined for comparison with the elastic calculation. serviceability limit state and ultimate limit state.

Loads

Load case 1,
G permanent loads [kN/m²]

Load case 2 to 9,
Q field 1 to 8 [kN/m²]
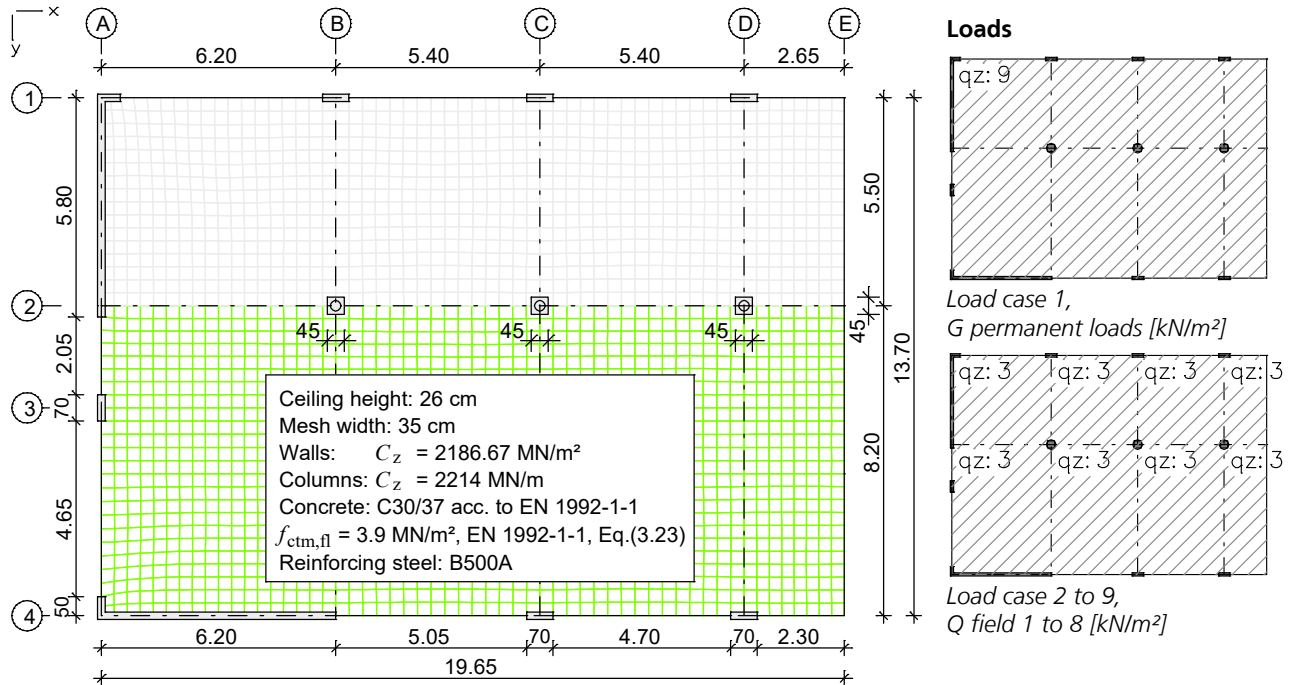
Element system and loads from
"Beispiele zur Bemessung nach Eurocode 2 – Band 2: Ingenieurbau"

Due to the normal forces to be expected in the slab, shell elements are to be used for the nonlinear structural analysis and horizontal support supports should preferably be free of restraint. Because the longitudinal reinforcement has an essential influence on the deformations within a nonlinear structural analysis, a realistic reinforcement arrangement is to be ensured. For this reason, a linear-elastic static calculation of load cases 1 to 9 with subsequent design according to EN 1992-1-1 using the basic reinforcement given below is carried out.

For the subsequent nonlinear system analysis, load cases 21 to 23 have already been entered with load groups.

In load cases 22, the nonlinear creeping of the concrete is additionally taken into account with the creep coefficient $\varphi = 2.5$ and the shrinkage of the concrete is assumed to be $\varepsilon_{cs} = -40 \cdot 10^{-5}$.
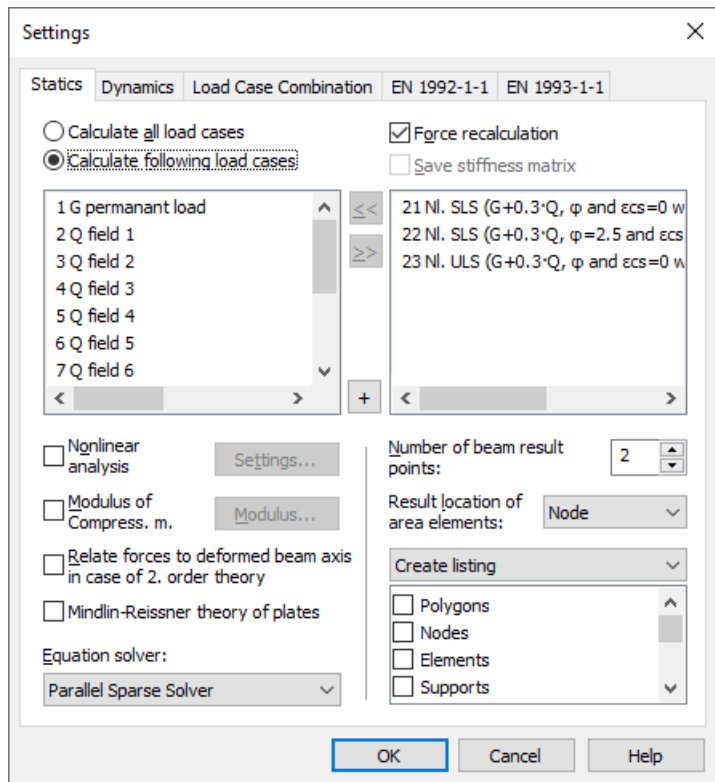
Reinforcement for area elements

No.	Lay.	Qual.	d1x [m]	d2x [m]	asx [cm²/m]	d1y [m]	d2y [m]	asy [cm²/m]	as fix	Roll-ing
1	1	500M	0.045		5.670	0.035		5.650		Warm
	2	500M		0.035	7.850		0.025	5.030		Warm
2	1	500M	0.045		5.670	0.035		5.650		Warm
	2	500M		0.035	7.850		0.025	11.340		Warm

as   Base reinforcement
d1   Distance from the upper edge
d2   Distance from the lower edge
   The z axis of the element system points to the lower edge

Bending reinforcement from design of the permanent and temporary situation

Only in the area around the columns and the corners does a reinforcement increase result in the upper reinforcement layers, which approximately corresponds to the additional reinforcement provided in the literature example.

Additional reinforcement $a_{sx.1}$ [cm²/m]   Additional reinforcement $a_{sy.1}$ [cm²/m]
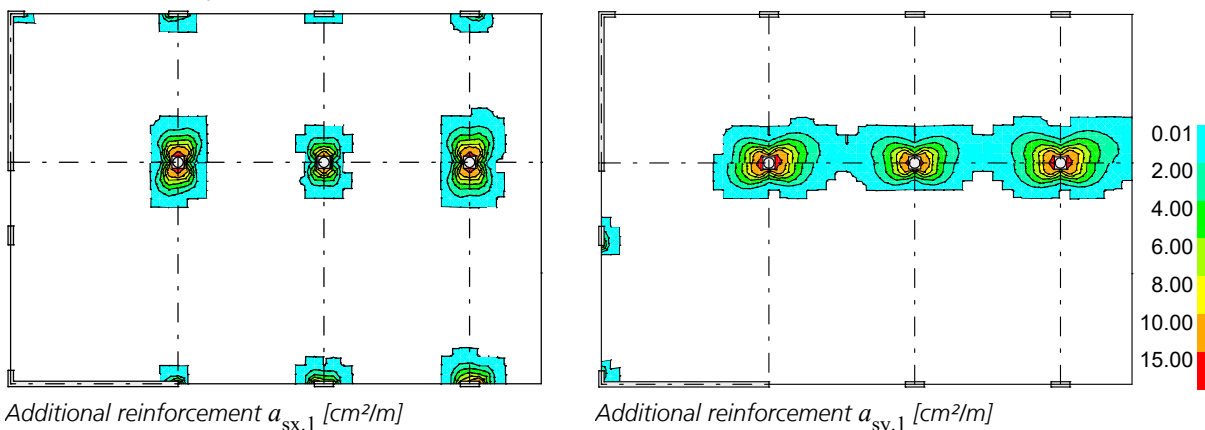
Analysis settings

After the elastic static calculation of load cases 1 to 9 and the subsequent design according to EN 1992-1-1, the nonlinear system analysis is selected in the static analysis settings and the following settings are made.
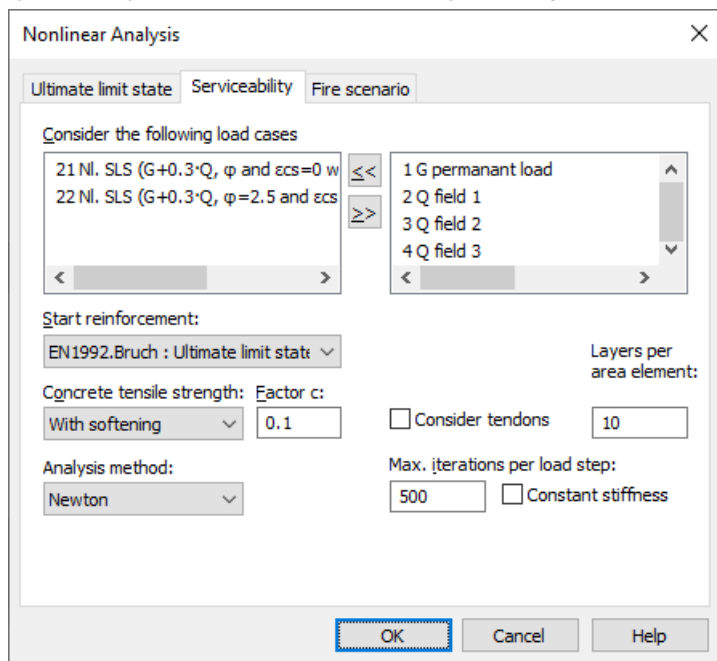

For the load cases (21 and 22) for serviceability, softening and a residual tensile strength of $c \cdot f_{ctm,fl}$ = 0.1·3.9 = 0.39 MN/m² are calculated in the tensile zone of the concrete.

Load case 23 for the ultimate limit state is calculated without considering the concrete tensile strength.

In order to increase the accuracy of the calculation, the error threshold is set to 0.1 % in the load groups. Therefore, the number of maximum iterations per load level is increased to 500.

Deformations

The different deformation results are compared below. For better comparison all non-linearly calculated load cases, including the one in the ULS, are calculated with the load G+0.3·Q. In all cases a load factor of 1.0 can be achieved.
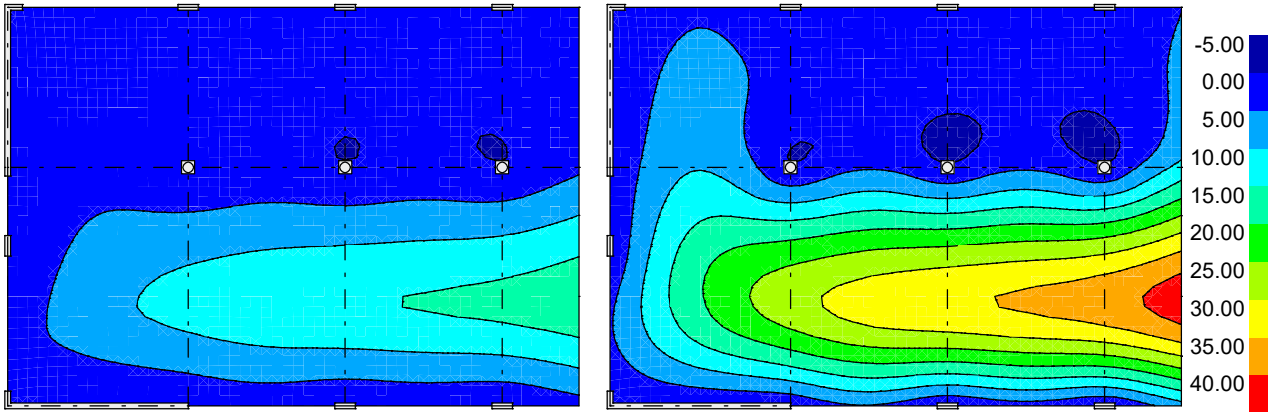

Load cases 21: Deformations u_z [mm]

Load cases 22: Deformations u_z [mm]

In the following, the maximum calculated deformations in state II are compared with the results determined in state I (see example for EN 1992-1-1):

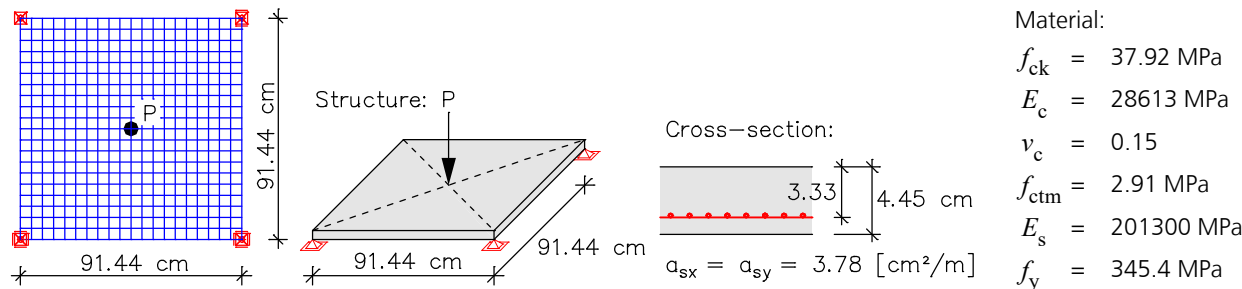| Load case		max u_z [mm]	
		Calculation	Literature
(11)	G+0.3·Q with elastic material behavior (state I)	10	10
(12)	Creeping (φ=2.5 by LC 11) with elastic material behavior (state I)	23	-
(13)	Total (load case 11 + load case 12) (state I)	33	-
21	Nl. SLS (G+0.3·Q, φ and ε_{cs}=0 with softening)	18	20
22	Nl. SLS (G+0.3·Q, φ=2.5 and ε_{cs}=-40·10^{-5} with softening)	43	40
23	Nl. ULS (G+0.3·Q, φ and ε_{cs}=0 without concrete tensile strength)	56	-

Concrete stresses
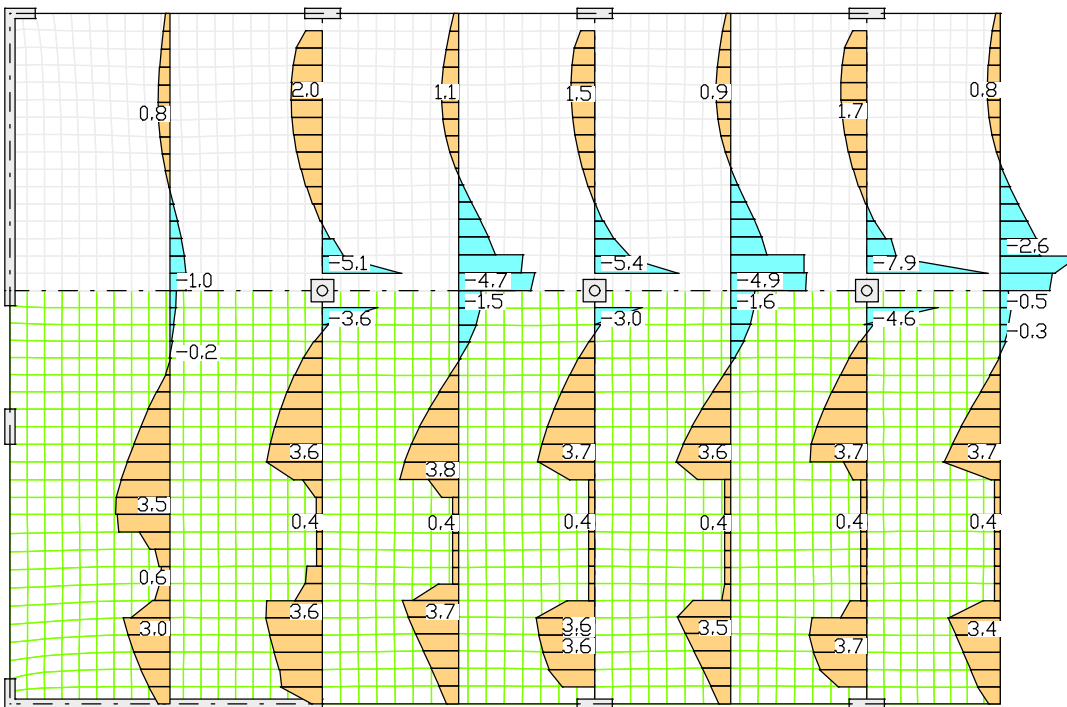
*Load case 22: Concrete stresses [MN/m²] in y-direction at the bottom*

Experiment of Fracture of a Reinforced Concrete Slab

The system described below was analyzed experimentally by Jofriet & McNeice in 1971 (taken from Krätzig & Meschke 2001). The goal is to demonstrate the plausibility of the achieved calculation results. For the crosscheck a system with 20x20 shell elements was used as illustrated below.

Material:

$$f_{ck} = 37.92 \text{ MPa}$$
$$E_c = 28613 \text{ MPa}$$
$$v_c = 0.15$$
$$f_{ctm} = 2.91 \text{ MPa}$$
$$E_s = 201300 \text{ MPa}$$
$$f_y = 345.4 \text{ MPa}$$

$$a_{sx} = a_{sy} = 3.78 \ [\text{cm}^2/\text{m}]$$

Element system with supports, load and the specified material parameters.

The load-displacement curve determined in the test for the slab middle is contrasted with the results of the static calculation in the following diagram. For the SLS the calculation method "*Newton time steps*" was chosen with 60 time increments and an error threshold of 0.1%. The material parameters were set according to the specifications of the authors. The material type *CX-EN* (EN 1992-1-1) was used for this.
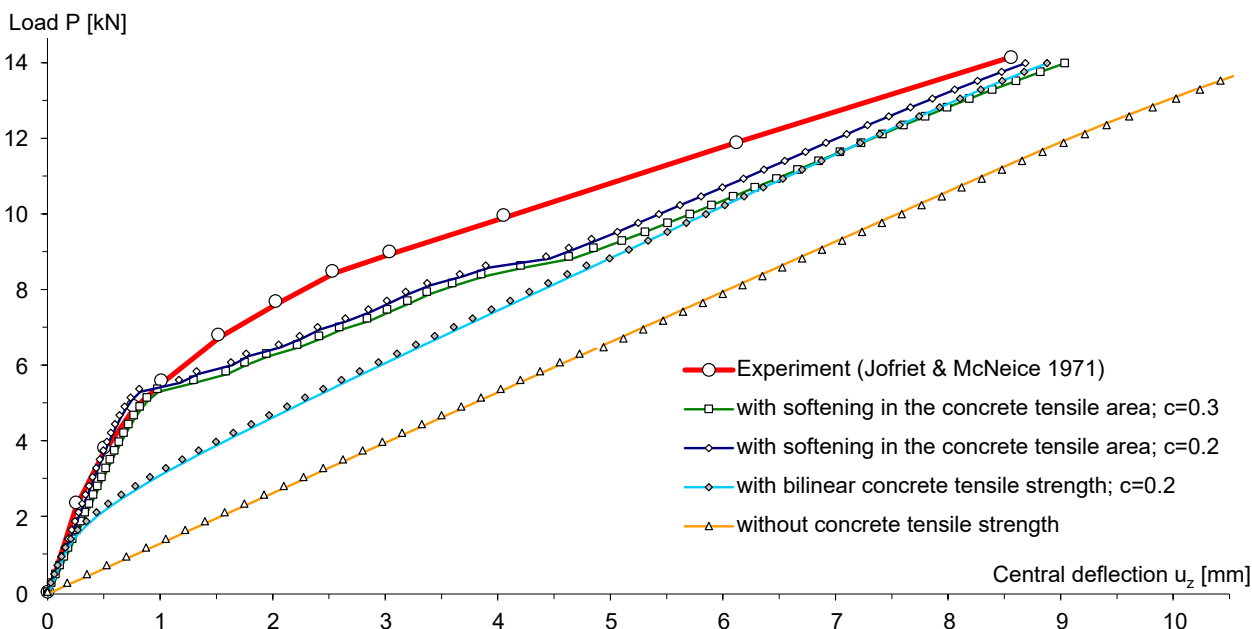
*Load-displacement curves from the crosscheck in SLS and experiment (Jofriet/McNeice)*

In order to demonstrate the mode of action of the methods implemented in the program for the concrete tensile stresses, four variants were calculated. The curve accounting for the concrete tensile strength with softening (c=0.3) exhibits the closest agreement with the test results. The behavior at the beginning of crack formation as well as close to load-bearing capacity display a large level of agreement.

The curve for the bilinear behavior in the concrete tensile area was calculated with the value (c=0.2). The stiffness of the slab is thus, as expected, underestimated at the beginning of crack formation. The load-bearing safety is, however, hardly influenced by this. This means that the calculation is on the safe side.

The curve for the 'naked state II' is for the most part determined by the characteristic curve of the reinforcing steel and thus has exhibits nearly linear behavior in the area under examination.

Experiment of a Reinforced Concrete Frame

The following reinforced concrete frame was analyzed by Ernst, Smith, Riveland & Pierce in 1973 (taken from Krätzig & Meschke 2001). The goal is to demonstrate the plausibility of the achieved calculation results as well as the mode of action of different approaches for determining concrete tensile strength and tension stiffening. The static system with material parameters is shown below.
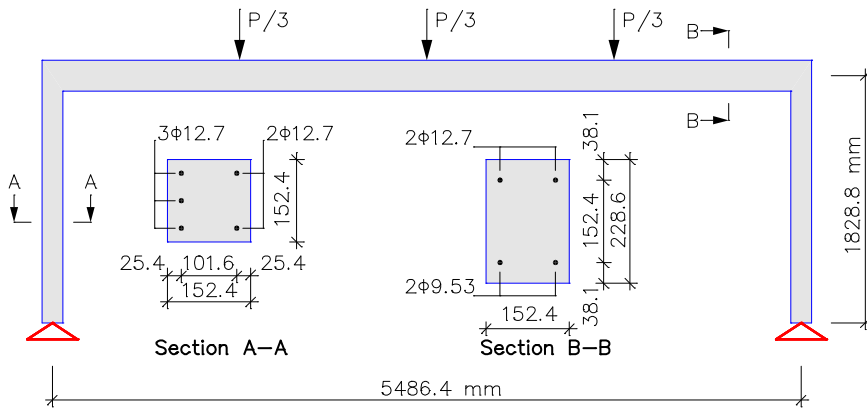
System with sections, load and dimensions [mm]

Material parameters of the experiment:

Concrete: f_{cm} = 40.82 MPa, ε_{c1} = -2.36

Reinforcing steel: $\varnothing$ 9.53: f_y = 472.3 MPa, E_s = 209 GPa (cold-drawn)

$\varnothing$ 12.7: f_y = 455.0 MPa, E_s = 200 GPa (hot-rolled)

Material parameters of the crosscheck:

Concrete: *CX-EN* (EN 1992-1-1), E_c = 33600 MPa, φ_c = 0.07

f_{ck} = f_{cm} - 8 = 32.82 MPa, f_{ctm} = 2.2 MPa

Reinforcing steel: $\varnothing$ 9.53: f_{yk} = 472.3 MPa, $\varnothing$ 12,7: f_{yk} = 455.0 MPa

E_s = 200 GPa, $(f_t/f_y) \cdot k$ = 1.05 (bilinear)

Analysis settings:

SLS with softening (c = 0.2) or without concrete tensile strength

Analysis method: Arc length

Control: Number of increments = 64 / 52

Iterations per arc length: 20

Stiffness: tangential

Initial arc length: ≤ 0.03

The following figure shows stress-strain-curves of the reinforcing steel used for the experiment and the crosscheck within the strain area up to 25 ‰.
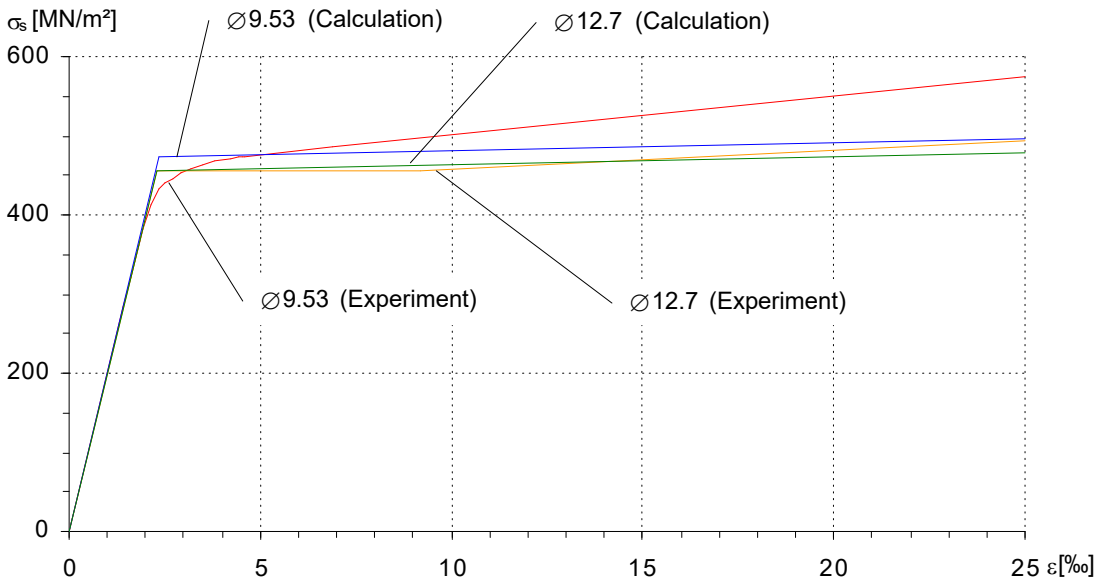
Stress-strain-curves of reinforcement steel from experiment and calculation

The crosscheck was performed according to the arc length method and the second-order theory. Softening in the concrete tensile area was considered for the first calculation variant whereas no concrete tensile strength was assumed for the second variant. According to the experiment, cracking occurs at a limit load of P = 5 kN corresponding to a concrete tensile strength of about 2.2 MPa. To take into account the stress-strain curves of the concrete according to the experiment, a concrete tensile strength f_{ctm} of 2.2 MPa and a creep coefficient φ_c of 0.07 were assumed. The attaining of the system limit load is indicated by stability failure. The failure is caused by reinforcement flow at a load of approx. 35-40 kN and formation of a plastic hinge in the frame center. The slightly lower failure load is due to different stress-strain-curves for reinforcing

steel decisive for the experiment and the crosscheck. As expected, the calculation without tensile strength results in a lower bound for the load-displacement curve of the frame center.
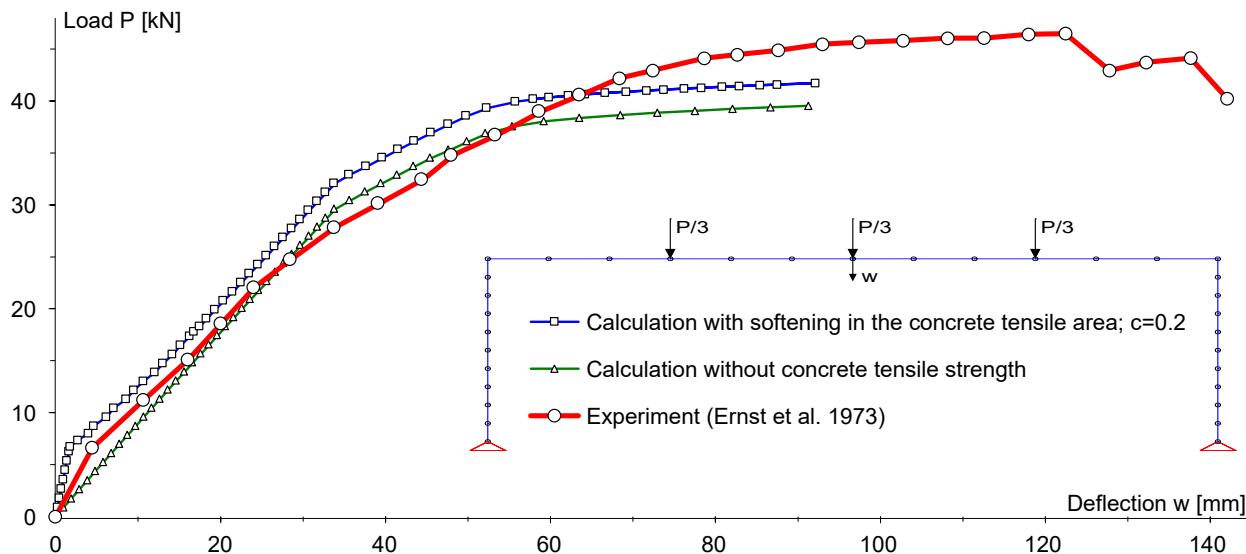

Load-displacement curves from the crosscheck and experiment (Ernst et al. 1973)

Pull Test With Hardening

The recalculation of the pull test shows the behavior of steel with or without strain hardening. A solid model with tetrahedron elements *VT10* is used. To simulate the hardening of the steel the material type *Frei* with the yield criterion *Huber-v.Mises* is used. The 220 mm long specimen, shown below, reacts with plastic behavior when the yield strength (f_{yk} = 240 MPa) is exceeded, as can be easily seen from the stress-displacement curve. The calculation was performed deformation-controlled using the arc length method.

E-Modul: 210000 MPa

ν: 0,3

Hardening modulus H MPa
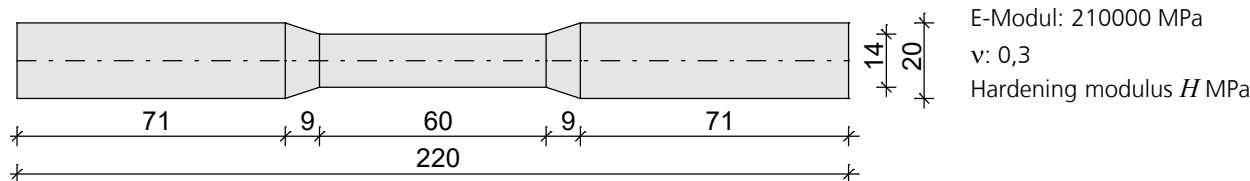
System with dimensions [mm]
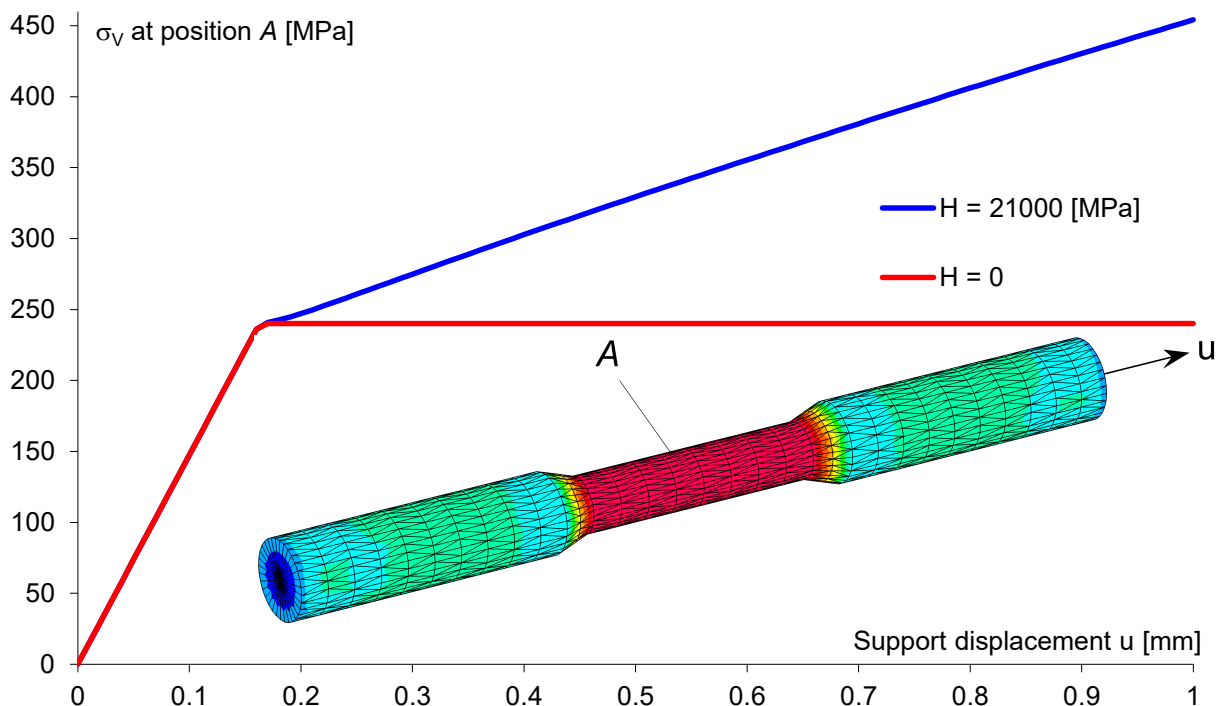
*Evolution of the equivalent stress σ_v with increasing length change of the specimen*
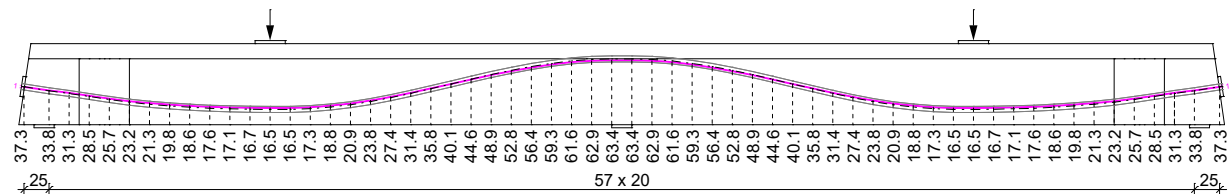
Prestressed Concrete Structure

In this example an experiment of a prestressed two-span beam DLT 2.1 with subsequent bond has been recalculated, which has been carried out at the TU Dortmund as part of a research project of the BASt (Maurer et al., 2015). The dimensions of the test beam are shown below. The structure has a T-beam cross section with a constant height of 80 cm. Also the flange dimensions are constant about the length of the beam with b/h = 80/15 cm. The web thickness within the fields and at the inner support is 30 cm. In the area of the end supports the web thickness increase to 60 cm. A mesh width of 5 cm was chosen for the calculation model. The material type *Frei* was selected for the solid model made of cuboid elements *VQ83*. For the reinforcing steel layers, steel beams were used for the longitudinal and stirrup reinforcement. The applied material properties according to *Hegger et al., BASt, Book B 150* (2020) are given below. The tendon group is automatically implemented in the element stiffness matrices of the solid elements by the program during the load case calculation. The vertical supports have a spring of 500 MN/m per support axis.
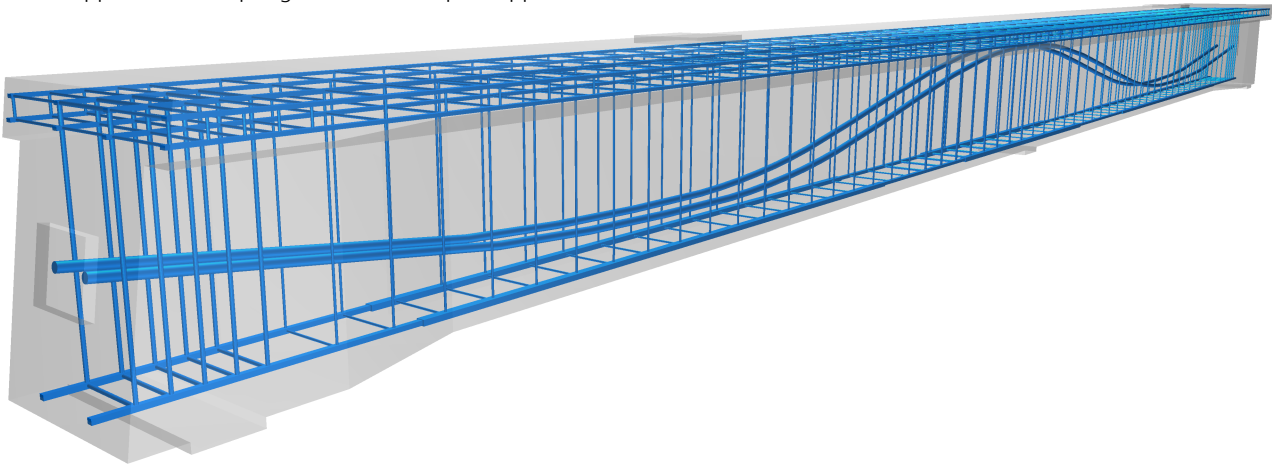
3D view of the calculation model with solid elements in the system viewer
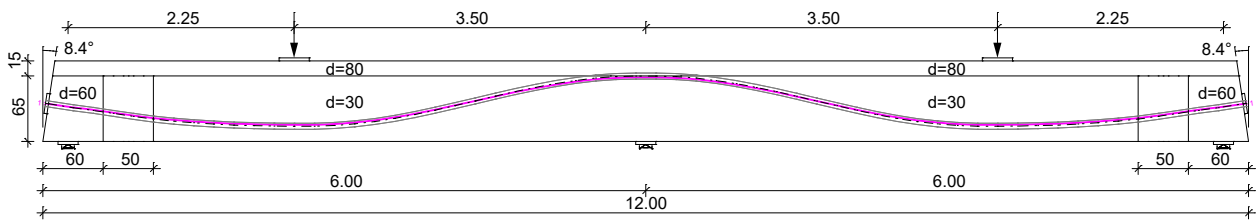
View with system dimensions and depiction of the tendon group

Distance between center axis of the tendon group and the bottom edge of the beam

Prestressing system 1 - SUSPA DSI. Certification according to DIN 4227
Pm0   = 1362.9 kN, Ap = 1400 mm², µa/µn = 0.20, Angle ß' = 0.3 °/m
E-Modulus = 199700 MN/m², ßs/ßz = 1666/1770 MN/m², Slippage = 3.0 mm
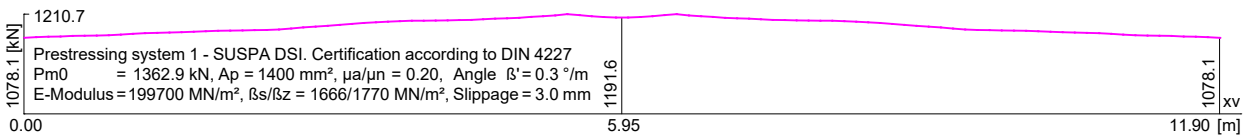
Prestressing force of the tendon group applied for the calculation
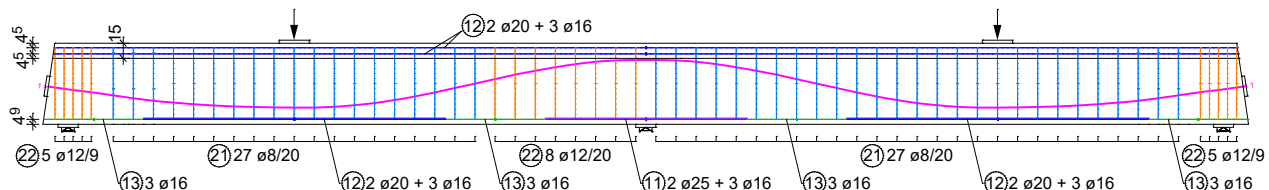
View of the reinforcement (beams) of the calculation model

Reinforcement

| Se-No.	Description	A_s [mm²]	E-Modulus [MN/m²]	f_{yk} [MN/m²]
11	Longitudinal reinf. ø25 + 1.5·ø16 (bottom)	792	199501	555
12	Longitudinal reinf. ø20 + 1.5·ø16 (bottom)	616	200506	567
13	Longitudinal reinf. 1.5·ø16 (bottom)	302	205200	554
14	Longitudinal reinf. 2·ø12 (top)	226	200750	532
21	Stirrups ø8	50	184000	475
22	Stirrups ø12	113	200750	532

Material properties of solid elements made of concrete

Material type	*Frei*
Material model	*Plasticity-damage*
E-Modul [MN/m²]	32860
Gamma [kN/m³]	23
Poisson's ratio [-]	0.2
Compr. strength [MN/m²]	$f_{cm} = f_{ck} + 8 = 41.15$
Tensile strength [MN/m²]	$f_{ct} = 2.688$
Ultimate compressive strain [‰]	2.363
Compr. fracture energy [kN/m]	15
Tensile fracture energy [kN/m]	0.09

The steel plates at the prestressing anchors, the supports and the presses were assumed to be linear-elastic.

The nonlinear system analysis was performed with the following settings:
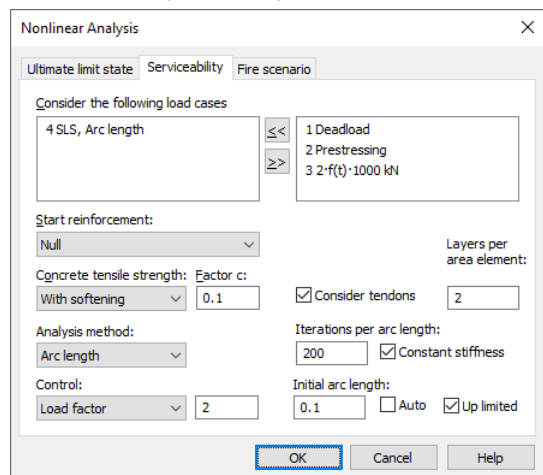
Load data load case 4: SLS, Arc length

Load group (GRL)
Theory: 1. order theory
No soil pressure > 0: No; No support reac. < 0: No; Error threshold [%]: 0.10
Additional global load factor: 1.00; Predeformation: 0
Consider concrete creeping in the nonlinear analysis: No

Selected load cases

No.	Label	Factor
1	Deadload	1
2	Prestressing	1
3	2·f(t)·1000 kN	1
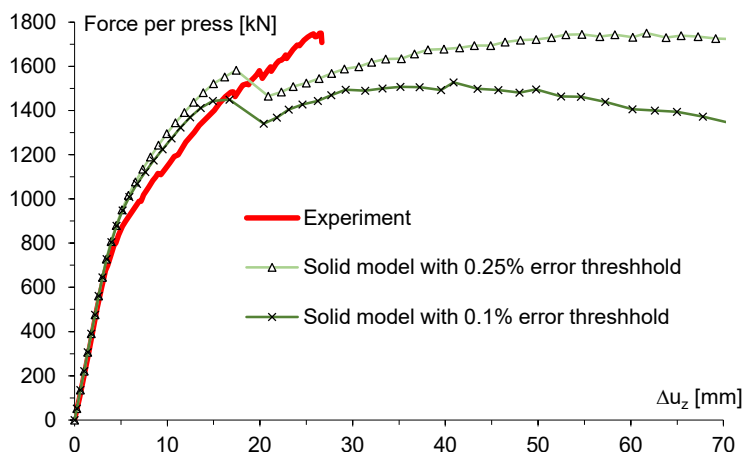
At about 700 kN, all load-displacement curves show a kink in their curve due to cracking. In the experiment, reinforcements were installed at a press load of 1743 kN because of the imminent failure of the structure. As can be seen in the figure on the left, the structure is very sensitive to the set error threshold. The following figures were calculated with the error threshold of 0.1 %.

Load-deformation curves at the load location in field 1 from the comparative calculation and the experiment (Maurer et al., 2015)
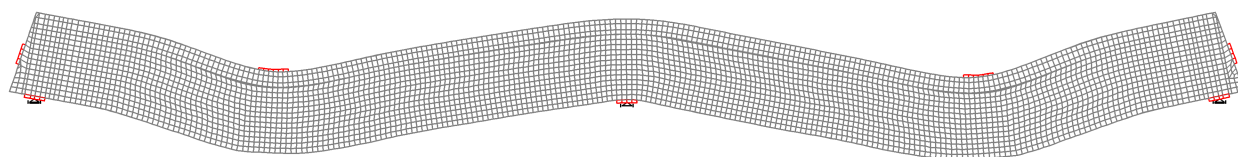
Deflection for press forces of 1500 kN (20 fold superelevated)
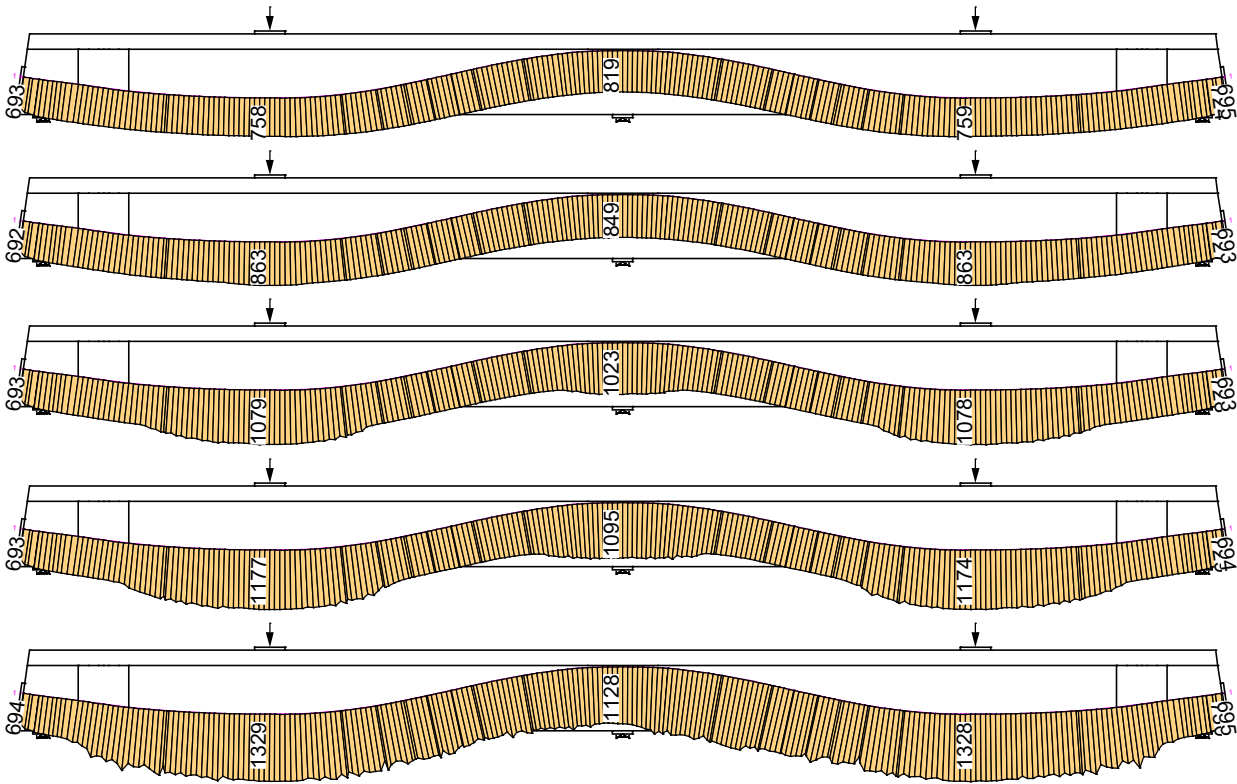
*Prestressing steel stresses σ*p *[MN/m²] for press forces of 0 / 800 / 1200 / 1400 / 1540 kN*
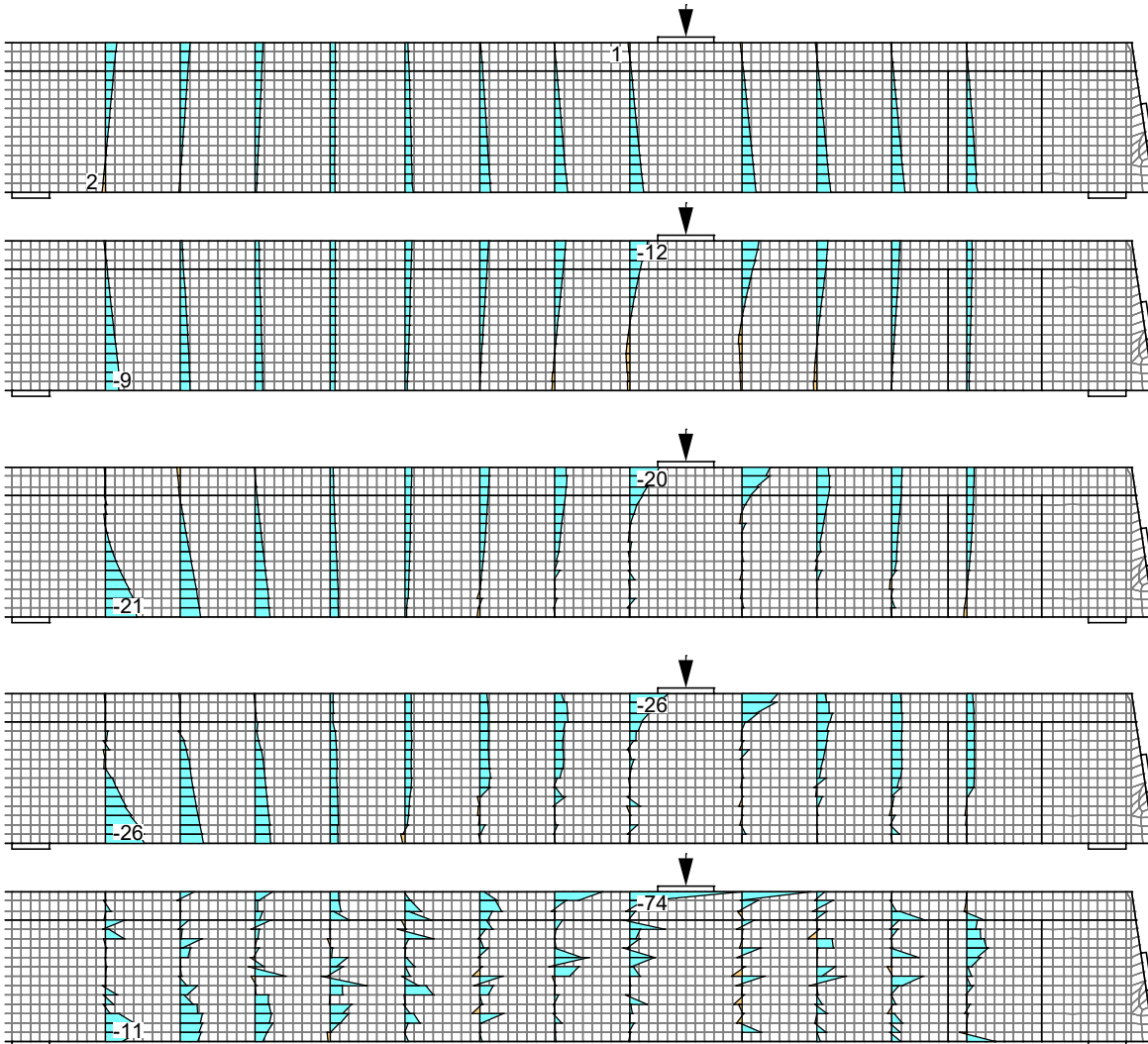
*Horizontal stresses σ*x *[MN/m²] between the stirrups at press forces of 0 / 800 / 1200 / 1400 / 1540 kN*
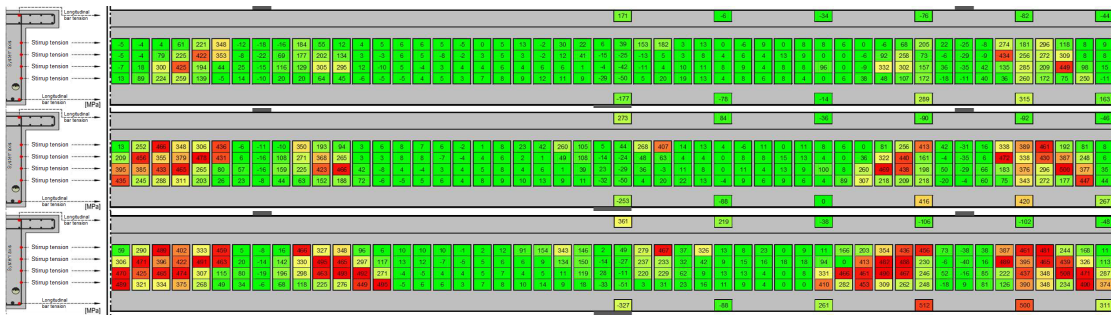
Measured stirrup stress σ [MN/m²] at press forces of 1200 / 1400 / 1540 kN BASt Book B 150, A.2.2.1 (c), (d), (e)
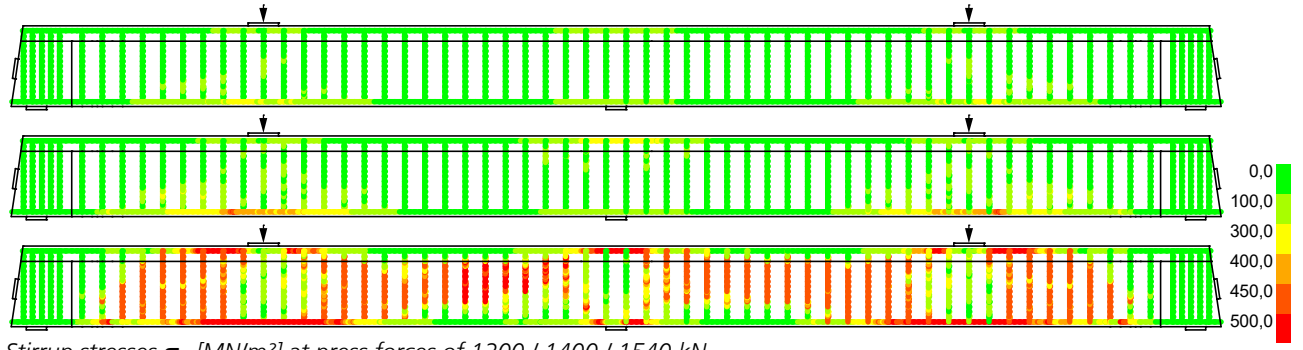
Stirrup stresses σ$_V$ [MN/m²] at press forces of 1200 / 1400 / 1540 kN
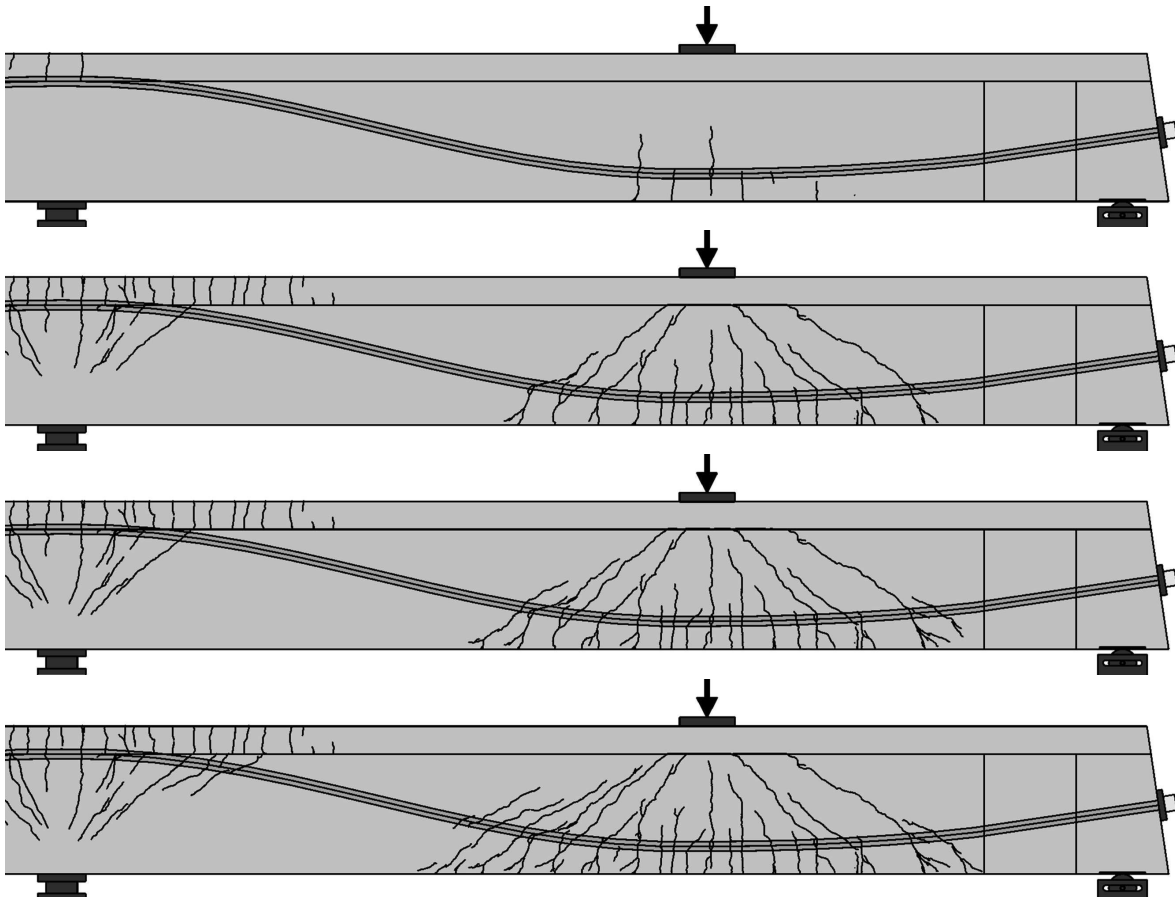
Crack formation of the experiment for press forces of 800 / 1200 / 1400 / 1540 kN (BASt Book B 150, A.2.1.1 (b), (c), (e))
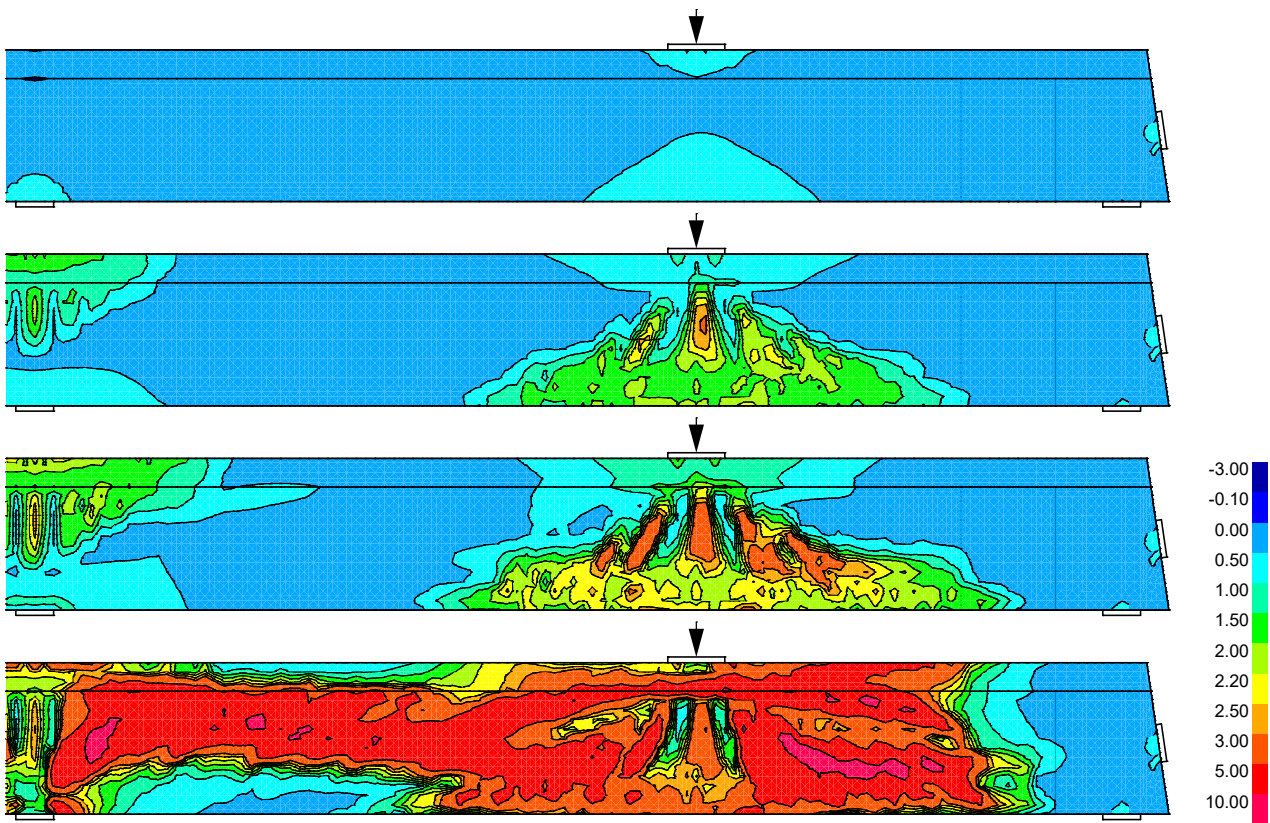
Principle strain ε_1 for press forces of 800 / 1200 / 1400 / 1540 kN
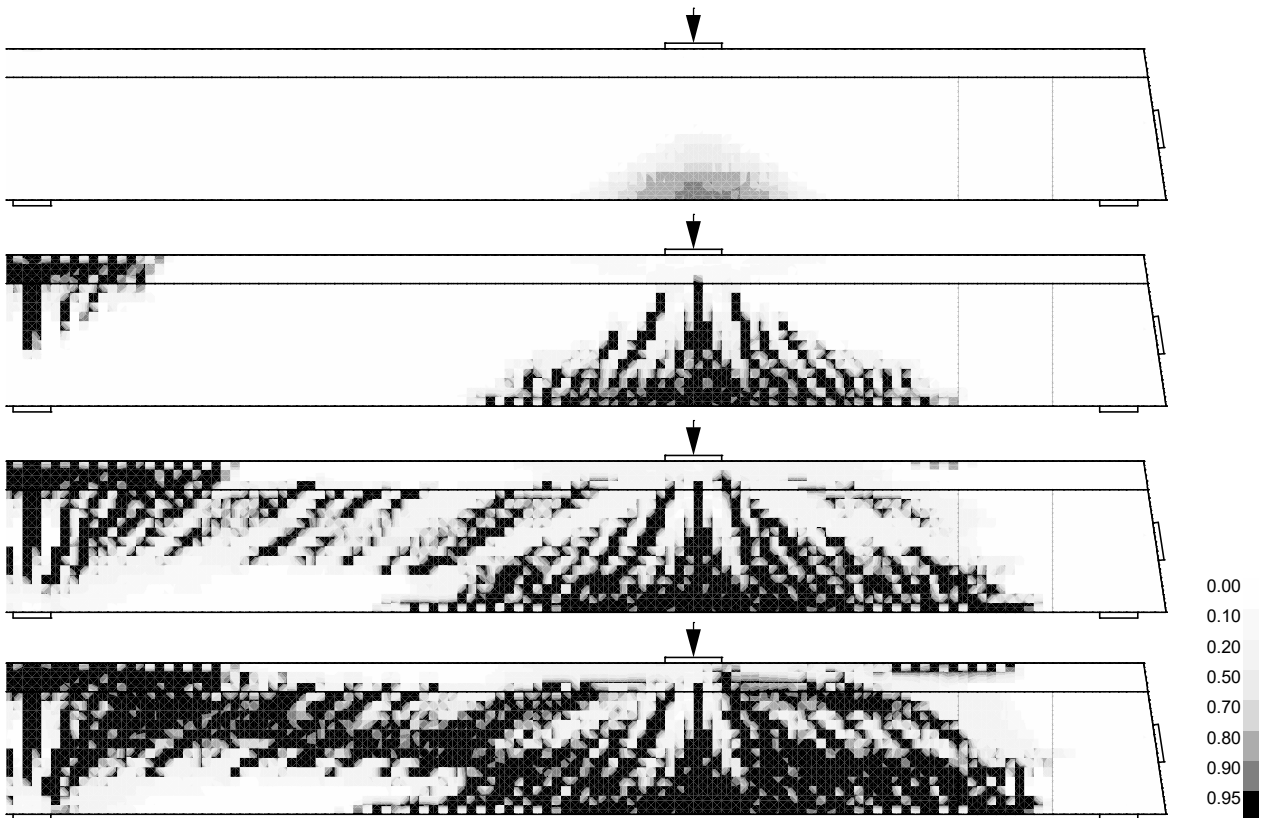
Damage for press forces of 800 / 1200 / 1400 / 1540 kN

Reinforced Concrete Corbel

Based on the experimental results of *Mehmel and Freitag*, which were published in 1967 in the journal "*Der Bauingenieur*", the damage models implemented in *InfoCAD* are analyzed below. The main focus is on the numerically predicted load-bearing capacity and damage prediction ('crack propagation'). Differently reinforced rectangular and trapezoidal corbels were investigated in the test series. The load was applied either directly or indirectly via additionally laterally arranged auxiliary corbels. For the comparative study, a reinforced rectangular corbel with direct load application is used, since numerical results with different approaches for the definition of the material behavior are already available for this test (I.2, reinforcement according to *Mehmel*). Figure 1 shows the corbel created with InfoCAD, including the geometry, boundary conditions and reinforcement. A three-dimensional calculation is essential here, since a simplified finite element simulation with plain or shell elements would underestimate the load-bearing capacity by about 40% (*Krejci and Mang*, 1986).
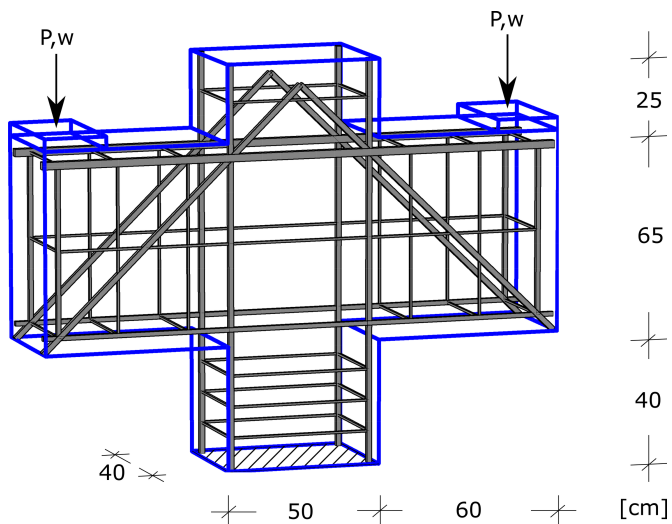

Figure 1:   Geometry, boundary conditions and reinforcement

Two simplifications were made when modeling the reinforcement. The first simplification results from the facts that the distance of the stirrups in the lower part of the column was not specified by *Mehmel and Freitag* and that a larger number has no decisive influence on the load-bearing behavior. Instead of seven stirrups, only three equidistant arranged stirrups were considered. The second simplification concerns the longitudinal reinforcement in the lower and upper part of the crossbeam as well as the diagonal reinforcement. Reinforcement bars that are directly adjacent to each other were combined into one cross-section:

Crossbeam top: 2x[2x∅16 + 1x∅14], diagonal bars: 4x[2x∅14] (cf. *Mehmel and Freitag, 1967*). The reinforcement in the thickness direction was assumed to be ∅8 everywhere. A detailed list of bar diameters used, quantities installed and strengths is given in Table 1.

Quantity	Type	∅	Location	E-Modulus [MPa]	f_{yk} [MPa]
9	Stirrups	8	Crossbeam: 5, Column: 4	206000	430
4	Bars	8	Crossbeam: 2x1 left, 2x1 right	206000	430
10	Bars	16	Crossbeam: 2x2 top, 2x1 bottom Crossbeam: 2x1 left, 2x1 right	206000	430
10	Bars	14	Crossbeam: 2x1 top, Diagonal: 4x2	206000	430
4	Bars	18	Column: 4x1	206000	430

Table 1:   Quantity and diameters of reinforcement bars and material properties

In addition to determining the steel bar strengths (~4400 kg/cm² corresponds to ~430 MPa), the concrete compressive strength was also determined during the tests. The result was a cube compressive strength of f_c = 226 kg/cm². The modulus of elasticity and the tensile strength are not mentioned in the publication by *Mehmel and Freitag*. In order to compare the *InfoCAD* results with the other numerical results, the material parameters for concrete were chosen as follows:

E = 21870 MPa, v = 0.2, f_c = 22.6 MPa, f_t = 2.3 MPa.

The numerical analysis is performed using both isotropic damage models available in *InfoCAD* (*De Vree* and *Mazars*). Table 2 shows the parameters for defining the corresponding damage functions or stress-strain relations.

N	Damage model	A	B	A_t	B_t	A_c	B_c
1	*De Vree*	0.45	400	-	-	-	-
2	*Mazars*	-	-	0.7	*auto*	0	*auto*

Table 2:   Damage parameters

Taking advantage of the double symmetry, the calculation is performed with only one quarter of the reinforced concrete corbel. In addition, the influence of the element size on the numerical result is shown on the basis of two different discretizations (see Figure 2; Mesh A: 4097 tetrahedral elements and 324 beam elements, Mesh B: 94968 tetrahedral elements and 939 beam elements).
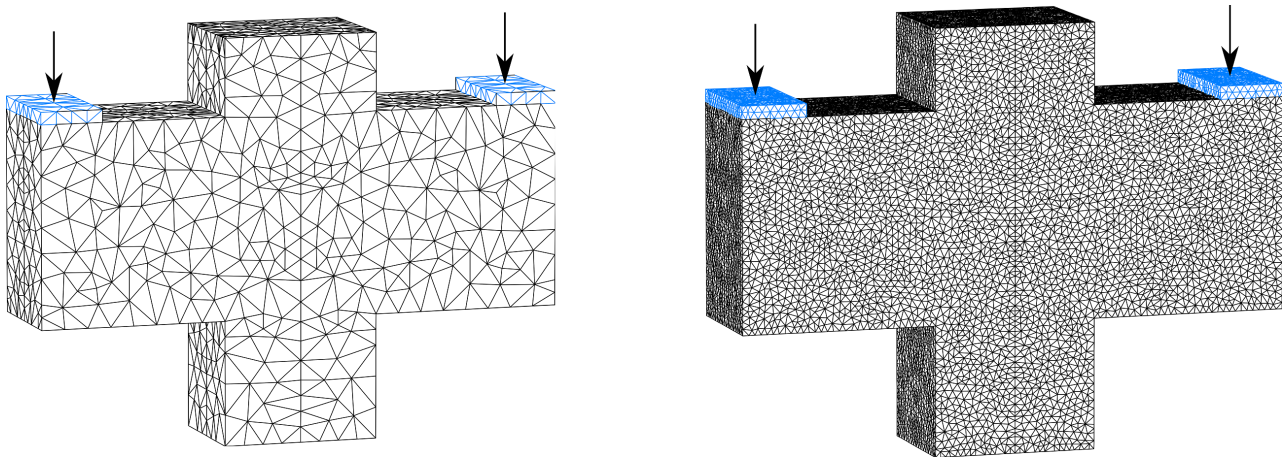

Figure 2:   Discretization of the reinforced concrete corbel

The arc length method was used as the calculation method in all cases: Error threshold 1%; Iterations per arc length 20; Initial arc length 0.1; Up limited; Constant stiffness. A displacement-controlled load was applied. Steel plates are placed at the load application points.

Figure 3 illustrates the crack propagation (traced here) recorded photographically during test execution. The condition of the concrete within the white areas before reaching the failure load is not known, see also *Mehmel and Freitag* (1967).
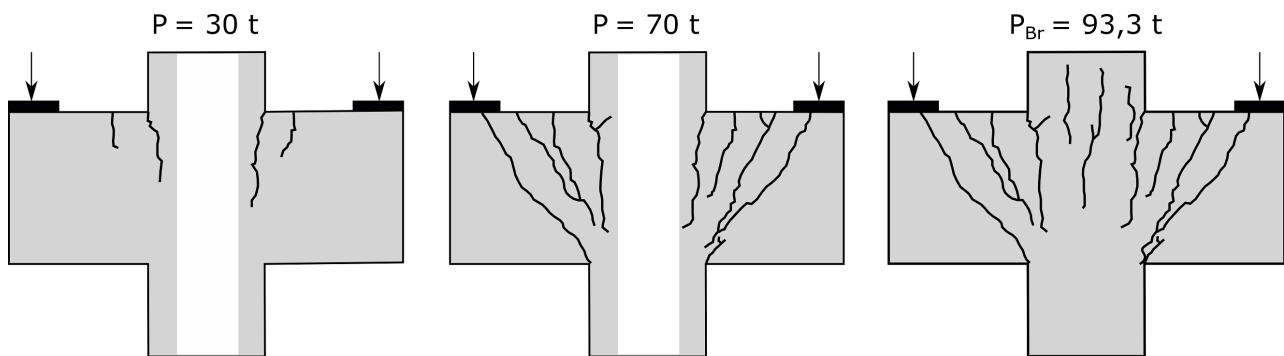
Figure 3:   Crack propagation during test execution

The numerically determined damage distributions shown in Figure 4 are comparable to the crack distributions observed during the experiment. Due to the continuum-based damage formulation used in *InfoCAD*, the cracks are not defined discretely but smeared. Therefore, there is a direct correlation between element size and 'crack width'. A comparison of the damage distribution resulting from different discretization (see Figure 2) shows this very clearly, cf. Figure 4 top (Mesh A) and bottom (Mesh B).

The crack propagation associated with the load increase causes a significant increase of the stresses in the reinforcing bars in the damage-relevant areas of the structure, see Figure 5. While in the test the diagonal bars started yielding before all other bars, in the numerical simulation the internal stirrups of the connected crossbeams reach the yield stress first. This is due to the fact that numerically, contrary to the observations during the experiment, up to a load of 70 t, no gaping crack occurs from the point of load application to the indented corner at the other side of the load (cf. Figure 3 and 4, center). After verification of damage distributions and steel stresses, the two damage models are finally analyzed with regard to their predictions of the load-bearing capacity.
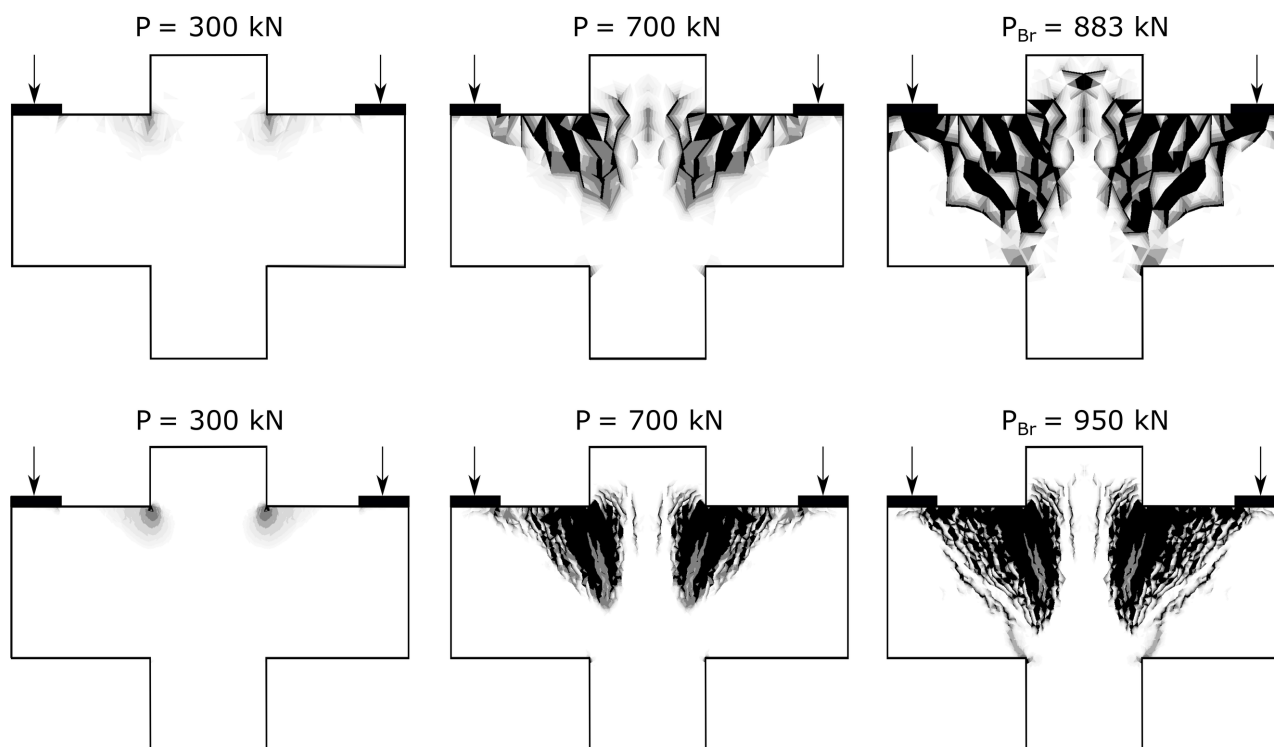
Figure 4:   Damage distribution – De Vree (D = 0: white, D > 0,9: black)
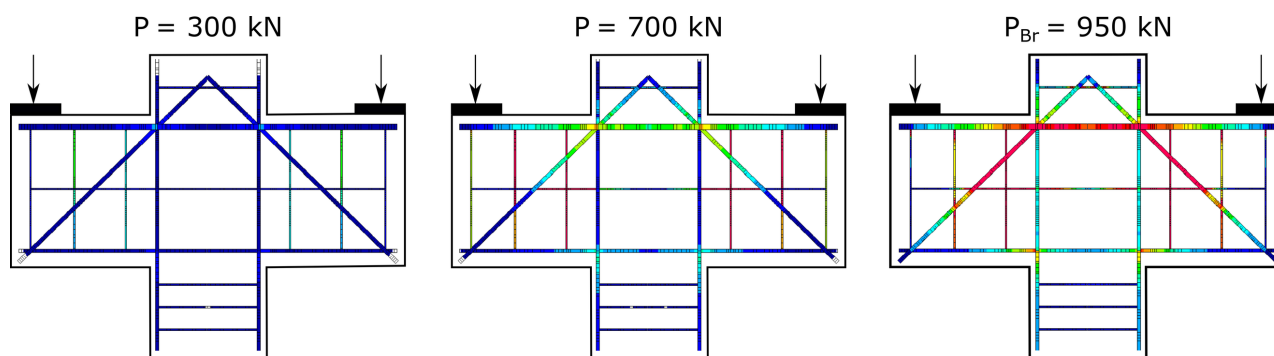
Figure 5:   Steel stresses (Mesh B) – De Vree (σ_V = 0: white, σ_V = 430MPa: red)

A very good agreement is achieved here for the ultimate load. While an ultimate load of P_{Br} = 93.3 tons was determined in the test, values between 883 kN and 962 kN are predicted numerically (depending on the damage model and discretization).
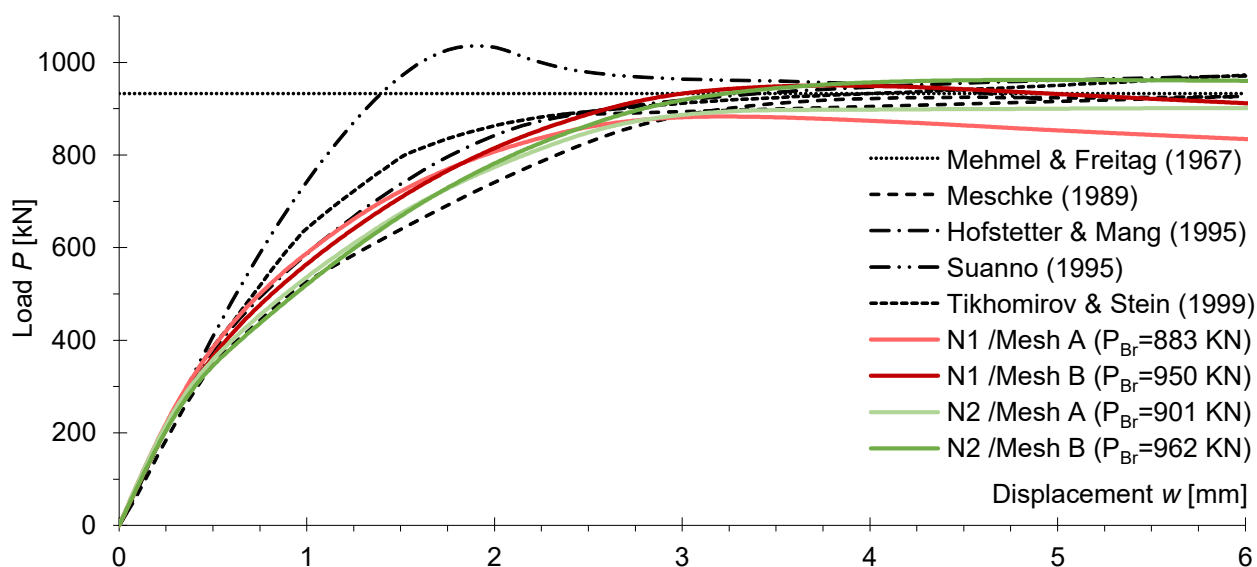
Figure 6:   Comparison of experimentally determined ultimate load (93.3 t) and numerically determined load-displacement curves (chosen parameters, see Table 2)

Unfortunately, no comparison of load-deformation curves can be made because the load history was not recorded during the tests. Therefore, simulation results from a total of four different publications (*Meschke* 1989, *Hofstetter & Mang* 1995, *Suanno* 1995, *Tikhomirov & Stein* 1999) serve as reference solutions, see Figure 6. Taking the *InfoCAD* solutions into account, only minor differences between the individual load-displacement diagrams can be identified. First of all, all curves are almost congruent up to a load of approx. 350 kN. While the model of *Meschke* (1989) predicts an early degradation of the corbel stiffness with an almost ideal plastic yielding after reaching the ultimate load, the model used by *Suanno* (1995) results in only a minimal stiffness degradation before a relatively strong decrease after exceeding the maximum load occur. With the model of *Tikhomirov & Stein* (1999), no definite ultimate load can be determined. Here, an increase in load results in a linear increase of the load-bearing capacity. In the same way as in *Meschke* (1989), *Hofstetter & Mang* (1995) also show an ideal-plastic material behavior after reaching the ultimate load. The InfoCAD results are in between the results from the latter two publications. While the *Mazars* model also predicts nearly ideal-plastic yielding after reaching the maximum load, the parameters chosen when using the *De Vree* model imply a slight degradation of the corbel stiffness. To achieve ideal-plastic material behavior, the parameter A (*De Vree*) or $A_{t,c}$ (*Mazars*) must be set to zero.

Unreinforced Concrete Structures

The validation of the implemented elasto-plastic damage model (plasticity-damage), which is available in *InfoCAD* for solid elements of the material type *Frei*, is done, among others, with the help of the experimental results of *Petersson* (1981) and *Winkler* (2001). Their experimental results serve as a reference and are often used in the development of nonlinear material models to verify numerically determined solutions, such as load-displacement curves. Both structures discussed below are unreinforced. First, *Petersson's* 3-point bending beam (with a notch in the center of the span) is analyzed. Due to the geometry and boundary conditions, the 'crack' that occurs with increasing load is in *Mode I* only (opening of the crack edges perpendicular to the crack plane). If additional sliding of the 'crack edges' (*Mode II*) is observed, the 'crack' is in the so-called *mixed mode*. This type of crack loading occurs with *Winkler's* L-shaped slab.

3-point bending test according to Petersson

The dimensions of the single-span beam with a notch in the center investigated by *Petersson* (1981) in his dissertation, as well as its boundary conditions and discretization with solid elements (*VQ83*) are shown in Figure 1. The width of the notch (2 cm) corresponds to the smallest mesh width below the load application (*Rots et al.,* 1985).
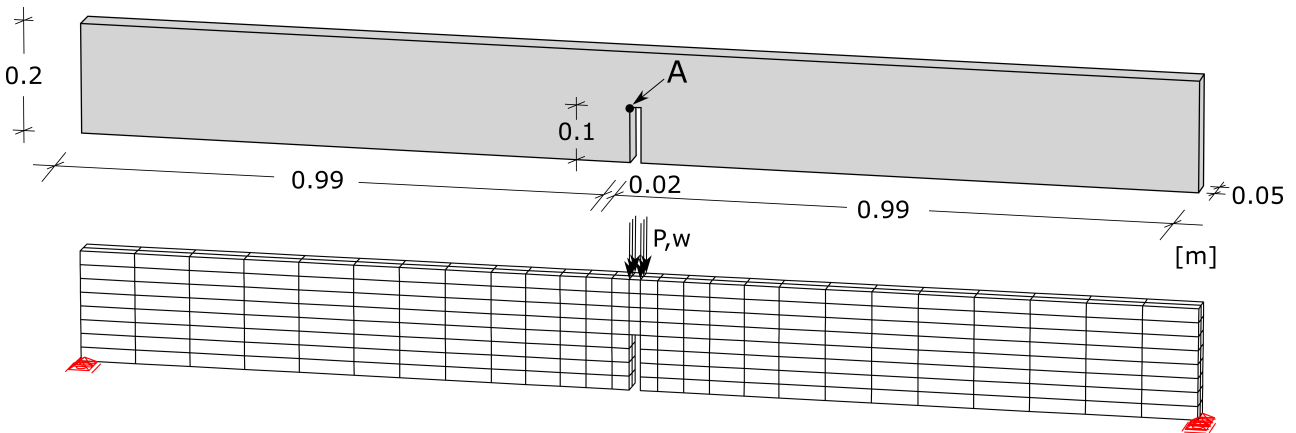
Figure 1: Geometry, boundary conditions and discretization (424 elements)

The point A drawn in the figure below is used to evaluate the inelastic and plastic strains and the damage over the entire load path. The load on the statically determinate supported 3-point bending beam was applied in a displacement-controlled manner.

Parameters	Material			Arc length method	
	E-Modulus [MPa]	30000		Error threshold [%]	0.001
	Poisson's ratio [-]	0.2		Number of iterations	200
	Compressive strength f_c [MPa]	43		Initial arc length	0.01
	Tensile strength f_t [MPa]	3.33		Upward limited	yes

Table 1: Parameters (material and arc length method)

The arc length method was used as the calculation method. Together with the material parameters used, the selected error tolerance, number of iterations and initial arc length are shown in Table 1. In order to show differences between the implemented nonlinear solid models (here: combined model according to *Lubliner* and *Lee & Fenves* as well as pure damage according to *de Vree*), the influence of the *de Vree* model parameters on the numerically predicted ultimate load and softening is analyzed in addition to the validation of the elasto-plastic damage model (in *InfoCAD*: plasticity-damage). A total of four different simulations are performed for this purpose. All model parameters used are listed in Table 2. While in

the case of the combined model (N1), the fracture energies measured by means of concrete specimens during the test (concrete age: 28 days / average values: G_t = 124 N/m, G_c = 23 kN/m) are directly included in the numerical calculation and determine both the ultimate load and the softening process, in the case of the *De Vree* model (currently no consideration of fracture energy regularization), an adjustment of the stress-strain relationship must be made via parameters A and B.

N	Material model	A	B	G_t	G_c	ε_{c1}
1	*Plasticity-damage*	x	x	124 N/m	23 kN/m	2.2
2	*Damage / De Vree*	0.98	10	x	x	x
3	*Damage / De Vree*	0.98	100	x	x	x
4	*Damage / De Vree*	0.98	1000	x	x	x
5	*Damage / De Vree*	0.98	230	x	x	x

Table 2:   Parameters material models

The difference between the two models or in their handling can be seen in the load-displacement curves (*InfoCAD*) illustrated in Figures 2 and 3.
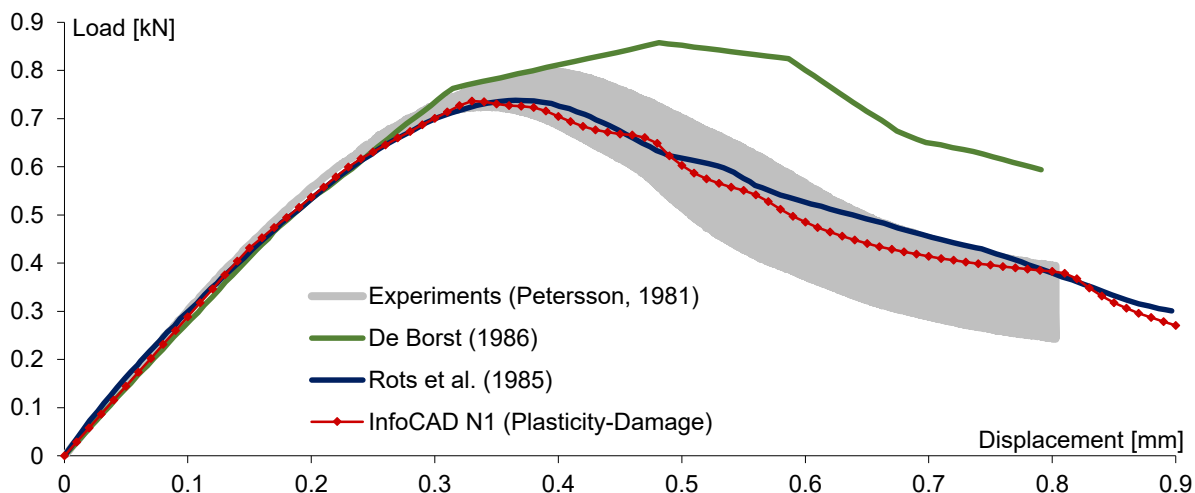
Figure 2:   Comparison of experimentally and numerically determined load-displacement curves. (InfoCAD: plasticity-damage)
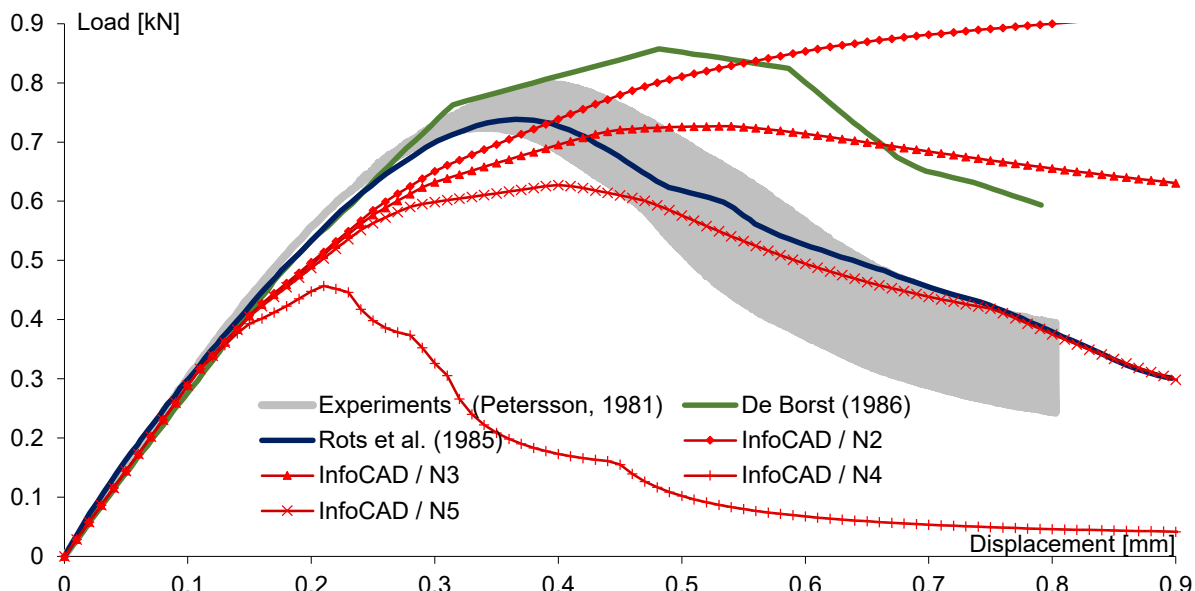
Figure 3:   Comparison of experimentally and numerically determined load-displacement curves. (InfoCAD: De Vree)

Using the elasto-plastic damage model (plasticity-damage) and the fracture energies (G_t, G_c) known from experiments, very good agreement is obtained with the load-displacement curves recorded during the experiment. An adjustment of the model parameters is not necessary. Both, the ultimate load and the softening material behavior are numerically predicted with sufficient accuracy. This is also shown by a comparison with other numerical results (*De Borst,* 1986; *Rots et al.* 1985). The situation is different with the results shown in Figure 3. It is obvious that the *De Vree* model requires a parameter study for a realistic representation of a particular material behavior. The ultimate load and the degree of stiffness reduction are

strongly coupled. Modeling a large increase in damage results in a reduced ultimate load, while a slow increase in damage results in an increased ultimate load (controlled by parameter B).
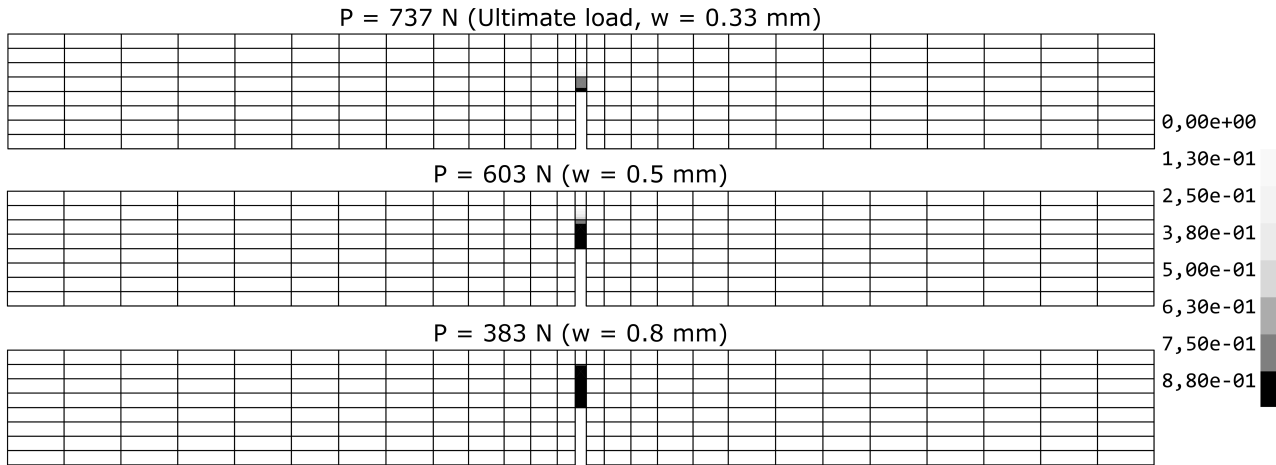
Figure 4:   Propagation of damage with increasing load (plasticity-damage)

For further analysis, but also to show possible result representations in *InfoCAD*, further numerical results of the combined model are evaluated here in addition to the load-displacement curve (see in Figure 2). These include the damage occurring with increasing load (Figure 4) as well as the inelastic (ε^{in}) and plastic (ε^{pl}) strains (Figure 5).
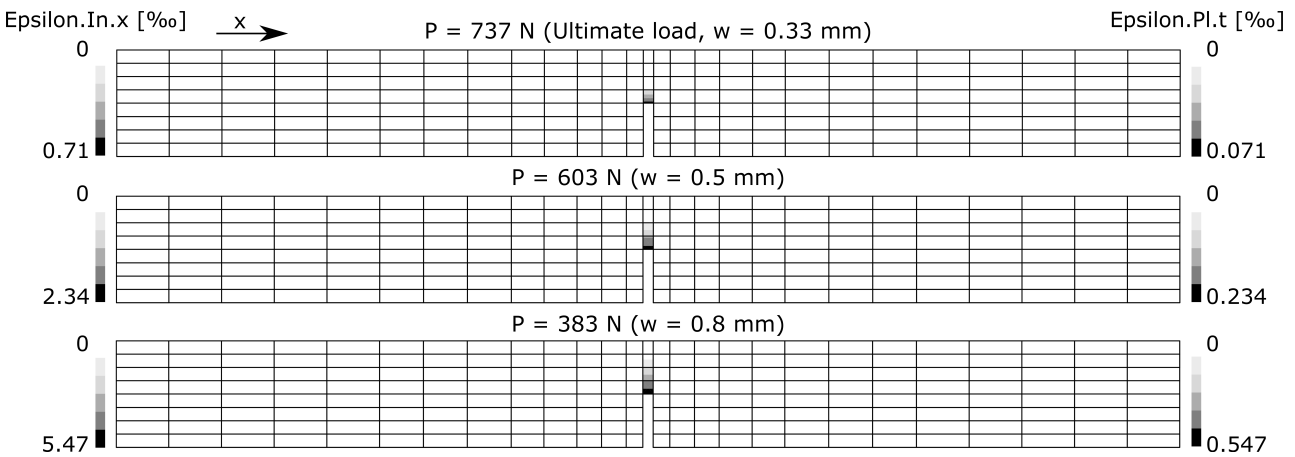
Figure 5:   Propagation of inelastic (In.x) and plastic (tension: Pl.t) strains with increasing load (plasticity-damage).

In addition, the relationship between the latter quantities (for uniaxial tension: $\varepsilon_t^{pl} / \varepsilon_t^{in} = 0,1$, see combined model, Figure 17), can be directly derived from the results of the *Petersson* experiment.
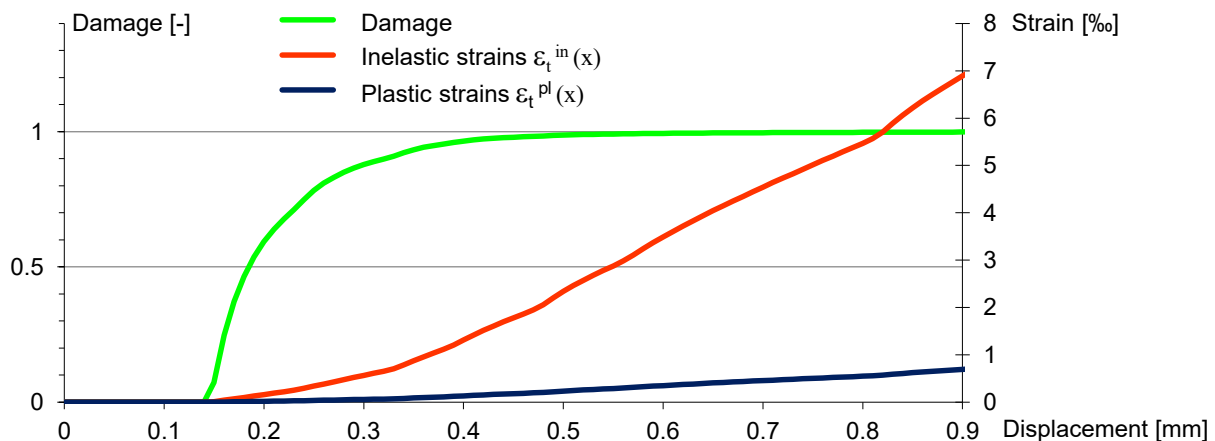
Figure 6:   Propagation of damage and inelastic and plastic strains at point A.
(see figure 1, plasticity-damage)

Either by looking at the contour plots, which also vividly illustrate the different degradation state within the entire structure, including when the ultimate load is reached ('crack initiation and crack propagation' above the notch), or by looking at Figure 6, which illustrates the propagation of both the damage and the inelastic and plastic strains over the entire loading path (the evaluation is done at point A, see Figure 1).

L-slab according to Winkler

In order to confirm the very good reproduction capability of the elasto-plastic damage model (plasticity-damage) with respect to stiffness degradation and damage propagation, as established in the analysis of the single-span beam (*Petersson,* 1981), the numerical results are verified on the basis of a second series of tests. This is an unreinforced L-shaped slab investigated by *Winkler* (2001) in his dissertation.
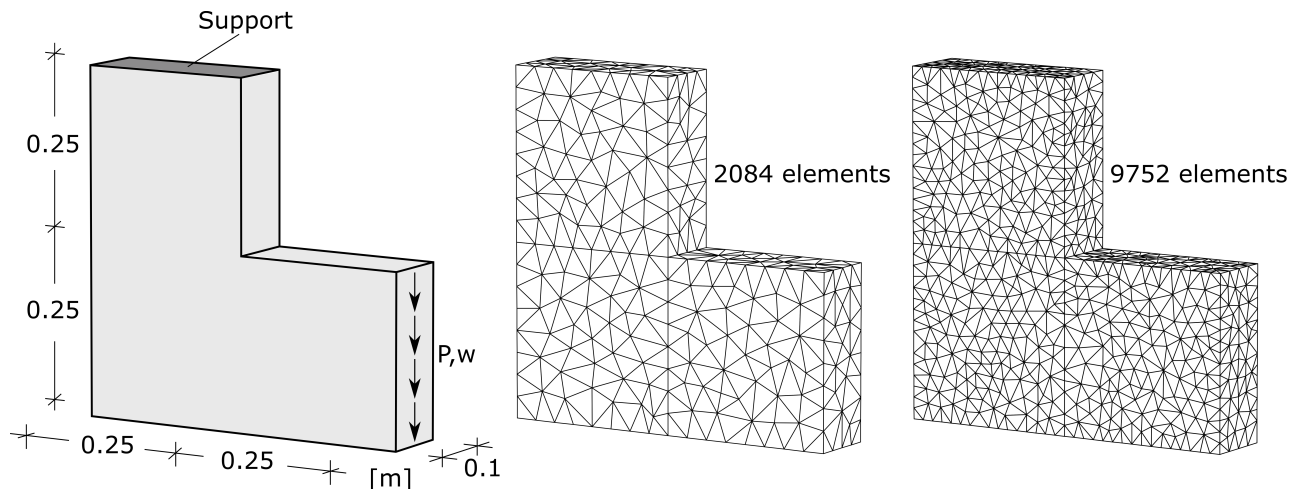
Figure 7:   *Geometry, boundary conditions and discretizations*

The geometric dimensions and boundary conditions are shown in Figure 7. Furthermore, two discretizations with different mesh widths are shown. Numerical analyses should provide information on the influence of the element size on the softening behavior. In order to minimize the stresses and thus any damage in the support area, the L-slab is supported in a statically determinate manner. In addition, in analogy to the 3-point bending beam, the load is also applied here in a displacement-controlled manner. As a result of the arc length method, which is again used as a calculation method, the representation of load-displacement curves as well as the increasing damage at selected nodes of the discretized structure over the course of the load is directly possible. The same applies to the inelastic and plastic strains.

Parameters	Material			Arc length method	
	E-Modulus [MPa]	25850		Error threshold [%]	0.01
	Poisson's ratio [-]	0.18		Number of iterations	50
	Compressive strength f_c [MPa]	33		Initial arc length	0.02
	Tensile strength f_t [MPa]	2.7		Upward limited	yes

Table 3:   *Parameters (material and arc length method)*

However, in contrast to the evaluation of the results of the single-span beam, in the following only load-displacement curves are verified or compared with the curves recorded during the experiment. However, two contour plots are included, which clearly show the relationship between deformation and damage ('crack progression'). Table 3 contains relevant material parameters and all necessary parameters for controlling the calculation with the arc length method. On the other hand, two further material parameters, which represent input parameters of the combined model, namely the two fracture energies (tension: G_t, compression: G_c), are shown in Table 4. The default values defined in *InfoCAD* (G_t = 100 N/m, G_c = 15 kN/m, ε_{c1} = 2.2 p.m.) were not changed for the FE simulations.

There is also a comparison of combined model (plasticity-damage) and pure damage model (*De Vree*) in this validation example. The chosen parameters (*A* and *B*) for generating the uniaxial stress-strain relation according to *Peerlings* (1999) can also be taken from Table 4.

N	Material model	A	B	G_t	G_c	ε_{c1}
1	*Damage / De Vree*	0.98	140	x	x	x
2	*Plasticity - damage*	x	x	100 N/m	15 kN/m	2.2

Table 4:   *Parameters material models*

Again, using the elasto-plastic damage model shows a very good correlation between numerically and experimentally determined load-displacement curves, see Figure 8. The ultimate load is predicted with sufficient accuracy for both discretizations. However, due to the smaller characteristic length in the case of the fine mesh (9752 elements) and the associated increased element-specific fracture energy, a minimally lower stiffness reduction in the post-failure region can be observed.
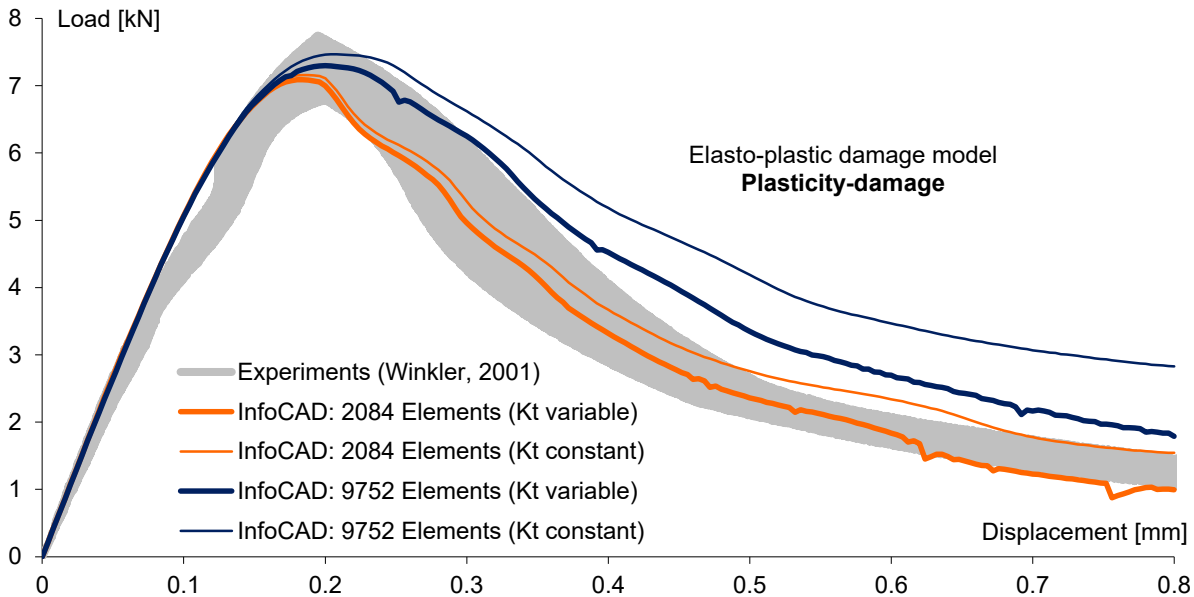
Figure 8:   *Comparison of experimentally (Winkler, 2001) and numerically (InfoCAD) determined load-displacement curves*

For both FE meshes, the analysis was also performed with constant stiffness (linear stiffness method). As expected, the curves are above those with variable stiffness. However, especially for complex structural analyses and stress conditions, constant stiffness is recommended for the calculation. Figure 9 shows the vertical displacement (left) together with the damage distribution (right) for the last load step (w = 0,8 mm).
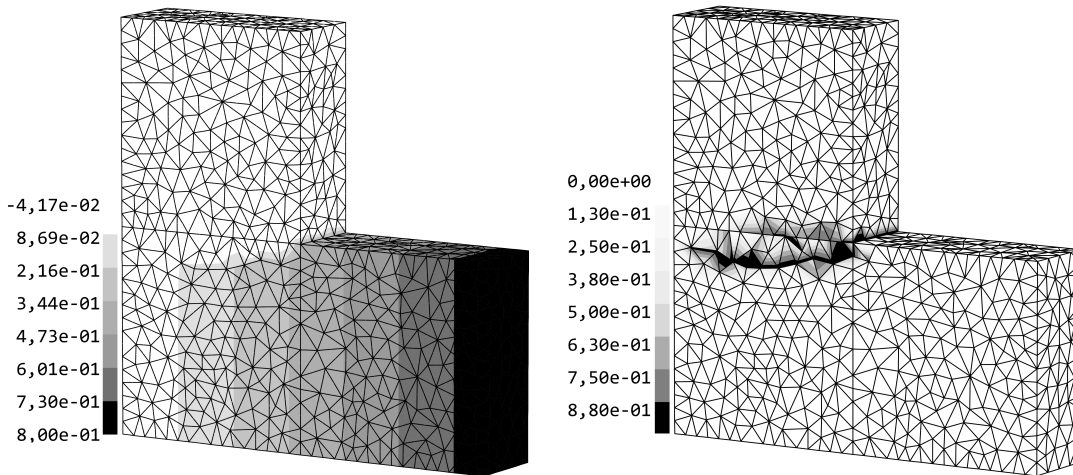
Figure 9:   *Vertical displacement (left) and damage propagation (right)*

The resulting, almost stress-free, 'crack' propagates in the same way as in the experiment (*Winkler,* 2001) in a slight arc from the inward corner to the opposite side of the slab. Both contour plots are from the simulation with fine discretization and variable stiffness.

While the combined model already achieves very good results with the standard model parameters (Table 4), the use of the *De Vree* model requires an adjustment of the parameters (possibly several times) in order to reproduce the real material behavior (see previous section). A parameter study carried out in advance, but not described in detail here, showed an acceptable stress-strain relationship for the parameters shown in Table 4. The ultimate load is slightly underestimated with the fine FE mesh, but the post-cracking behavior is predicted with sufficient accuracy. Above this load-displacement curve lies, as expected, the curve determined with broad discretization. In this case, the calculation model delivers a too low degradation of the material after exceeding the ultimate load. The post-cracking behavior thus deviates from the softening curve observed in the experiment.

Figure 10:   Comparison of experimentally and numerically (InfoCAD) determined load-displacement curves

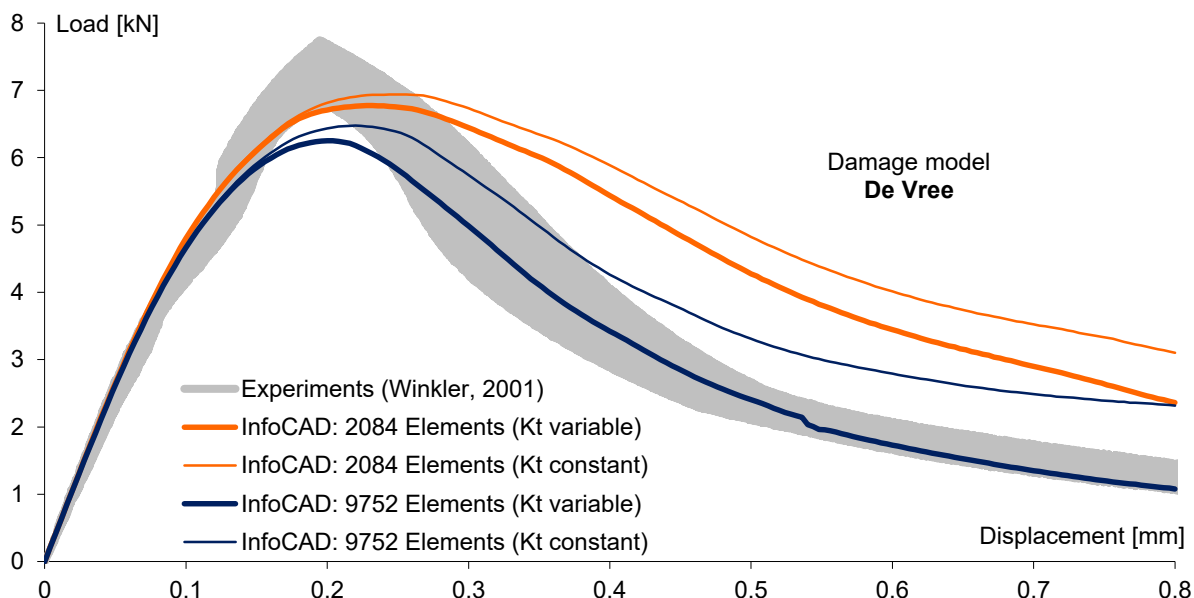The interrelationships between ultimate load and softening process as well as any parameter studies to be carried out to generate an adequate uniaxial stress-strain relationship have already been discussed in the case of the single-span beam with notch (*Petersson,* 1981). Repeated explanations are therefore not provided here and instead reference is made to the previous section.

Bearing Capacity Failure of Foundation and Embankment Failure

The *Mohr-Coulomb* plasticity model is available in *InfoCAD* for determining the load-bearing capacity of soils and predicting possible failure scenarios such as the formation of slip surfaces. The model can be used both for foundation failure analyses and for estimating the stability of embankments (*Phi-c Reduction*).

Bearing Capacity Failure of Foundation

The verification of the numerical results is done here on the basis of the problem considered by *Zienkiewicz et al.* (1975). In the same way as in the cited publication, the numerical analysis is performed using both associative and non-associative flow rule. In *InfoCAD*, the approach used for the calculation is determined by the appropriate choice of the dilatancy angle ψ. In Figure 1, all material parameters (dialog of material properties) are shown together with the dimensions and boundary conditions of the soil model (half system).
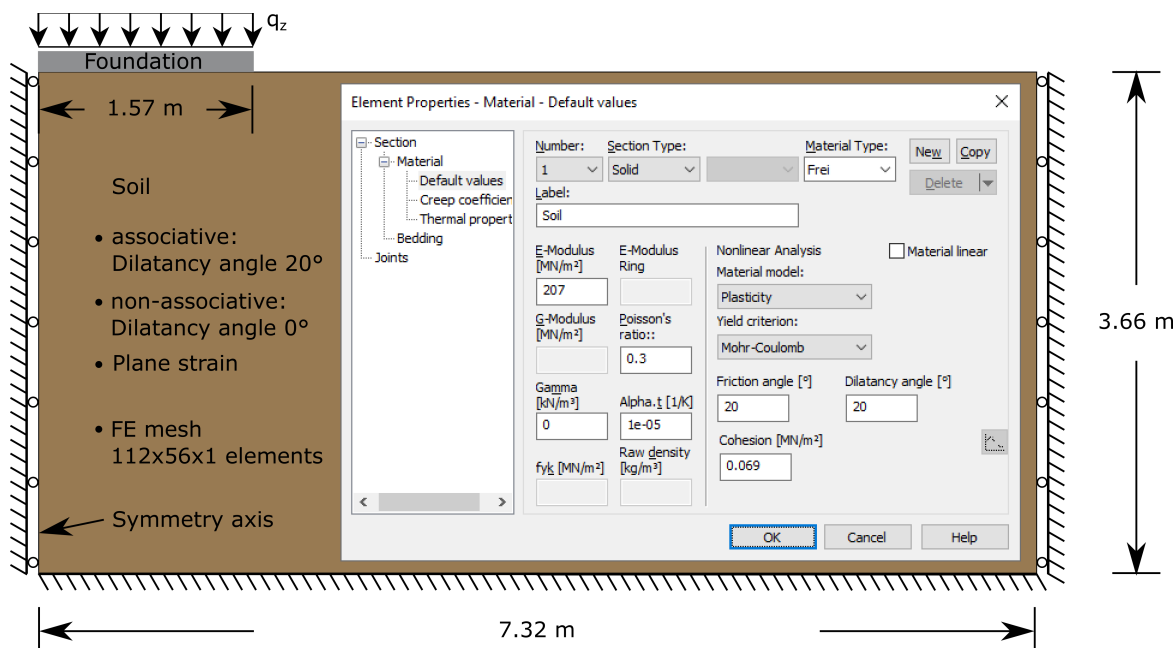

Figure 1:   Dimensions (thickness d = 1 m), boundary conditions and material parameters

In order to show the influence of the foundation stiffness on the deformation behavior and the bearing capacity of the soil,

two cases are investigated, a rigid and a flexible foundation. Numerically, this is implemented by a displacement-controlled (rigid) or load-controlled (flexible) calculation, where the superimposed load is applied directly to the weightless soil. The settlement underneath the foundation as well as the lateral upward displacement of the soil (bulging) that occurs when the load is increased can be illustrated using Figure 2.
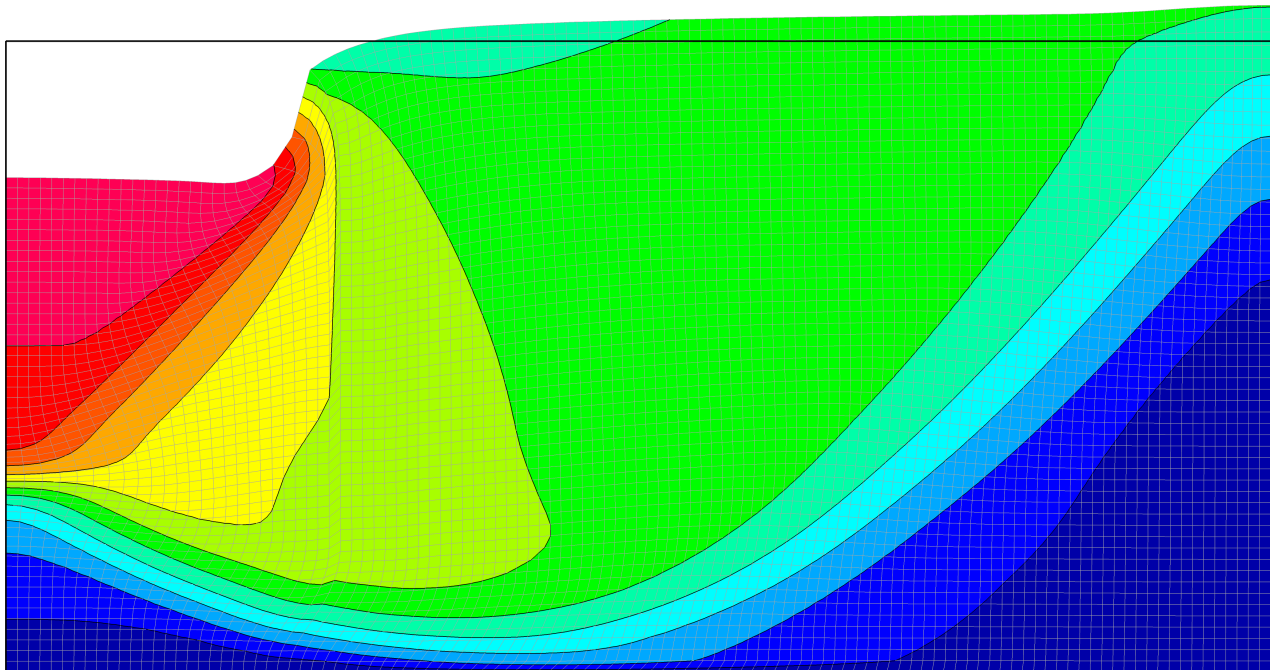
Figure 2: Deformation of the soil layer - flexible foundation

The mechanism of the bearing capacity failure of foundation (active wedge, radial shear zone, passive wedge) becomes even clearer using Figure 3 than when considering the deformations. When displaying the equivalent plastic strains, the shape of the slip surface becomes obvious. In addition to fracture figures, the *Mohr-Coulomb* plasticity model available in *InfoCAD* can also be used to numerically predict the ultimate load of the soil (maximum soil pressure).
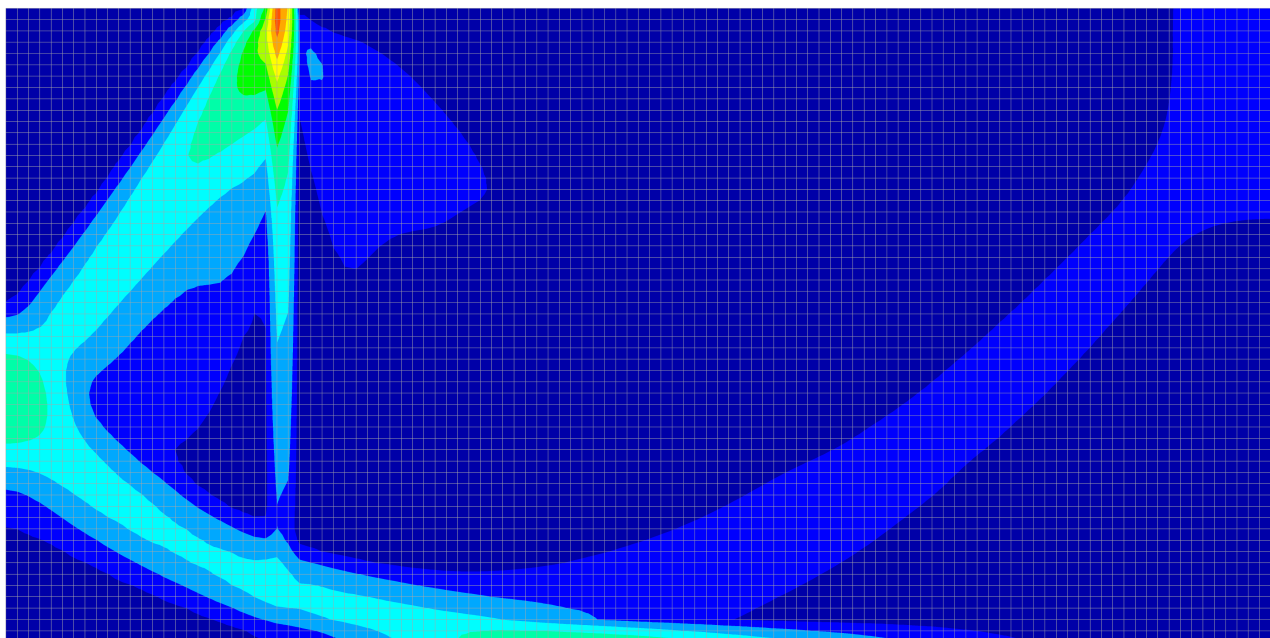
Figure 3: Equivalent plastic strains ε_v - flexible foundation (maximum values form sliding surface)

The analyses performed with the arc length method (number of iterations: 20, initial arc length: 1 (rigid) bzw. 0.1 (flexible), Up limited, error threshold: 0.01%, constant stiffness) are in very good agreement with the reference solutions from *Zienkiewicz et al. (1975)* and *Prandtl (1921)*, both for associative (Figure 4) and non-associative (Figure 5) plasticity.
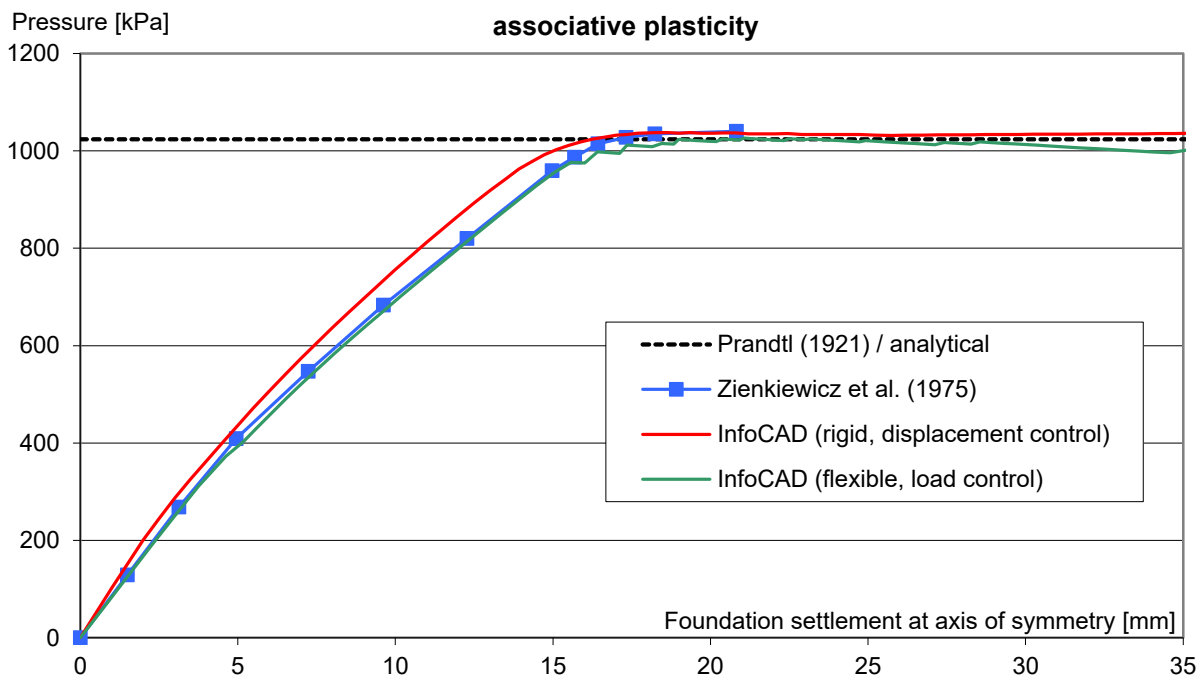
Figure 4:   Load-deformation curve (associative flow rule: φ = ψ = 20°)

The influence of the foundation stiffness is negligible here (deviation at the maximum bottom pressure is about 5%).
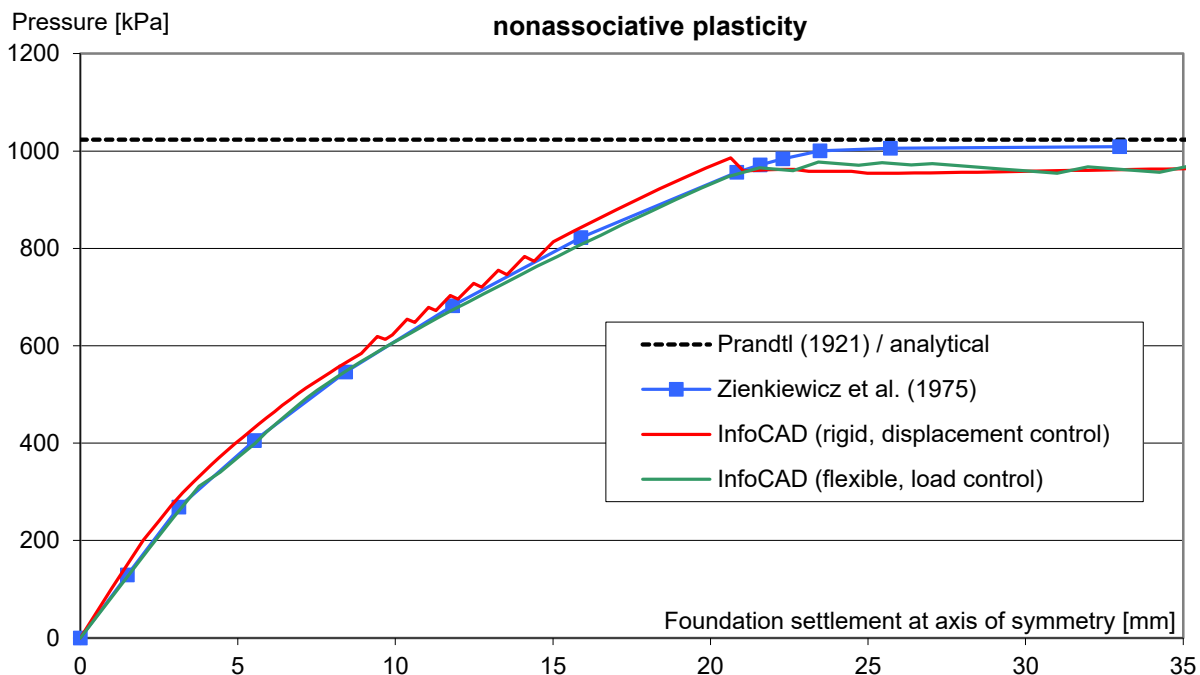
Figure 5:   Load-deformation curve (non-associative flow rule: φ = 20°, ψ = 0°)

Embankment Failure

To calculate the safety factor (FoS) or utilization factor (1 / FoS) of an embankment, the rule according to *Fellenius* (1927) [*Phi-c Reduction*] is used in *InfoCAD*. The soil parameters (friction angle φ and cohesion *c*) are successively reduced (see Eq. 1) until the failure of the soil occurs, characterized by the sliding of the sliding body on a sliding surface (slope failure).

$$\text{Cohesion}_{\text{Failure state}} = \text{Cohesion} / \text{FoS}$$

$$\text{Friction angle}_{\text{Failure state}} = \arctan(\ \tan(\text{Friction angle}) / \text{FoS}\ )$$

(Eq. 1)

On the basis of the problem described below and shown in Figure 6, taken from the publication by *Griffiths & Lane* (1999), the results calculated with *InfoCAD* are verified on the one hand and on the other hand possible analysis settings and internal program adjustments made when using the *Phi-c Reduction* are explained. The embankment failure simulation can be performed with any of the three implemented nonlinear analysis methods and is activated in the *Nonlinear System Analysis* settings (Serviceability).
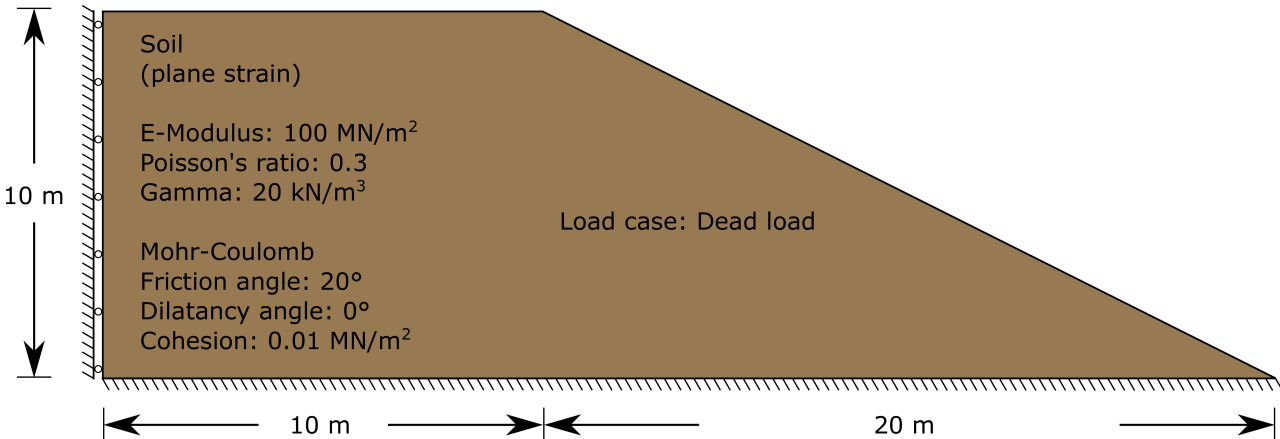
Figure 6:   Dimensions (thickness d=1m), boundary conditions and material parameters

The results obtained with both available analysis methods, the Newton and arc length methods, are compared here. Whereas with the arc length method (iterations per arc length 200; initial arc length 0.2; limited; tolerance 0.01%; constant stiffness) the dead weight is increased incrementally until the entire load is applied (load factor = 1), with the Newton method (max. iterations per load step 200; tolerance 0.01%; constant stiffness) the load is applied immediately. In addition, to show a possible influence of the discretization on the calculation of the factor of safety (FoS), the analysis was performed with three different FE meshes (tetrahedron elements). The numerically determined safety factors are included in Table 1.

Number of elements	Analysis method	
	Newton	Arc length method
1822	1.35	1.325
18922	1.35	1.325
55085	1.35	1.325

Table 1:   Influence of discretization and analysis method on the determination of the safety factor

Newton and the arc length method provide a factor of safety of 1.35 and 1.325, independent of the discretization. The values correspond very well both with the numerical reference solution of *Griffiths & Lane* (1999) [FoS = 1.35 (last convergent state)] and with the analytical solution of *Bishop & Morgenstern* (1960) [FoS = 1.38]. In *InfoCAD*, in addition to the factor, the reduced soil properties are also logged, see Figure 7. When using the arc length method or the Newton time-step method, the log also contains the entire history of the *Phi-c Reduction* (all increments of the interval nesting).

Phi-c Reduction: Load case 1 (Serviceability)

```
Factor of Safety (FoS) according to Fellenius  :   1.35

Reduced parameters (Failure)
Nr.     Friction angle [°]   Dilatancy angle [°]    Cohesion [MPa]
-------------------------------------------------------------
  1           15.1                 0.0                 0.0074
```
Figure 7: Log entry

In the same way as in the foundation failure analysis, the sliding surface occurring within the soil can also be clearly recognized here using the equivalent plastic strains (Figure 8). It should be noted that all *Phi-c Reduction* results (deformations, stresses, strains, etc.) presented in *InfoCAD* show the condition when the embankment is still stable and not the condition when the embankment has already failed.

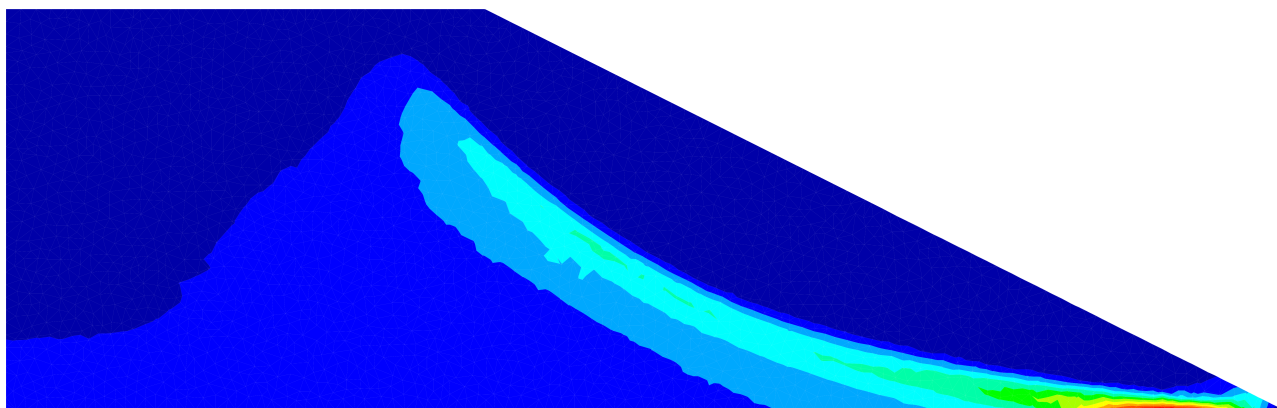*Figure 8:*   *Equivalent plastic strains* ε_v *(maximum values form sliding surface)*

It should also be noted that the load-time curve is adjusted internally in the program when the Newton time-step method is used for embankment failure calculation. The internal adjustment affects all loads with assigned *load-time curves*. Here, a load-time curve entered by the user as desired is converted into a linear load-time curve (Figure 9). The duration at which the maximum load factor (f(t)=1) is reached is to be defined by the user in the analysis settings.
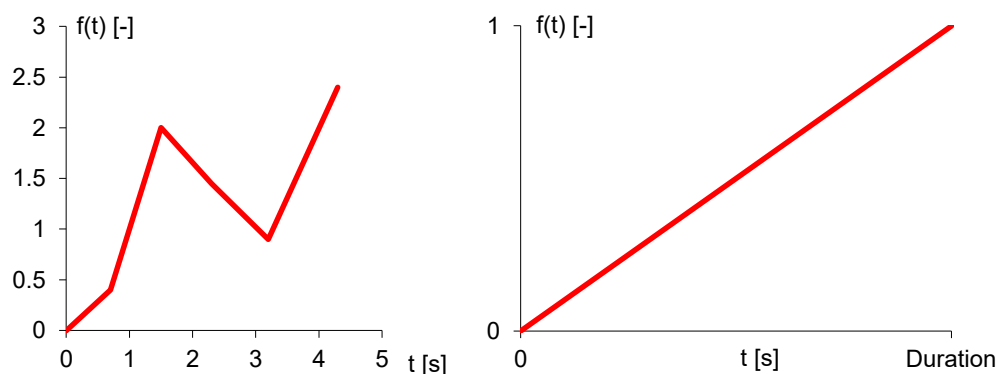
Figure 9: Load-time curve when using the nonlinear analysis method Newton time steps.
Left: Random load-time curve (entered in InfoCAD), right: load-time curve after automatic adjustment.

Snap Through Problem of a Cylindrical Shell

The cylindrical shell subjected to a central point load as shown below was first numerically investigated by *Sabir* and *Lock* in 1972. Their results are used to verify the arc length method implemented in InfoCAD. For the comparison calculation, the structure with jointed supports on two sides was discretized with 20x20 shell elements.

Discretization with supports, load and parameters
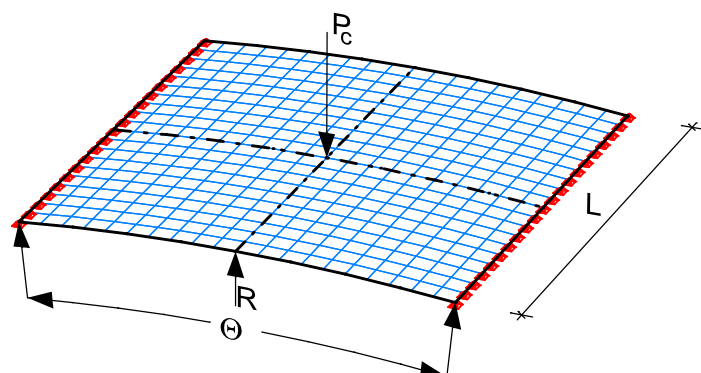
Parameters:

P_c = 1 kN
R = 2540 mm
Θ = 0,2 rad
L = 508 mm
t = 6.35 mm
E_s = 3102.64 MN/m²
v = 0.3

The calculation was based on the third order theory assuming linear-elastic material behavior (Error threshold 0.01 %). In order to illustrate the influence of the arc length on the numerical result as well as to show two possibilities to control the end of the calculation, three FE simulations with different specifications for the non-linear system analysis were performed.

Settings:	Case 1	Case 2	Case 3
Control:	Load factor = 1	Load factor = 1	1. Bifurcation point
Initial arc length:	0.1	auto	0.1
Up limited:	yes	no	yes
Iterations per arc length:	3	3	3

As illustrated in the figure below, all load-displacement curves calculated with the arc length method are in good agreement with the results of *Sabir* and *Lock*. (identical result curve for case 1 and 3 until first branch point is reached, load factor = 0.53) In addition, it becomes clear that a sufficiently small arc length is required for a detailed resolution of the complete equilibrium path.
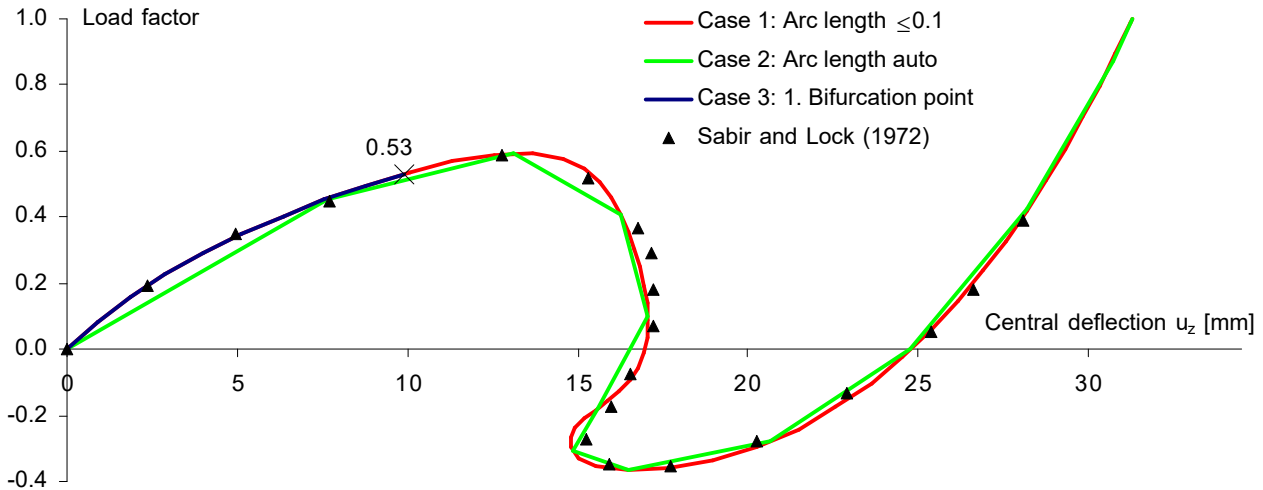
Load-displacement curves

References

Bažant, Z.P, Oh, B.H.
    Crack band theory for fracture of concrete, Materials and Structure, Volume 16, pp. 155-177,
    Publisher: Springer Verlag, 1983.

Beispiele zur Bemessung nach Eurocode 2 – Band 2: Ingenieurbau.
    Publisher: Deutscher Beton- und Bautechnik-Verein E.V., Ernst & Sohn Verlag, Berlin 2015.

Bishop, A. W., Morgenstern, N., Stability coefficients for earth slopes, Géotechnique, Volume 10, Edition 4, pp. 129-153,
    1960.

CEB-FIP Model Code 1990, Design Code
    Authors: Comite Euro-International Du Beton - 1993, Publisher: Thomas Telford Ltd, London 2007.

Chaboche, J.-L.
    Continuous damage mechanics — A tool to describe phenomena before crack initiation,
    Nuclear Engineering and Design, Volume 64, Issue 2, pp. 233-247, 1981.

Chen, W.F. & Han, D.J.
    Plasticity for Structural Engineers, Springer-Verlag, New York, 1988.

Cornelissen, H.A.W., Hordjik, D.A., Reinhardt,H.W.
    Experimental determination of crack softening characteristics of normalweight and lightweight concrete, Heron, Volume 31, Issues 2, Delft University of Technology, Delft, Netherlands 1986.

Crisfield, M.A.
    Non-linear Finite Element Analysis of Solids and Structures.
    John Wiley & Sons, Ltd. New York 1991.

Darwin, D.; Pecknold, D.A.W.
    Inelastic Model for Cyclic Biaxial Loading of Reinforced Concrete.
    A Report on a Research Project Sponsored by The National Science Foundation, Research Grant GI 29934
    University of Illinois at Urbana-Champaign Urbana, Illinois 1974.

De Borst, R.
    Non-linear analysis of frictional materials, Dissertation, Delft University of Technology, 1986.

De Vree, J.H.P., Brekelmans, W.A.M., van Gils, M.A.J., Comparison of nonlocal approaches in continuum damage
    mechanics, Computers & Structures, Volume 55, Issue 4, pp. 581-588, 1995.

© InfoGraph GmbH, February 2024

DIN EN 1992-1-1/NA:2013+A1:2015-12
>   National Annex – Nationally determined parameters –
>   Eurocode 2: Design of concrete structures – Part 1-1: General rules and rules for buildings.
>   Publisher: DIN Deutsches Institut für Normung e.V., Beuth Verlag GmbH, Berlin 2015.

DIN 1045-1:2008-08 (New Edition)
>   Concrete, reinforced and prestressed concrete structures – Part 1: Design and construction.
>   Publisher: DIN Deutsches Institut für Normung e.V., Beuth Verlag GmbH, Berlin 2008.

DIN 1045, Edition July 1988
>   Structural use of concrete – Design and construction.
>   Publisher: DIN Deutsches Institut für Normung e.V., Beuth Verlag GmbH, Berlin 1988.

DIN 18800:2008-11
>   Stahlbauten (Steel Structures) – Part 1 to Part 4.
>   Publisher: DIN Deutsches Institut für Normung e.V., Beuth Verlag GmbH, Berlin 2008.

Duddeck, H.; Ahrens, H.
>   Statik der Stabwerke (Statics of Frameworks), Betonkalender 1985. Ernst & Sohn Berlin 1985.

EN 1992-1-1:2004+A1:2014
>   Eurocode 2: Design of concrete structures – Part 1-1: General rules and rules for buildings.
>   Publisher: CEN European Committee for Standardization, Brussels. Beuth Verlag GmbH, Berlin 2014.

EN 1993-1-1:2005+A1:2014
>   Eurocode 3: Design of steel structures – Part 1-1: General rules and rules for buildings.
>   Publisher: CEN European Committee for Standardization, Brussels. Beuth Verlag GmbH, Berlin 2014.

EN 10025-2:2019-10
>   Hot rolled products of structural steels – Part 2: Technical delivery conditions for non-alloy structural steels.
>   Publisher: CEN European Committee for Standardization, Brussels. Beuth Verlag GmbH, Berlin 2019.

Ernst, G.C.; Smith, G.M.; Riveland, A.R.; Pierce, D.N.
>   Basic reinforced concrete frame performance under vertical and lateral loads.
>   ACI Material Journal 70(28), pp. 261-269. American Concrete Institute, Farmingten Hills 1973.

Fellenius, W., Erdstatische Berechnungen mit Reibung und Kohäsion (Adhäsion) und unter Annahme kreiszylindrischer
>   Gleitflächen, Verlag von W. Ernst u. Sohn, Berlin, 1927.

Gafoor, A.H., Dinkler, D.
>   A macroscopic gradient-enhanced damage model for deformation behavior of concrete under cyclic loadings.
>   Archive of Applied Mechanics Volume 90, pp. 1179–1199; Springer Verlag, Berlin Heidelberg 2020.

Griffiths, D. V., Lane, P. A., Slope stability analysis by finite elements, Géotechnique, Volume 49, Edition 3, pp. 387-403,
>   1999.

Hegger, J. et al.
>   Beurteilung der Querkraft- und Torsionstragfähigkeit von Brücken im Bestand – erweiterte Bemessungsansätze
>   (Assessment of the shear and torsion capacity of existing bridges - extended design approaches)
>   Berichte der Bundesanstalt für Straßenwesen, Brücken- und Ingenieurbau, Heft B 150.
>   (Reports of the Federal Highway Research Institute, Bridge and Engineering Construction, Book B 150)
>   Publisher: Federal Highway Research Institute (BASt), https://bast.opus.hbz-nrw.de/, 2020.

Hillerborg, A., Modéer, M., Petersson, P.-E.
>   Analysis of crack formation and crack growth in concrete by means of fracture mechanics and finite elements, Cement
>   and Concrete Research, Volume 6, Issue 6, pp. 773-781, Publisher: Pergamon Press. USA 1976.

Hirschfeld, K.
>   Baustatik Theorie und Beispiele (Structural Analysis Theory and Examples).
>   Springer Verlag, Berlin 1969.

Hordjik, D.A.
>   Tensile and tensile fatigue behaviour of concrete; experiments, modelling and analyses,
>   Heron, Volume 37, Issue 1, pp. 3-79.
>   Publisher: Delft University of Technology, Delft, Netherlands 1982.

Hofstetter, G., Mang, H.A., Computational Mechanics of Reinforced Concrete Structures, Vieweg Verlag, Wiesbaden, 1995.

Irwin, G.R.
>   Fracture, Elasticity and Plasticity, pp. 551-590, Publisher: Springer Verlag, Berlin 1958.

Jofriet, J.C.; McNeice, M.
>   Finite element analysis of reinforced concrete slabs.
>   Journal of the Structural Division (ASCE) 97(ST3), pp. 785-806. American Society of Civil Engineers, New York 1971.

Kachanov, L.M.
>   On time to rupture in creep conditions (in russian)
>   Izviestia Akademii Nauk SSSR, Otdelenie Tekhnicheskikh Nauk, 8, pp. 26-31, 1958.

Kachanov, L.M.
>   Introduction to continuum damage mechanics, Volume 10. Springer Science & Business Media 1986.

Kindmann, R.
    Traglastermittlung ebener Stabwerke mit räumlicher Beanspruchung
    (Limit Load Determination of 2D Frameworks with 3D Loads).
    Institut für Konstruktiven Ingenieurbau, Ruhr-Universität Bochum, Notice no. 813, Bochum 1981.

Knott, J.F.
    Fundamentals of fracture mechanics, Publisher: Butterworth & Co Ltd, London 1973.

König, G.; Weigler, H.
    Schub und Torsion bei elastischen prismatischen Balken (Shear and Torsion for Elastic Prismatic Beams).
    Ernst & Sohn Verlag, Berlin 1980.

Krätzig, W.B.; Meschke, G.
    Modelle zur Berechnung des Stahlbetonverhaltens und von Verbundphänomenen unter Schädigungsaspekten
    (Models for Calculating the Reinforced Concrete Behavior and Bonding Phenomena under Damage Aspects).
    Ruhr-Universität Bochum, SFB 398, Bochum 2001.

Krätzig, W.B., Pölling,R.
    An elasto-plastic damage model for reinforced concrete with minimum number of material parameters, Computers & Structures, Volume 82, Issues 15–16, pp. 1201-1215, 2004.

Krejci, H., Mang, H.A., Zur Traglastberechnung von Stahlbetonkonsolen mittels der Methode der Finiten Elemente (For the ultimate load calculation of reinforced concrete corbels with the finite element method), Beton- und Stahlbetonbau, 81 (1986), pp. 15 - 21.

Kupfer, H. B.; Hilsdorf, H. D.; Rüsch, H.
    Behavior of Concrete under Biaxial Stresses.
    ACI Structural Journal 1969, pp. 656-666. American Concrete Institute, Farmington Hills 1969.

Lee, J., Fenves, G. L., Plastic-damage model for cyclic loading of concrete structures. Journal of engineering mechanics, Volume 124(8), pp. 892 - 900, 1998.

Lemaitre, J., & Chaboche, J.-L.
    Mechanics of solid materials, Cambridge university press 1990.

Link, M.
    Finite Elemente in der Statik und Dynamik (Finite Elements in Statics and Dynamics).
    Teubner Verlag, Stuttgart 1984.

Litzner, H.-U.
    Grundlagen der Bemessung nach DIN 1045-1 in Beispielen.
    Beton-Kalender 2002, Volume 1, pp. 435-480.
    Ernst & Sohn Verlag, Berlin 2002.

Lubliner, J., Oliver, J., Oller, S., Oñate, E.
    A plastic-damage model for concrete,
    International Journal of Solids and Structures, Volume 25, Issue 3, pp. 299-326, Publisher: Elsevier Ltd. 1989.

Maurer, R.; Gleich, P.; Heeke, G.; Zilch, K.; Dunkelberg, D.
    Untersuchungen zur Querkrafttragfähigkeit an einem vorgespannten Zweifeldträger
    (Investigations into the shear capacity of a prestressed double-span beam).
    Reports of the Federal Highway Research Institute (BASt) Book B 120, Bergisch Gladbach, 2015.

Maurer, R.; Kattenstedt, S.; Gleich, P.; Stuppak, E.; Kolodziejczyk, A.; Zilch, K.; Dunkelberg, D.; Tecusan; R.
    Nachrechnung von Brücken - Verfahren für die Stufe 4 der Nachrechnungsrichtlinie
    Tragsicherheitsbeurteilung von Bestandsbauwerken
    (Structural assessment of concrete bridges - Procedures in level 4 of the structural assessment provisions
    Structural safety assessment of existing buildings).
    Forschung Straßenbau und Straßenverkehrstechnik Heft 1120
    (Research road construction and road traffic engineering Book 1120)
    Federal Ministry of Transport and digital Infrastructure, Bonn, 2016.

Mazars, J., Hamon, F. & Grange, S.
    A new 3D damage model for concrete under monotonic, cyclic and dynamic loadings. Materials and Structures, Volume 48, pp. 3779–3793, Publisher: RILEM 2014.

Mazars, J., Grange, S., Simplified strategies based on damage mechanics for concrete under dynamic loading, Philosophical Transactions of the Royal Society A, Volume 375, Issue 2085, Publisher: The Royal Society 2017.

Mehmel, A.; Freitag, W.: Tragfähigkeitsversuche an Stahlbetonkonsolen (Load capacity tests on reinforced concrete corbels).
    Der Bauingenieur 42 ,pp. 362–369, 1967.

Meschke, G., Synthese aus konstitutivem Modellieren von Beton mittels dreiaxialer, elasto-plastischer Werkstoffmodelle und Finite-Elemente-Analysen dickwandiger Stahlbetonkonstruktionen (Synthesis of constitutive modeling of concrete using three-axial elasto-plastic material models and finite element analyses of thick-walled reinforced concrete structures), Dissertation, Technische Universität Wien, 1989.

Oliver, J.
    A consistent characteristic length for smeard cracking models,
    Int. Journal for Numerical Methods in Engineering, Volume 28, pp. 461-474, 1989.

OENORM B 4700:2001-06
Reinforced concrete structures – EUROCODE-orientated analysis, design and detailing.
Publisher: Österreichisches Normungsinstitut. ON Österreichisches Normungsinstitut, Vienna 2001.

Pande, G.N., Beer, G., Williams, J.R.
Numerical Methods in Rock Mechanics, John Wiley & Sons, New York, 1990.

Peerlings, R. H. J.
Enhanced damage modelling for fracture and fatigue.
Ph.D. Thesis, Technische Universiteit Eindhoven, Eindhoven 1999.

Petersen, Ch.
Statik und Stabilität der Baukonstruktionen (Statics and Stability of Constuctions).
Vieweg Verlag, Braunschweig 1980.

Petersson, P. E.
Crack growth and development of fracture zones in plain concrete and similar materials, Dissertation, Division of Building Materials, LTH, Lund University, 1981.

Poliotti M., Bairan, JM.
A new concrete plastic-damage model with an evolutive dilatancy parameter, Engineering Structures 2019.

Prandtl, L.
Über die Eindringungsfestigkeit (Härte) plastischer Baustoffe und die Festigkeit von Schneiden,
Zeitschrift für Angewandte Mathematik und Mechanik, Volume 1, Issue 1, pp. 15-20, 1921.

Quast, U.
Nichtlineare Stabwerksstatik mit dem Weggrößenverfahren (Non-linear Frame Analysis with the Displacement-Method).
Beton- und Stahlbetonbau 100. Ernst & Sohn Verlag, Berlin 2005.

Raghava, R.S., Caddell, R.M. & Yeh, G.S.Y.
The macroscopic yield behaviour of polymers.
Journal of Materials Science 8, pp. 225–232, Michigan USA 1973.

Rankine W.J.M.
A Manual of Applied Mechanics. London and Glasgow 1858.

Reinhardt H.W., Cornelissen H.A.W.
Post-Peak Cyclic Behaviour of Concrcete in Uniaxial Tensile and Alternating Tensile and Compressive Loading,
Stevin Laboratory of Delft University of Technology, CEMENT and CONCRETE RESEARCH. Volume 14, pp. 263-270,
Publisher: Pergamon Press, Delft, Netherlands 1984.

Richart, F. E., Brandtzæg, A., Brown, R. L.
A study of the failure of concrete under combined compressive stresses,
University of Illinois at Urbana Champaign, Volume 26, Issue 12, Champaign, 1928.

Rots, J. G., Nauta, P., Kusters, G. M. A.
Blaauwendraad, J., Smeared crack approach and fracture localization in concrete, Heron, Volume 30(1), Delft University of Technology, 1985.

Sabir, A.B.; Lock A.C.
The applications of finite elements to large deflection geometrically nonlinear behaviour of cylindrical shells.
In Variational methods in engineering: proceedings on an international conference held at the University of Southampton, 25th September, 1972.
Brebbia, C.A.; Tottenham, H. (eds.) Southampton University Press 1972.

Schleicher, F.
Der Spannungszustand an der Fließgrenze (Plastizitätsbedingung).
Zeitschrift für Angewandte Mathematik und Mechanik, Volume 6, Book 3, pp. 199-216,
WILEY-VCH Verlag GmbH & Co. KGaA, Weinheim, 1926.

Schwarz, H. R.
Methode der finiten Elemente (Method of Finite Elements).
Teubner Studienbücher. Teubner Verlag, Stuttgart 1984.

SIA 262:2013 Bauwesen
Concrete Structures, Swiss Standard SN 505 262,
Registered standard of the Swiss Association for Standardization SNV,
Publisher: Schweizerischer Ingenieur- und Architektenverein, Zürich 2013.

Simo, J. C., Hughes, T. J. R.
Computational Inelasticity, Springer Verlag, New York, 1998

Sinha B.P., Gerstle K.H. und Tulin L.G.
Stress-Strain Relations for Concrete Under Cyclic Loading
Journal of the American Concrete Institute ACI, February issue 1964.

Stempniewski, L.; Eibl, J.
Finite Elemente im Stahlbetonbau (Finite Elements in Reinforced Concrete Construction).
Betonkalender 1993. Ernst & Sohn Verlag, Berlin 1993.

Suanno, R.L.M., Ein dreidimensionales Simulationsmodell für Stahlbeton mit Plastizität und Schädigung (A three-dimensional simulation model for reinforced concrete with plasticity and damage), Dissertation, Universität Stuttgart, 1995.

Tikhomirov, D., Stein, E., Anisotrope Schädigungskonzepte für nichtlineare
Berechnungen von Stahlbetonkonstruktionen (Anisotropic damage concepts for nonlinear

calculations of reinforced concrete structures), Bauingenieur, 74 (1), pp. 36-44, 1999.

Vonk, R. A.
Softening of concrete loaded in compression, Dissertation, Technische Universität Eindhoven 1992.

Winkler, B. J.
Traglastuntersuchungen von unbewehrten und bewehrten Betonstrukturen auf der Grundlage eines objektiven Werkstoffgesetzes für Beton, Dissertation, Innsbruck University Press, 2001.

Zedler, T.
Zum Tragverhalten von Stahlbeton- und Spannbetonbalken unter Torsion,
Dissertation, Fakultät für Bau- und Umweltingenieurwissenschaften der Ruhr-Universität Bochum,
Bochum Januar 2011.

Zienkiewicz, O.C., Humpheson, C., Lewis, R.W.
Associated and non-associated visco-plasticity and plasticity in soil mechanics. Geotechnique, Volume 25, Issue 4, pp. 671-689, 1975.

InfoGraph GmbH

Kackertstrasse 10

52072 Aachen, Germany

Phone: +49 241 889980

Fax: +49 241 8899888

info@infograph.eu

www.infograph.eu

InfoGraph

Software für die Tragwerksplanung